Récupération d'énergie efficace à Métasurface pour applications IoT

Raziyeh Sharifi

INSTITUT POLYTECHNIQUE DE PARIS

TELECOM Paris

IP PARIS

NNT : 2025IPPAT019

Thèse de doctorat

Efficient Metasurface Energy Harvesters for IoT Applications

Thèse de doctorat de l'Institut Polytechnique de Paris
préparée à Télécom Paris

École doctorale n°626 École doctorale de l'Institut Polytechnique de Paris (ED IP Paris)

Spécialité de doctorat: Électronique et optoélectronique

Thèse présentée et soutenue à Palaiseau, le 11 Juin 2025, par

Raziyeh SHARIFI

Composition du Jury:

Nel SAMAMA Professeur, Télécom SudParis	Président/Examinateur
Ala SHARAIHA Professeur des Universités, Université de Rennes	Rapporteur
Eric LHEURETTE Professeur des Universités, Université de Lille	Rapporteur
Ludivine FADEL Maître de Conférences, Université de Bordeaux	Examinatrice
Xavier BEGAUD Professeur, Télécom Paris	Directeur de thèse
Anne Claire LEPAGE Maître de conférences, Télécom Paris	Co-directrice de thèse
Kyriaki NIOTAKI Maître de conférences, Télécom Paris	Invitée/Co-encadrante de thèse

To my family,

your love and support have been the foundation of all my achievements.

Acknowledgments

I would like to sincerely thank my thesis director, Prof. Xavier Begaud, and my supervisors, Dr. Anne Claire Lepage and Dr. Kyriaki Niotaki, for their guidance throughout this journey to help me grow and explore new possibilities.

A sincere thank you to the jury members — Prof. Ala Sharaiha, Prof. Eric Lheurette, Prof. Nel Samama, and Dr. Ludivine Fadel — for their valuable feedback and for taking the time to evaluate my work.

To my parents, whose unconditional love and encouragement have been my foundation and greatest source of strength—I am forever grateful for your belief in me.

To my soulmate, whose angelic presence turns every ordinary day into a glimpse of heaven, I am grateful to have you in my life.

My heartfelt thanks go to my friends, especially my best friend Parni, whose vibrant energy and constant moral support transformed this challenging path into an unforgettable experience.

My gratitude also goes to Prof. Lirida Naviner, who always supports PhD candidates and helps make their journey smoother. I would also like to thank Prof. Bruno Thedrez for his valuable guidance and many engaging discussions.

Finally, I am grateful to my colleagues, whose thoughtful scientific discussions and camaraderie made the daily work of my PhD both engaging and inspiring.

“You were born with potential.

You were born with goodness and trust.

You were born with ideals and dreams.

You were born with greatness.

You were born with wings.

You are not meant for crawling, so don’t.

You have wings.

Learn to use them and fly.”

Rumi

Abstract

Wireless communications and the Internet of Things are becoming integral parts of modern life. By avoiding the need for batteries—thereby reducing the cost as well as the size and weight of appliances—energy harvesting by collecting ambient energy represents a promising alternative power supply. Ambient energy in the environment can be captured from various sources like solar, wind, or radio frequency signals, etc. While solar and wind energy are characterized by a high power density, these sources are not always available. Radio frequency signals, on the other hand, have the advantage of being ubiquitously present but have a comparatively low power density.

There are several solutions for collecting electromagnetic energy; two common solutions are rectenna and metasurface for energy harvesting. To use absorbers in energy harvesting devices, the challenge is to maximize the collected energy and thus to minimize losses which occur in dielectrics. To do so, metasurfaces, with their low profile and absorption characteristics can be good candidates using a low-loss substrate.

In general, in energy harvesting devices based on metasurface, either multi-layer or planar structures can be used. The main drawback of multi-layer structures is the complexity of fabrication. Planar designs help to overcome this problem. Moreover, as the ambient radio frequency energy is usually low, it is necessary to collect most of it by improving the performance of the metasurface. To do so, in this thesis, compact efficient metasurface harvesters are proposed: a single-band design operating at 2.45 GHz and a dual-band design operating at 2.45 GHz, and 5.2 GHz.

Firstly, the metasurface structures have been designed. Given the low levels of ambient radio frequency energy, it is crucial to maximize the collected power. To address this challenge, an intermediate step in the design process is introduced to enhance the capturing efficiency of metasurface. This additional step is applied for both proposed single and dual-band designs. A finite array of 5×4 cells is presented for both designs. The simulated capturing efficiency of the central rows of the finite array for the single-band design is 90% at 2.54 GHz. The simulated capturing efficiency of the central rows of the finite array for the dual-band design is 74% at 2.5 GHz, and 30% at 5.09 GHz.

Secondly, a single-band rectifier circuit based on Schottky diodes is proposed to be integrated with the single-band metasurface structure, in order to convert the collected radio

frequency energy to DC. The rectification efficiency at 2.49 GHz at the differential input of the rectifier at -2.7 dBm, is 58%.

Each proposed design of the metasurfaces and the rectifier has been analyzed independently. Then all have been fabricated and measured to verify their performance.

Résumé

Les communications sans fil et l'Internet des objets (IoT) deviennent des éléments incontournables de la vie moderne. En évitant l'utilisation de batteries et en réduisant ainsi les coûts, la taille et le poids des appareils, la récupération d'énergie ambiante représente une alternative prometteuse pour l'alimentation électrique.

L'énergie ambiante peut être captée à partir de diverses sources telles que l'énergie solaire, éolienne ou les signaux radiofréquences (RF). Alors que les énergies solaire et éolienne offrent une densité de puissance élevée, elles ne sont pas toujours disponibles. À l'inverse, les signaux RF sont omniprésents, mais leur densité de puissance est relativement faible.

Plusieurs solutions permettent de collecter l'énergie électromagnétique, notamment les rectennas et les métasurfaces pour la récupération d'énergie. Pour utiliser des absorbants dans les dispositifs de récupération d'énergie, le défi principal est de maximiser l'énergie collectée et ainsi de minimiser les pertes dans les diélectriques. À cet égard, les absorbants à base de métasurface, grâce à leur faible épaisseur et leurs caractéristiques d'absorption constituent des solutions prometteuses si on utilise un substrat à faibles pertes.

En général, les dispositifs de récupération d'énergie basés sur des métasurfaces se présentent sous forme de structures multicouches ou planaires. L'inconvénient majeur des structures multicouches réside dans leur complexité de fabrication. Les conceptions planaires permettent de surmonter ce problème. De plus, étant donné que l'énergie RF ambiante est généralement faible, il est essentiel d'en capter un maximum en optimisant les performances du dispositif récupérateur d'énergie.

Dans cette thèse, des récupérateurs d'énergie à base de métasurface compacts et efficaces sont proposés : une structure monobande fonctionnant à 2,45 GHz et une bi-bande fonctionnant à 2,45 GHz et 5,2 GHz.

Dans un premier temps, les métasurfaces ont été conçues. Étant donné les faibles niveaux d'énergie RF ambiante, maximiser la puissance collectée est une priorité. Pour relever ce défi, une étape intermédiaire dans le processus de conception a été introduite afin d'améliorer l'efficacité de capture. Cette étape supplémentaire a été appliquée aux deux structures, monobande et bi-bande. Un réseau fini de 5×4 cellules est développé pour chaque

structure. L’efficacité de capture des rangées centrales du réseau fini simulé atteint 90 % à 2,54 GHz pour la version monobande. Pour la conception bi-bande, l’efficacité de capture des rangées centrales est de 74 % à 2,5 GHz et de 30 % à 5,09 GHz en simulation.

Dans un second temps, un circuit redresseur mono-bande à base de diodes Schottky est proposé pour être intégré à la métasurface mono-bande, afin de convertir l’énergie RF captée en courant continu. L’efficacité de redressement à 2,49 GHz pour une puissance d’entrée de -2,7 dBm atteint 58 %.

Les métasurfaces mono-bande et bi-bande ainsi que le redresseur ont été analysés indépendamment. Ensuite, tous les dispositifs ont été fabriqués et mesurés afin de vérifier leurs performances.

Contents

List of Figures

List of Tables

List of Acronyms

IoT Internet of Things

RFID Radio Frequency Identification

DC Direct Current

2-D Two-Dimensional

SRR Split Ring Resonator

TE Transverse Electric

TM Transverse Magnetic

ADS Advanced Design System

RMS Root Mean Square

FWHM Full Width at Half Maximum

Q-factor Quality-factor

SMD Surface Mount Device

AC Alternating Current

HB Harmonic Balance

EM Electromagnetic

General Introduction

General Introduction

Energy harvesting refers to the process of collecting energy from ambient sources and transforming it for storage or to power a wide variety of applications. Rather than focusing on commonly known forms of ambient energy such as wind and solar, the purpose of this thesis is to propose an efficient device to collect ambient RF energy, such as that found in the signals emitted by wireless routers. Although the ambient RF power level is comparatively low, it is widely available and can be sufficient to support modest power requirements such as those of internet of things (IoT) devices; it may also supplement primary power supplies such as batteries.

Wi-Fi signals at 2.45 GHz and 5.2 GHz (IEEE 802.11ax/be), represent one of the most accessible and widely available sources for RF energy harvesting in modern life. The channel bandwidth of the networks 802.11ax/be is 20/40/80/160 MHz [1-5]. These frequencies are commonly found in environments such as homes, offices, and public spaces such as train stations, as well as outdoor areas where Wi-Fi networks are freely accessible, such as cities like Luxembourg. Potential applications include powering Internet of Things (IoT) devices, such as sensors in smart homes and offices, as well as health monitoring systems [6]. Harvesters operating at these frequencies can also be used to collect ambient RF energy, to supply the power of passive Radio Frequency Identification (RFID) tags, which do not have an internal battery to power their data storage chips [7, 8].

An RF energy harvester typically comprises two essential components, a receiver and a rectifier circuit. The receiver is responsible for capturing RF energy from the surrounding environment, ensuring efficient energy collection. To facilitate the collection of ambient RF energy, so-called metasurfaces can be employed. These are purpose-engineered materials (metamaterials) with favorable properties that allow for near-complete absorption of the incident RF power. In addition to their high absorption potential, another key feature of metasurface absorbers is their low thickness. Note that, as stated in the paragraph above, merely absorbing the ambient energy is not enough - it must either be stored or direct consumed for an application. As captured power takes the form of AC current, it must be therefore first be rectified to, say, charge a battery or supply power to a sensor.

This thesis proposes efficient metasurface RF energy harvesters designed to operate at Wi-Fi bands (2.45 GHz, 5.2 GHz) for IoT applications. In addition to the devices' designs,

we aim to introduce a methodology to enhance the collected RF power by the proposed metasurface harvesters. A further objective is to ensure that the designed harvesters are simple to realize and incorporate as few components as possible, thereby minimizing potential component-related losses. To this end, this manuscript focuses on the design, simulation, fabrication, and measurement of compact single-layer efficient metasurface RF harvesters that incorporate only a few components to collect the RF power and later convert it to DC. The manuscript is structured into four chapters.

In Chapter I, we give a brief background on different ambient sources for energy harvestings, later a detailed overview of RF energy harvesters operating on the basis of a metasurface harvester and a rectifier is provided.

A detailed discussion of our proposed single-band metasurface harvester follows in Chapter II. Concretely, we propose a single-band harvester operating at 2.45 GHz. A design approach is presented and applied to our proposed metasurface harvester. The discussion begins with the design of the unit cell, where the operating frequency is determined by factors such as the harvester's geometric dimensions and shapes. Having chosen the dimensions and thereby fixed the operating frequency, the next design step is followed by connecting multiple cells to each another in order to increase the collected RF power. The design methodology is proposed in order to maximize the collected power. As the final design step, a finite array is designed, and a detailed analysis of it, along with an explanation of the necessity for this in-depth analysis, is provided. The simulated performance of the proposed single-band metasurface harvester is evaluated by the measurement.

In Chapter III, the RF power collected by the single-band metasurface harvester is converted into DC using a rectifier. First, a brief background on rectifiers is provided, followed by a discussion on the key components of a typical rectifier circuit. The design of the rectifier is then presented, with a justification for selecting a single-diode configuration based on the various topologies explored in this chapter. The rectifier geometry is designed to be compatible with the metasurface harvester. The input power of the rectifier is chosen to be relatively low, in order to be closer to real life conditions. The simulated results are provided and discussed, and these results are then examined through measurements of the fabricated rectifier. The fabricated rectifier is connected with the fabricated single-band metasurface harvester to conduct further measurements and evaluate the overall device performance.

Chapter IV presents the final contribution of this thesis with the extension of the structure to a multiband design. Concretely, we adapt the design of the metasurface harvester of Chapter II so as to not only target the Wi-Fi band at 2.45 GHz, but also that at 5.2 GHz. The design steps are followed and the proposed methodology is applied to the dual-band RF metasurface harvester to maximize the collected RF power. The finite array of the dual-band harvester is designed, and its simulated performance is evaluated through the measurement.

Finally, general conclusions are drawn, and future research works are suggested

1 State of the Art

1.1 Introduction

Energy harvesting is an effective, sustainable approach to power devices by capturing energy from the surrounding environment [1-11]. Unlike conventional power sources such as batteries that have a finite lifespan and that may be too bulky to integrate in a target application, energy harvesters gather ambient energy whenever available, making them a promising alternative for self-sustaining system [12, 13]. This is particularly relevant in applications where continuous power supply and minimal maintenance are essential, such as in remote sensing networks and IoT [14-19].

IoT devices, which include smart sensors, wireless networks, and autonomous systems, have seen widespread adoption in healthcare, agriculture, smart cities, and industry. Traditional battery-powered IoT systems often require periodic maintenance, which can be costly and impractical, especially for large-scale setups in remote or otherwise difficult-to-reach locations. Hence, energy harvesting serves as a crucial enabler of sustainable and low-maintenance IoT systems by reducing reliance on conventional power sources [14-17].

An energy harvester is a system that captures energy from an external source—such as light, heat, motion, or electromagnetic waves—and converts it into usable electrical power. Energy harvesters may tap into a variety of different sources which are introduced in the following section [1]. For now, we merely wish to mention that the ambient energy source targeted in this thesis – Radio Frequency (RF) energy [20-26] – provides substantial advantages due to its widespread availability. This compensates for its rather low power density, and makes it highly relevant for applications such as low-power sensors and IoT devices [14, 19, 27-31].

While different designs have been proposed for RF energy harvesters, we shall focus on those based on metasurfaces, that is, engineered materials whose properties can be tuned so as to achieve a high absorption efficiency, as it will be later discussed in this chapter [32, 33]. When discussing metasurface-based RF energy harvesters, we will distinguish between multilayer and planar structures [34-45] and carefully describe the advantages and disadvantages of both; this will be done as part of a broader discussion on designing RF energy harvesters that are both simple and yet highly efficient.

1.2 Energy Harvesting

Broadly speaking, energy harvesting systems operate by collecting energy from ambient sources and converting it to electrical energy. Their operating principles, along with their advantages and disadvantages, depend on the underlying source of energy. Below, we describe the most common ambient energy sources.

Solar energy is converted to electrical energy using, for instance, solar panels [40-47]. For heat, so-called thermoelectric converters are employed [48-50]. Mechanical energy (such as vibrations, material stress, etc.) is converted to electrical energy using a transducer operating based on various physical mechanisms, for example, piezoelectricity [51-53]. Wind is converted to electrical energy by means of turbines [54, 55]. Another common ambient source, RF energy is collected by an antenna or a metasurface harvester [20-45]. RF energy harvesting offers a unique advantage in that it captures energy from electromagnetic waves that are already present in the environment. These waves, emitted by devices like Wi-Fi routers, cellular networks, and radio towers, offer a consistent and readily accessible energy source [56-58].

In Table 1.1 the above-mentioned common ambient energy sources are summarized along with their key properties.

Table 1.1 Common ambient energy harvesting sources [53, 56-58].

Ambient Energy	Sources (examples)	Power Density	Advantages	Disadvantages
Solar	Sun	100 $\mu W/cm^2$ [53]	+ High power + Advanced technology	- Dependency on weather and time - Expensive (solar panels) - Not compact (required large panel)
Thermal	Sun Body heat System losses	60 $\mu W/cm^2$ [53]	+ Losses can be reused	- Low available power - Not compact (required large area [31])
Mechanical	Vibrations Material stress	250 $\mu W/cm^2$ [53]	+ High power + Advanced technology	- Dependency on activity or motion - Expensive
Wind	Wind	177 $\mu W/cm^2$ [57]	+ Possibility to harvest low winds	- Dependency on weather - Can be bulky harvester
RF	Cellular networks Wi-Fi bands Radio and TV broadcast signals	40 $\mu W/cm^2$ [53]	+ Indoor and outdoor availability + Low profile	-Low efficiency

As can be seen in Table 1.1 certain energy sources such as solar and wind are characterized by a high power density. However, these sources are not always available and are weather-dependent. Thermal energy, another widely available source often requiring larger harvesters [31]. Mechanical energy harvesters operate based on vibrations or movement, which may introduce variability in power generation depending on the environmental variations [53, 56-58].) Each energy harvesting method has its own characteristics, making them suitable for different applications. RF signals, have the advantage of being ubiquitously present but have a comparatively low power density which can be nonetheless enough to turn on some sensors or support low-power devices [53]. Additionally, RF energy harvesters benefit from a constant and predictable energy source, as RF signals are continuously emitted by communication networks in the modern life.

In conclusion, RF energy is a source that is widely present and comparatively easy to harvest for a wide range of relevant applications such as IoT and sensors. The following section provides an introduction to metasurface RF energy harvesters.

1.3 Introduction of Metasurface RF Energy Harvesters

RF energy harvesters comprise two parts: a receiver and a rectifier circuit. The discussion of the latter is deferred to Chapter III, where we present the associated theory in detail and propose a rectifier to be employed in our RF energy harvester. The former (the receiver) may be implemented using different structures such as antennas [59-61], and metamaterials/metasurfaces [34-45]. A schematic of a simplified metasurface harvester as a receiver and a connected rectifier is shown in Figure 1.1. In several studies to design a metasurface harvester, first a rectifier circuit is replaced by a resistive load. The objective is to design the metasurface such as the maximum ambient RF energy is collected in this resistive load. Second, in the final device this resistive load can be replaced by a suitable rectifier to convert collected RF power to DC.

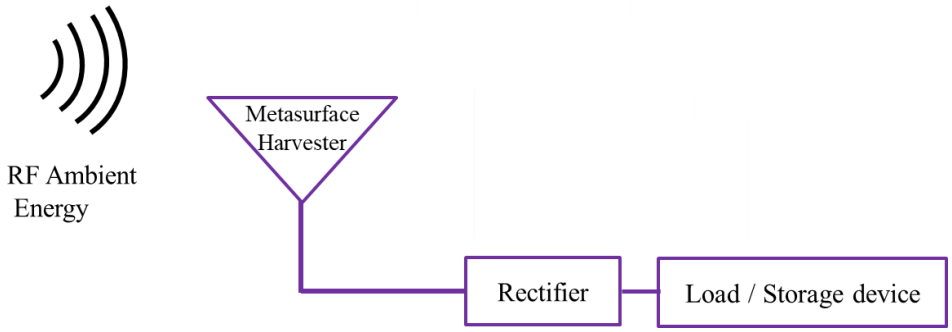

Figure 1.1 A schematic of a simplified metasurface with a connected rectifier.

Metasurface RF energy harvesters can therefore be seen as an instance of RF energy harvesters where the receiver is implemented by means of a metasurface. This choice is motivated by the fact that the ambient RF energy is usually low, and it is hence of great importance to collect it as efficiently as possible. Metamaterials/metasurfaces, with their high absorption efficiency, are an excellent candidate for this task. Additionally, metasurfaces offer advantages such as compactness and tunability making them well suited for applications where space constraints are critical, such as IoT and wireless sensor networks.

Metamaterials can be defined as artificial materials, which have unique properties like negative refraction (negative permeability ($\mu_r < 0$) and permittivity ($\varepsilon_r < 0$)), features that cannot be found in natural materials [62-65]. The name metamaterial comes from the word "meta" in Greek, which means "beyond". The two-dimensional (2-D) arrangement of a metamaterial structure is called metasurface; conceptually speaking, it is a structure comprising periodically arranged unit cells that serve as resonators [65-67].

In 2002 [68], Engheta came up with the idea that metamaterials/metasurfaces can, due to their unique characteristics, be purpose-engineered as absorbers which are much thinner than their classical counterparts in the microwave range [69-71].

As Engheta envisaged, metasurface absorbers with their high absorption are a viable choice to absorb electromagnetic energy efficiently. The absorption characteristics of a metasurface are defined by the geometric properties of the underlying unit cells (such as the metallic shape and size) and by its periodicity, as well as by the substrate properties [72, 73].

A distinction should be made between metasurface absorbers and metasurface harvesters: The former is employed in the context of the latter to collect RF energy [74]. A low-loss substrate is employed to avoid the dissipation of the collected energy in the dielectric and instead transfer it to a resistive load. In the following section a brief summary on wave reflection, transmission and absorption background is provided.

1.4 Key Definitions

In this section, we briefly review some definitions useful to describe performances of absorbers and energy harvesters. These are the metrics used in the following chapters.

An incident electromagnetic wave arriving onto a material interacts with the latter in three different ways: parts of it are reflected, transmitted, and absorbed. Denoting the power in these three parts by $P_{reflected}$, $P_{transmitted}$, and $P_{absorbed}$, respectively, and the power of the incident wave by P_{in}, conservation of energy states that

$$P_{in} = P_{reflected} + P_{transmitted} + P_{absorbed} . \quad (1.1)$$

The reflection of the wave occurs due to an impedance mismatch between the surrounding medium (in this thesis, free space) and the material that the wave is incident

on. The fraction of the reflected power is quantified by the frequency-dependent power reflection coefficient $R(\omega)$ which is defined as:

$$R(\omega) = P_{reflected} / P_{in} \tag{1.2}$$

Analogously to the definition of the power reflection coefficient, the power transmission coefficient quantifies the fraction of the transmitted power that continues to propagate in the material:

$$T(\omega) = P_{transmitted} / P_{in} \tag{1.3}$$

Finally, the power absorption coefficient quantifies the fraction of the incident power that is neither reflected nor transmitted but rather dissipated by interaction with the material. This dissipation may be due to losses in the dielectric, metallic parts, or conversion to other forms of energy depending on the material's properties and design. The power absorption coefficient is expressed as:

$$A(\omega) = P_{absorbed} / P_{in} \tag{1.4}$$

Dividing both the left- and right-hand side of Equation (1.1) by P_{in}, and using Equations (1.2), (1.3), (1.4), conservation of energy may be expressed succinctly in terms of the coefficients as

$$1 = R(\omega) + T(\omega) + A(\omega). \tag{1.5}$$

If the metasurface absorber includes a metallic backing plate that prevent any transmission ($T(\omega) = 0$), the above equation can be simplified and rewritten as:

$$A(\omega) = 1 - R(\omega). \tag{1.6}$$

Since the objective in designing the metasurface RF harvester is – naturally – to maximize the absorbed RF ambient power and to deliver most of it to a resistive load, the parameters of a design should be chosen so as to maximize $A(\omega)$ and minimize $R(\omega)$.

Finally, we shall touch on the different notions of efficiency involved in the design of a metasurface RF energy harvester. The absorption efficiency is defined as the (percentage) ratio of the time-average power absorbed by the metasurface design over the time-average incident power over the metasurface area:

$$\text{Absorption efficiency} = (P_{absorbed} / P_{in}) \times 100 = A(\omega) \times 100. \quad (1.7)$$

Note that maximizing A(ω) (as suggested as above) is tantamount to maximizing the absorption efficiency. While necessary, this goal is not sufficient: we do not only seek to maximize the absorbed power, but rather the power delivered to the load (P_{dl}). Since the power can be partially dissipated in the dielectric substrate ($P_{loss\text{-}dielectric}$) and metallic components ($P_{loss\text{-}metals}$), the absorption efficiency counts for those losses as well:

$$P_{absorbed} = P_{loss\text{-}dielectric} + P_{loss\text{-}metals} + P_{dl} \quad (1.8)$$

For an energy harvester, the objective is to maximize the capturing efficiency of the metasurface defined as:

$$\eta_{MS} = P_{dl}/P_{in} \quad (1.9)$$

Thus, only when also minimizing losses in the dielectric and metallic components can the concentration of the absorber power into the resistive load – and therefore the capturing efficiency – be truly maximized. In the following section, some existing works on metasurface RF energy harvesters and their key features are presented, along with a comparison of their performance.

1.5 Metasurface RF Energy Harvesters

In 2012 an electromagnetic energy harvester using metamaterials was proposed for the first time by Ramahi et al. [33]. The goal was to demonstrate that it is possible to use a split ring resonator (SRR) and place a resistor within its gap to gather the captured electromagnetic energy irrespective of the incident field's polarization. To that end, an SSR, as shown in Figure 1.2 (a) was designed to operate at 5.8 GHz with Rogers Duroid RT5880 used as the substrate at a thickness of 0.79 mm. The magnetic incident field is normal to the plane of the SRR. A finite array of 9×9 SRRs was simulated, with a resistive load of 2.3 kΩ located in the gap of each SRR, as shown in Figure 1.2 (b). The capturing efficiency of the metasurface array of 9×9 cells at three different incident angles ($\varphi=30^0,45^0, 60^0$) is shown in Figure 1.2 (c); it is more than 40% at 5.8 GHz at all three simulated angles. Together, these findings support the initial goal of demonstrating that the SRR array can be used to collect electromagnetic energy by the resistors positioned within its gap.

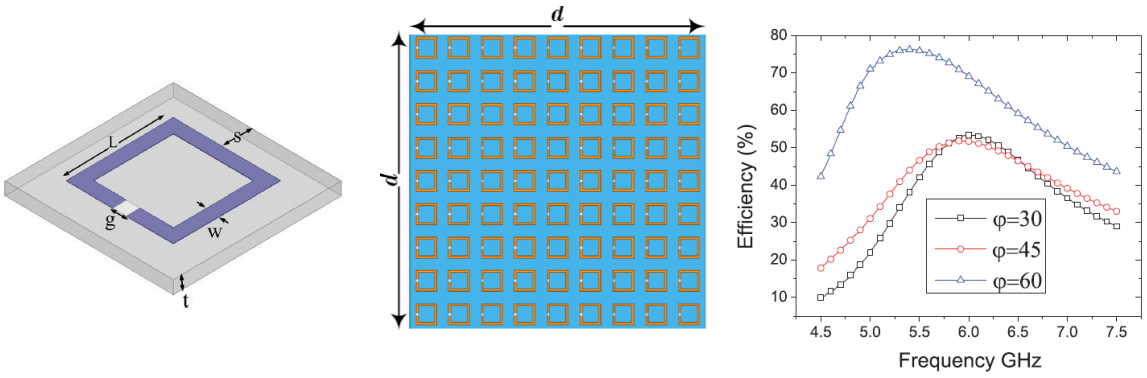

(a) (b) (c)

Figure 1.2 (a) A split ring resonator element, (b) an SRR array of 81 unit cells, and (c) simulated capturing efficiency of the finite array at different incident angles [33].

It is worth recalling that to design a metasurface harvester for RF energy harvesting applications, the first step may be collecting the RF energy in a resistive load, which is later replaced by a rectifier. However, the focus of work [33] was mostly on capturing the electromagnetic energy.

Metasurface RF energy harvesters can be classified into two categories: multi-layer and planar structures. Each of these categories can whether include a rectifier to convert RF energy into DC power or use only lumped elements to mimic the rectifier's impedance. Works highlighting the properties of these respective designs are discussed below.

1.5.1 Multi-layer Structures

Following the work of [33], several studies have focused on enhancing the performance of RF metasurface harvesters, for example, by improving efficiency or achieving polarization insensitivity [35-44, 74-78]. The following paragraphs will discuss studies with several layers, which can generally be categorized into two groups: designs that collect RF power in a resistive load and those that collect RF power and convert it to DC using a rectifier.

1.5.1.1 EH without Inclusion of a Rectifier

To harvest ambient electromagnetic energy across multiple frequencies (8.4 GHz, 16 GHz, and 20.7 GHz), a wideband polarization-independent metamaterial was designed in [35]. Note that in its illustration in Figure 1.3 (a), four vias are employed to provide a conductive path that directs the current induced on the unit cell's surface toward four 50 Ω

resistive loads. These loads are positioned between the vias and the metallic ground. The dielectric layer used in the structure is F4B-2 with a loss tangent of 0.001 and a permittivity of 2.65. The substrate with a thickness of 3 mm is placed between the top and ground layers. In metasurface energy harvesters containing vias, the positioning of vias plays a critical role in optimizing current flow toward the loads. Consequently, careful design is required to achieve maximum capturing efficiency.

Simulated results of the periodic unit cell under different incident angles, for both transverse electric (TE) and transverse magnetic (TM) polarizations, are shown in Figure 1.3 (b). It is observed that the maximum capturing efficiency was above 88% for incidence angles up to 45^0 with a minimum half-power bandwidth of 83% irrespective of the polarization. After the study of the unit cell, a 5×5 array of the design was fabricated, and the middle cell of it was chosen for the measurement. The measured capturing efficiencies of the middle unit cell of the fabricated array were 82% at 7 GHz, 91% at 15 GHz, and 89% at 19.5 GHz under normal incidence, as shown in Figure 1.3 (c).

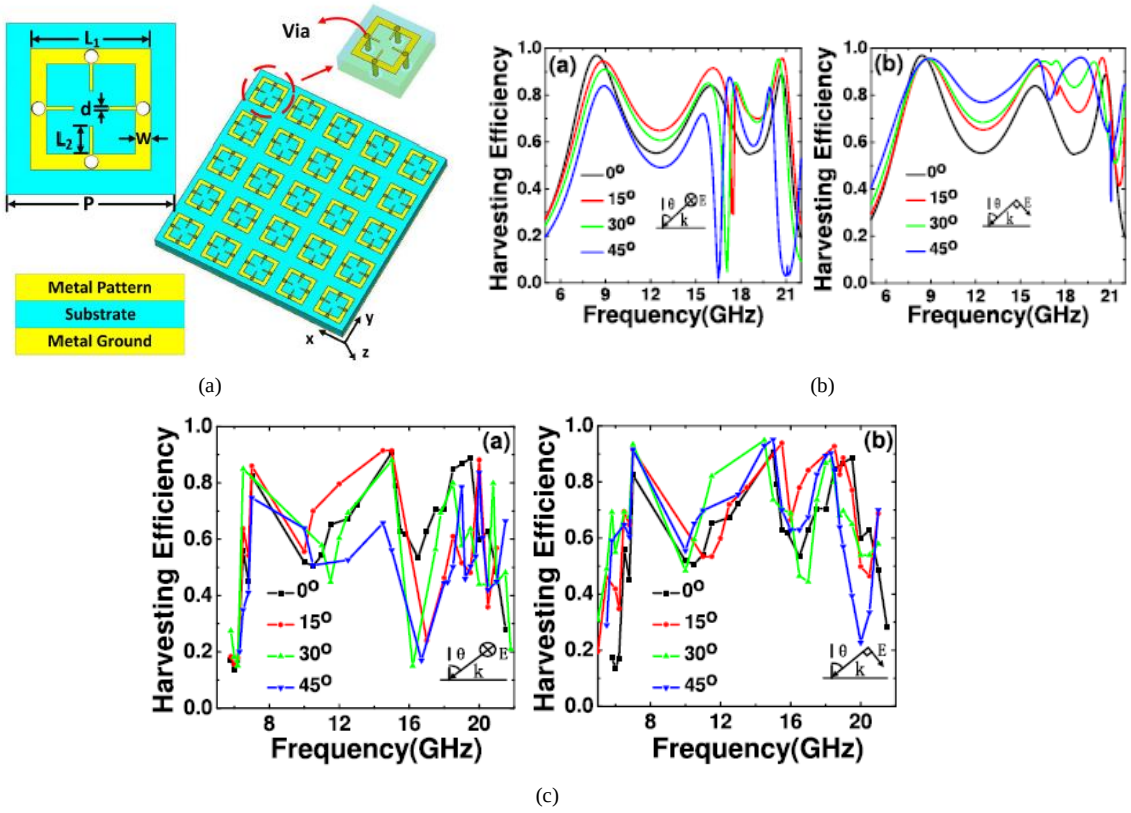

Figure 1.3 (a) Geometry of the unit cell incorporating 4 vias, (b) simulated and (c) measured capturing efficiencies of the middle cell of the finite array at different incident angles under different polarizations [35]

A noticeable difference is observed between the results of the simulated periodic unit cell and the measured middle cell in a finite array. The proposed design in this work, despite its good performance, presents challenges related to the use of multiple vias, which can increase fabrication complexity.

As discussed in [35], several works have been presented with the feature of polarization-insensitivity; however, multiple vias were employed in their proposed designs [36, 37, 44, 75]. To primary address this challenge, single-via designs were proposed [41, 42, 78].

In [41], a polarization-insensitive metasurface harvester designed for electromagnetic energy collection at 5.8 GHz is proposed. The unit cell geometry of this design is shown in Figure 1.4 (a), where a 50 Ω load is positioned on the bottom layer, connected between a single via and the ground plane. The defining feature of the proposed structure is the use of a single via to guide the current from the metasurface unit cell through a 0.787mm substrate, which has a dielectric constant of 2.2 and a loss tangent of 0.001, to a resistive load. Due to the symmetric geometry of the structure, the design is inherently insensitive to the polarization of the incident wave. Moreover, the proposed design exhibits acceptable performance across a wide range of incident angles for both TE and TM polarization, as evident in the plot presented in Figure 1.4 (b). At normal incidence, the simulated peak capturing efficiency of the unit cell reaches 88% at 5.8 GHz. In this work, after simulating the unit cell, a 5×5 metasurface array was fabricated, with the middle cell selected for measurement. The measured capturing efficiency of this middle cell for various incidence angles is presented in Figure 1.4 (c). At normal incidence, the measured peak capturing efficiency of the middle cell of the array is 80% at 5.91 GHz.

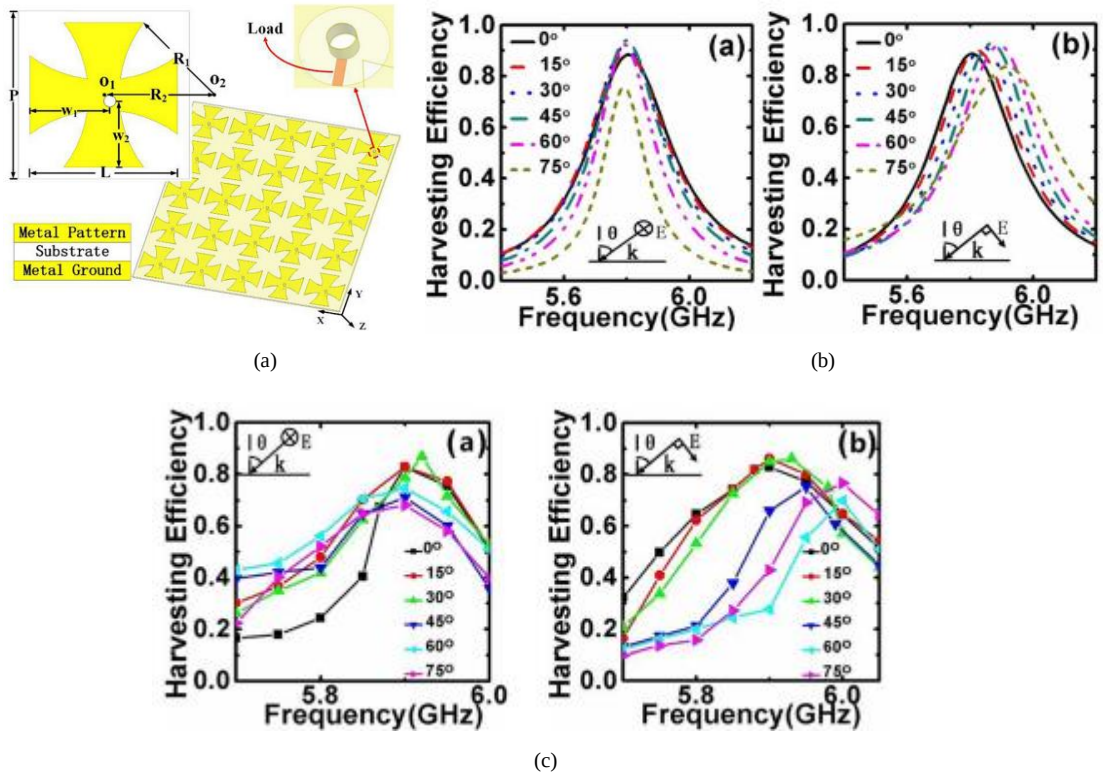

Figure 1.4 (a) Geometry of the unit cell incorporating a single via, (b) simulated and (c) measured capturing efficiencies of the unit cell under oblique incident angles up to 75° under different polarizations [41].

The differences between the simulated and measured results arise primarily from the simulation setup; the unit cell was simulated in periodic boundary conditions, whereas the measurement is conducted on a finite 5×5 array, with the middle cell used as a representative sample. Additionally, the authors mentioned fabrication errors as another source of this disagreement [41].

The works discussed so far have primarily focused on capturing RF power without addressing its conversion to usable DC power. However, some research efforts have advanced beyond RF energy collection to convert it into DC for practical applications.

1.5.1.2 EH with Inclusion of a Rectifier

The rectifier's role is to convert RF or AC power into DC power. A diode serves as its primary component for rectification, which will be discussed in detail in Chapter III. In metasurface RF harvester designs, either a single rectifier or multiple rectifiers can be incorporated. When a rectifier circuit is placed on a separate layer for integration with a

metasurface RF energy harvester, two common methods can be employed: DC-combining [79-82] or RF-combining [83-87].

DC-combining method

In the DC-combining method, each unit cell is connected to its own rectification circuit, with a matching network placed between them, as depicted in Figure 1.5. The rectified power from each unit cell is then aggregated using a DC power-combining network. Finally, the DC power is delivered to energy storage devices or a load. This approach offers a simple design for the DC combiner network, which is its primary advantage. However, a notable disadvantage is that the received power per unit cell might not be sufficient to activate the rectifier diode, particularly in environments where ambient energy is low. Furthermore, because of the additional DC combiner network, this method can result in a multi-layer structure, which makes the design complex and its fabrication difficult.

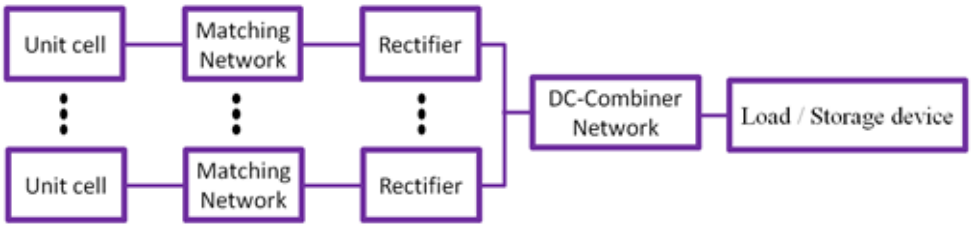

Figure 1.5 Configuration of a metasurface energy harvester with DC-combining network.

An example of a metasurface energy harvester employing a DC power combiner network can be found in the work of Xin Duan et al. [79]. A three-layer unit cell, as shown in Figure 1.6 (a), is optimized for a frequency of 2.45 GHz and integrates a rectifier positioned on the bottom layer. This rectifier is connected to the unit cell surface at the top layer via a via-hole. The top substrate layer is 3 mm thick polytetrafluoroethylene with permittivity of 2.65 and a low loss tangent of 0.0007. The intermediate layers are made of 0.1 mm thick Rogers RO4450F bondplys, while the bottom substrate layer is a 1 mm thick polytetrafluoroethylene dielectric.

A fabricated array of 6×6 cells is depicted in Figure 1.6 (b) with the comparison of simulation and measured efficiency for various incident power densities shown in Figure 1.6 (c). This configuration achieved a simulation efficiency of 73% and a measured efficiency of 67% under a power density of 5 mW/cm² at 2.45 GHz. Both simulation and measured results indicate an increase in efficiency with higher input power levels. The

authors suggested that discrepancies between the measured and simulated efficiencies might be attributed to fabrication imperfections, among other factors (not accurate model of the diode of Schottky diode HSMS-282B in Advanced Design System (ADS)) [79].

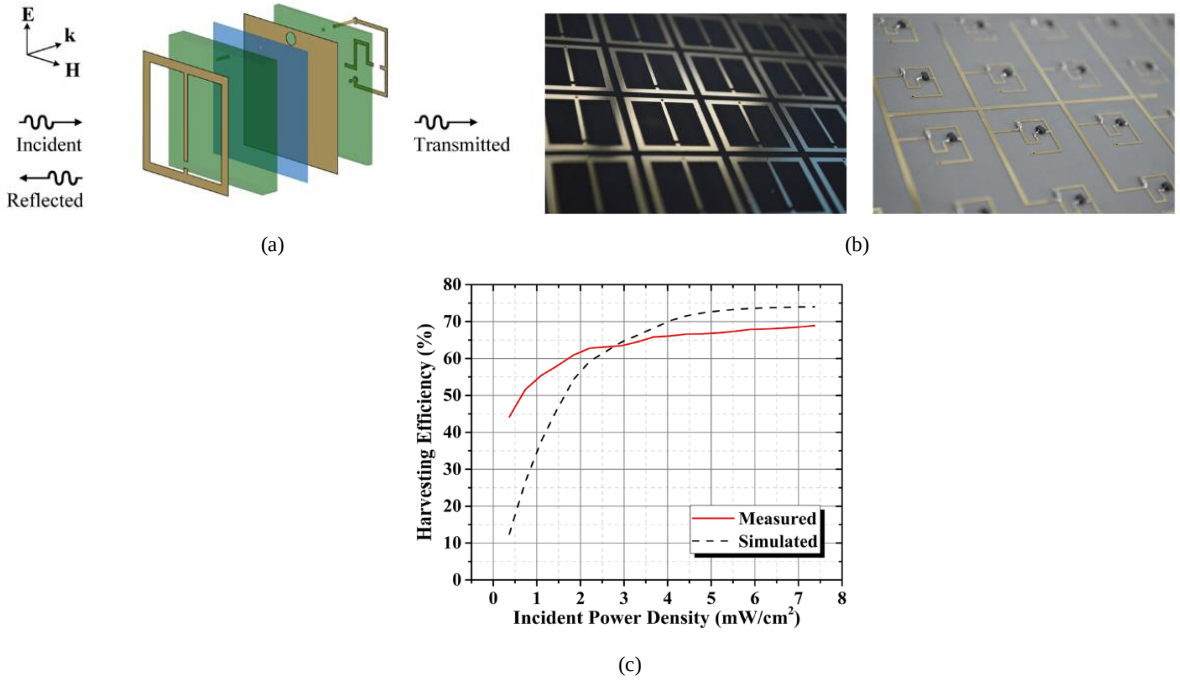

Figure 1.6 (a) Geometry of the proposed unit cell (b) fabricated array of a DC-combining design (c) comparison between the simulated and measured efficiencies [79].

The main advantage of this design is the simplicity of the DC-combining network. However, the need to connect each unit cell to a rectifier circuit may lead to additional losses due to the large number of diodes involved. Furthermore, the collected power may not always be sufficient to turn on the rectifier diode especially under low ambient energy conditions.

RF-combining

To address these challenges, an alternative technique known as RF-combining has been proposed, as illustrated in Figure 1.7. In the RF-combining method, the RF output power from multiple unit cells is aggregated to feed a single rectifier, whereas in the DC-combining method, the outputs of multiple rectifiers are combined.

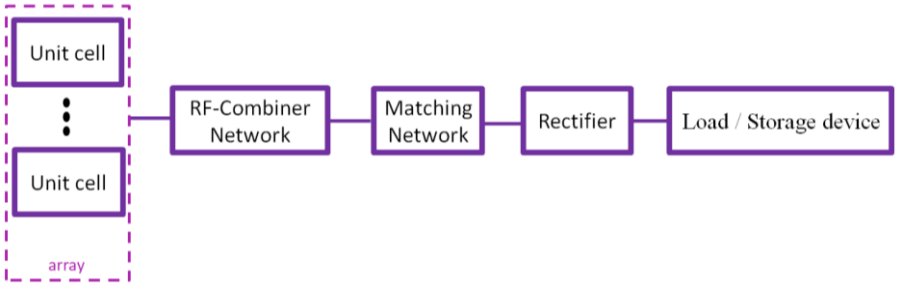

Figure 1.7 Configuration of a metasurface energy harvester with RF-combining network.

An example of a metasurface design incorporating an RF-combining network placed in a separate layer is presented in [83]. A schematic of a single cell is shown in Figure 1.8 (a), designed to resonate at 3 GHz. A resistive load of 200 Ω is placed in the bottom layer and connected to the top layer via a via-hole. The array consists of 8×8 unit cells designed on a Rogers TMM10i substrate with a thickness of 1.542 mm, permittivity of 9.9, and a loss tangent of 0.002. The RF-combining network is positioned beneath the array on a Rogers RT5880LZ substrate with a permittivity of 1.96 and a loss tangent of 0.0019, as shown in Figure 1.8 (b). Initially, each metasurface cell is designed with an impedance of 200 Ω. When the power from multiple resonators is combined through a corporate feed network, this impedance must be transformed to 50 Ω to match standard measurement equipment, such as a power meter. The simulation results for three different configurations are presented in the Figure 1.8 (c). The DC simulation illustrates the performance of the metasurface array, including a rectifier positioned at the output of the feeding network. A HSMS 2860 Schottky diode is used in the rectifier circuit design. The measured capturing efficiency of the proposed design is 78% at 2.9 GHz, while the total efficiency is 40% at 2.82 GHz under an input power of 12 dBm at the input of the rectifier.

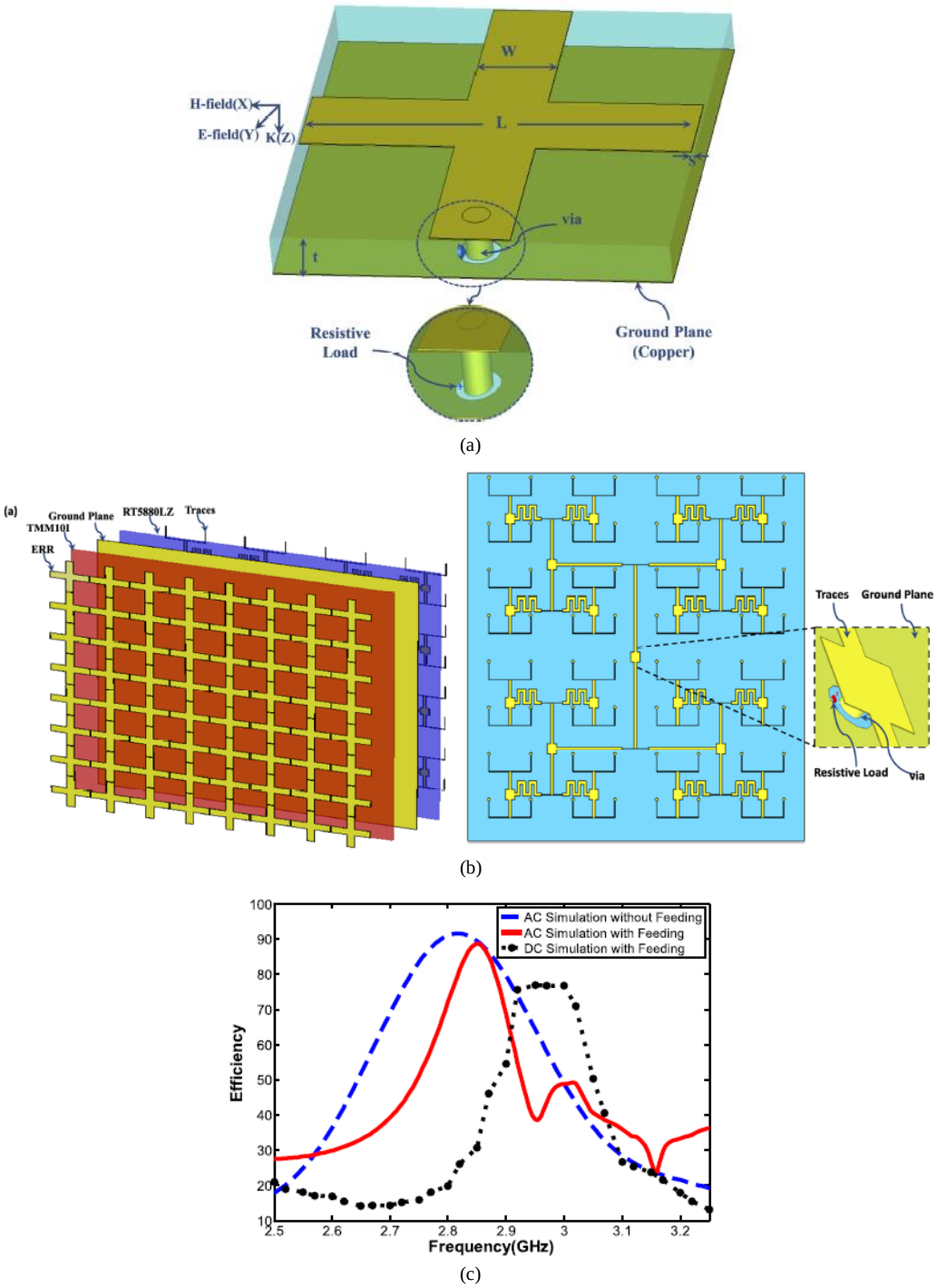

Figure 1.8 (a) Geometry of the proposed unit cell, (b) finite array consists of 64 unit cell with a feeding network, and (c) simulated efficiencies [83].

While the efficiency of the rectifier is not provided in this work, it may be among the reasons for the reduced total efficiency. The potential causes of the latter were not discussed by the authors.

Subsequent research has further explored this approach, introducing improvements in the metasurface harvesters by proposing a wideband design [84], polarization insensitivity design [85], and other enhancements [40, 78, 86, 87].

As previously mentioned, a key advantage of this method is that the RF output power from multiple cells is combined to feed a single rectifier. This means that even if the power received by each individual cell can be insufficient to activate a diode on its own—as is the case in DC-combining technique—it becomes effective when aggregated with the power from other cells, providing enough power at the input of the rectifier to turn the diode on. However, a notable drawback is the need to combine the outputs of individual cells using an RF-combining network that is placed in an additional layer and connected to a single rectifier. This multi-layer configuration increases design complexity and introduces fabrication challenges. Additionally, the feeding combining network design is intricate and can contribute to further losses. Moreover, incorporating vias in the design can contribute to higher losses.

1.5.2 Planar Structures

Planar designs offer an effective solution to overcome the challenges associated with multi-layer configurations. One approach to achieve this is by integrating the diode within the metasurface design, allowing the harvester to remain single-layered and compact [88-90]. In this technique, direct impedance matching between the metasurface design and the rectifier can be achieved, eliminating the need for additional DC or RF-combining networks. This method enhances the overall efficiency of the metasurface RF energy harvester. However, it must be implemented within the particular metasurface design. Alternatively, another strategy to increase the collected power at the output of the metasurface is the interconnected cells method, which is based on the RF-combining technique but without having a feeding network arranged in an extra layer [91-95, 97].

As mentioned before, due to the low ambient input power levels, a single rectifier connected to each individual cell may not receive sufficient power to turn on the diode. The interconnected cells method has the key advantage of collecting RF power from multiple cells instead of a single one, as shown in Figure 1.9. Multiple unit cells connected to one another in a row, with the last cell connected to a resistive load, are characterized as a

supercell. Due to its larger area, a supercell naturally collects more power than a single cell. The power collected by the supercell is directed to a single resistive load, whose value is the same as obtained for the unit cell [91, 92]. Similar to many previously discussed methodologies, initially the resistive load is present to simulate the rectifier input impedance. However, later this resistive load will be replaced with a suitable rectifier circuit to ensure DC output power for practical applications.

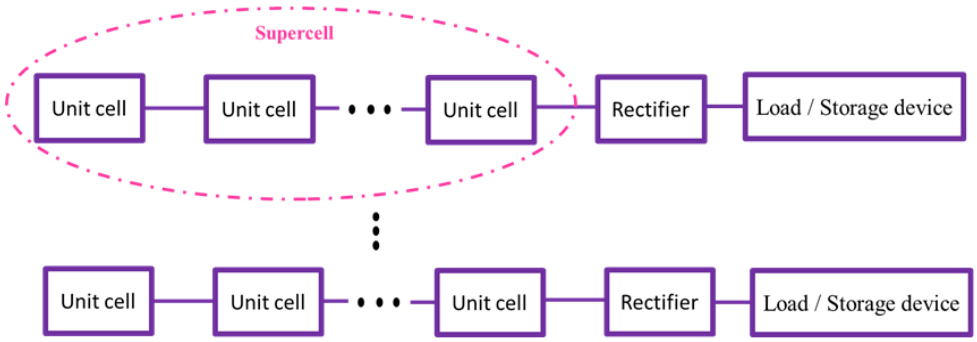

Figure 1.9 Configuration of a planar interconnected cells energy harvester.

In [91], the novel approach of interconnected cells is discussed. The optimized unit cell is shown in Figure 1.10 (a), where the polarization of the incident electric field is aligned along the y-axis. The structure consists of two substrate layers: Rogers RO4003C with a thickness of 1.524 mm and a 5 mm air spacer, both serving as dielectric materials. A lumped resistor of 370 Ω is placed at the end of the metallic strips. Simulations conducted in CST Microwave Studio indicate that the unit cell achieves an absorption of 98.5% and a capturing efficiency of 97% at 2.45 GHz [91]. An array of 5×6 cells was fabricated, as shown in Figure 1.10 (b) with indicating the measured area by the black dashed line. In this array, the resistor in the middle row was replaced with a rectifier circuit (diode HSMS-286P), while for the remaining rows, a 370 Ω resistor was placed at the end of the last cell in each row. The comparison between simulated and measured results is presented in Figure 1.10 (c). The simulated efficiency is obtained by multiplying the unit cell capturing efficiency, the matching efficiency, and the rectification efficiency

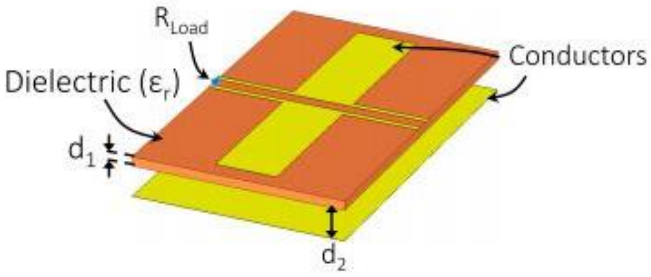

(a)

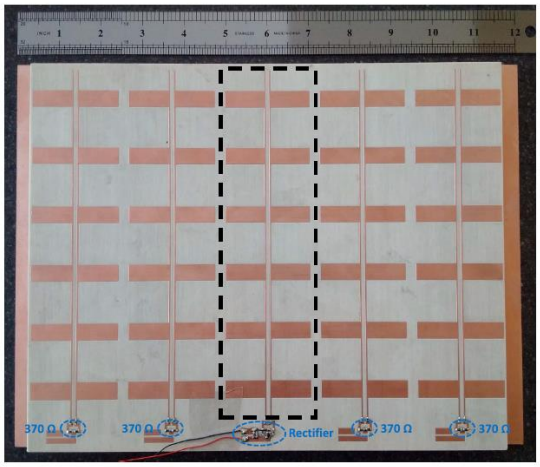

(b)

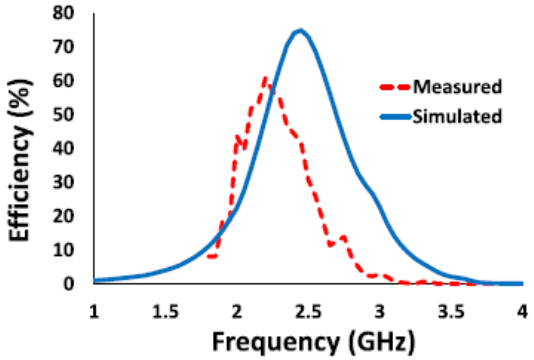

(c)

Figure 1.10 (a) Geometry of an interconnected unit cell, (b) a fabricated array of 5×6 unit cells, and (c) comparison of the simulated and measured efficiencies [91].

As observed in Figure 1.10 (c), there is a noticeable discrepancy between simulation and measurement results. The measured total efficiency reaches a peak of 61% at 2.2 GHz, whereas the simulated total efficiency is 75% at 2.45 GHz, when the power at the rectifier's input is 15 dBm. The study suggests that one possible explanation for the 200 MHz frequency shift between simulation and measurement is the finite size of the array [91]. However, one major contributing factor to this discrepancy could be the use of the unit cell capturing efficiency to calculate the total efficiency of the middle row or finite array. This is because, in a supercell, the interaction between the unit cell and its neighbors must be taken into account. In Chapter II, we suggest a solution to more accurately evaluate the efficiency in this configuration.

This work offers the advantages of a planar design and the ability to collect high RF power from multiple cells rather than a single cell. However, the total measured efficiency is based on an input power of 15 dBm at the rectifier, which is considered significantly high

compared to real-life scenarios. Additionally, the proposed design is sensitive to the polarization of the incident wave.

One recent work from 2024 [93] presents a wide-angle metasurface design operating at 5.8 GHz. In the proposed unit cell, shown in Figure 1.11 (a), a 1000 Ω load resistance positioned in the gap between the two triangles shapes, while the incident wave's polarization aligned along the y-axis. The F4B dielectric with a thickness of 3 mm, permittivity of 2.2, and loss tangent of 0.0009 has been employed as the substrate of this structure. The simulated efficiencies of the unit cell, indicate that the majority of the absorbed power is effectively collected by the resistive load.

The fabricated array of 5×7 cells is depicted in Figure 1.11 (b). Each row consists of 7 cells that are connected to each other via the two microstrip lines. These microstrip lines were not included in the initial unit cell design (see Figure 1.11 (a)). The middle row is terminated with a rectifier circuit and was selected for the measurement. The authors have mentioned that the middle row has been chosen as it is less affected by non-uniform coupling [93]. The best performance of the fabricated array is achieved when the rectifier (diode HSMS-2860) input power is 7 dBm, with the peak measured total efficiency occurring at 5.9 GHz, reaching a value of 72%, as shown in Figure 1.11 (c). To showcase the wide-angle capability of this design, measurements were conducted at various incident angles, ranging from 0° to 60°. The minimum measured total efficiency was at 60°, with value of 60% at the rectifier's input power level of 7 dBm.

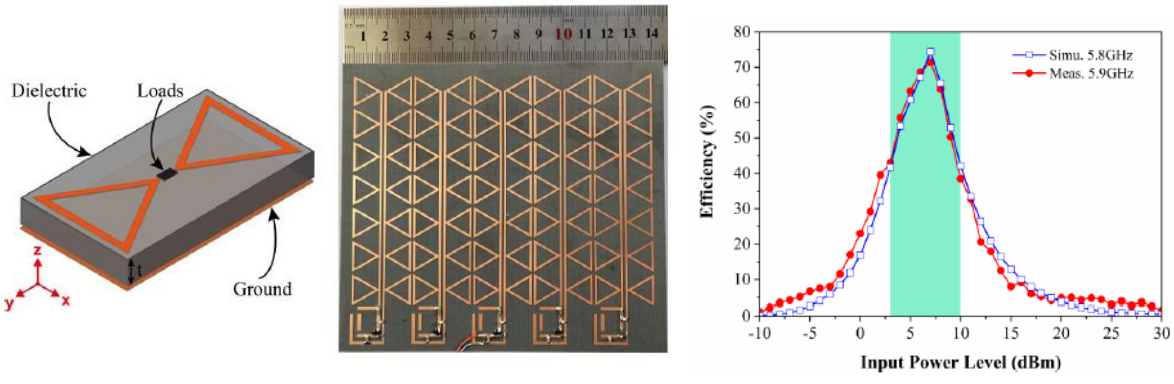

(a) (b) (c)

Figure 1.11 (a) Geometry of a wide-angle unit cell, (b) prototype of the 5×7 array, and (c) comparison of the simulated and measured efficiencies [93].

In addition to the works presented in this chapter, several other studies have employed the interconnected cells method [94-97]. However, these designs generally

achieve high efficiency at relatively high input power to their rectifiers, while their performance tends to decline at lower input power levels. Furthermore, some of these works incorporate multiple lumped elements or rectifiers in their design, for different objectives [94, 95, 97]. For instance, in [94], the authors used two resistive loads, which were later replaced by two rectifiers within their design, enabling dual-band operation—each rectifier operating at a different frequency. In [95, 97], one of the objectives was to achieve polarization insensitivity. To accomplish this, the design was made symmetric by interconnecting the cells along both the x-axis and y-axis. As a result, two lumped elements (later replaced by rectifiers) were incorporated into the design. However, the use of multiple lumped elements or rectifiers may introduce higher losses.

Table 1.2 summarizes the advantages and disadvantages of the popular methods for designing metasurface RF energy harvesters that integrate a rectifier circuit into their design, as presented in this chapter.

Table 1.2 Comparison of popular methods to design a metasurface harvester with integrated rectifiers.

Design	Method	Advantages	Disadvantages
Multi-layer	DC-combining	+ Simplicity of DC-combining network design	- Received power per cell may be not enough to turn a diode on - Fabrication difficulties due to its multi-layer aspect - Necessities of incorporating via/vias
	RF-combining (including feeding network)	+ Collecting power from multiple cells + Received power per cell can be enough to turn diode on	- Additional combining network - Complexity in designing feeding network - Fabrication difficulties due to its multi-layer aspect
Planar	Direct matching	+ Omits the need of additional combining network + One layer structure and compact + Via free	- Multiple diodes within metasurface design - Design complexity
	RF-combining (interconnected cells)	+ No need of additional combining network + One layer structure and compact + Simplicity + Low cost of manufacture + Via free + Collecting power from multiple cells	- Potential sensitivity to fabrication errors (depends on the design)

As can be seen in Table 1.2, the interconnected cells method is a promising solution to increase the collected power at the input of a rectifier while maintaining a planar design. This approach helps to avoid fabrication complexity and further losses.

To the best of this thesis' author's knowledge, the majority of works based on the interconnected cells method have not presented the performance of the metasurface finite array individually, but rather in conjunction with the rectifier. However, as both the metasurface and the rectifier are part of the RF energy harvester, it is prudent to optimize

them individually (at the same target frequency) so as to attain the highest possible total efficiency.

1.6 Conclusion

In this chapter, an introduction on energy harvesting and the various energy sources has been provided. Then, the main characteristics of RF energy harvesting have been discussed. A large part of this chapter was further dedicated to present and compare the various design principles of RF energy harvesters. In particular, focused on metasurface-based RF energy harvesters for desirable (and tunable) physical properties. Within the domain of metasurface RF energy harvesters, we explored a wide range of literature to highlight the characteristics of various architecture choices; among those discussed were planar and multilayer designs, harvesters with and without a rectifier, as well as DC and RF-combining networks. Aiming for a compact and simple design, the interconnected cells method has been selected as a promising technique to achieve a planar metasurface RF energy harvester in this thesis. However, enhancing its capturing efficiency remains challenging while minimizing the number of lumped elements used in the metasurface design.

Thus in the next chapter, we focus only on designing our efficient single-band metasurface harvester operating at 2.45 GHz, and discuss its design steps. In addition, we will propose a method to improve the capturing efficiency of the structure, and implement it into the design to validate its effectiveness.

2 An Efficient Single-Band Metasurface Harvester for IoT Applications

2.1 Introduction

As discussed in Chapter I, a simplified metasurface RF energy harvester consists of a metasurface for harvesting the ambient RF energy and a rectifier to convert it to DC. The highest total efficiency can be attained when both the metasurface and the rectifier operate efficiently at the same frequency. To achieve this, they can be optimized individually. In this chapter, we propose an efficient planar metasurface RF harvester and focus on evaluating its performance independently from a rectifier. To that end, the latter is temporarily replaced by a resistive load with the same impedance, which allows us to focus on optimizing the capturing efficiency of the metasurface.

As the ambient radio frequency energy is usually low, it is necessary to collect most of it, which is made possible by the interconnected cells method that helps to increase the collected RF energy level. However, improving the total efficiency of an ambient RF energy harvester can still be challenging. To overcome this challenge, our objective is to minimize losses in the dielectric and metallic components while maximizing the concentration of the absorbed power into a resistive load, which results in the improvement of the capturing efficiency of the metasurface harvester.

This chapter describes the design steps of the proposed planar efficient single-band metasurface harvester for energy harvesting applications based on the interconnected cells method. First, the unit cell design is presented; second, the supercell discussion is detailed, and an intermediate step in the design process of the metasurface harvester is proposed to enhance its capturing efficiency. Following this, a finite array, with the additional step design, is discussed. Then, the measurement result of the fabricated proposed structure is presented. Finally, a methodology is obtained based on the proposed design steps to increase the collected power by a metasurface harvester.

2.2 Metasurface Unit Cell Design

As mentioned, metamaterials/metasurfaces are generally periodic structures composed of unit cells designed to manipulate electromagnetic waves. In this thesis, the unit cell geometry

is carefully designed to absorb most of the incident RF energy. A key aspect of designing the unit cell is determining the operating frequency based on the intended application. For the proposed single-band metasurface harvester we target the Wi-Fi band at 2.45 GHz, based on its wide availability and various associated applications explained in Chapter I, to capture the ambient energy. Once the operating frequency is established, the geometry and resonant characteristics of the unit cell can be optimized for the desired frequency.

Referring to the design steps of the proposed metasurface harvester described in the introduction, we now focus on its fundament, namely the unit cell. In the first step, the geometry of the unit cell is presented.

The unit cell is depicted in Figure 2.1, and its geometry has been designed and optimized so as to achieve a high absorption efficiency at the desired frequency while being compact and simple. The top layer of the proposed unit cell is composed of two rectangular metallic rings facing each other, separated by a gap of width "g", the corresponding parameters are provided in Table 2.1. The motivation behind the rectangular rings is to enable tuning the resonance frequency by independently adjusting the rings' dimensions, which will be discussed later in detail in the parameter study.

As mentioned in Chapter I, in the interconnected cells method, adjacent unit cells from one or two directions are connected to one another, so the resistive load is positioned at the end of the connecting line [91, 93, 94, 96, 98]. Accordingly, in the proposed unit cell design, the two microstrip lines along the x-axis are located in the middle of the unit cell, each attached to its respective ring, as shown in Figure 2.2 (b). The width of the microstrip lines in the metallic rings is denoted "W". A resistor of R_{load} = 700 Ω is positioned at one edge between the two strips. Its value was obtained by optimizing the absorption efficiency at the operating frequency. Placing the resistor at the end of the gap allows for its future replacement with a suitable rectifier circuit while maintaining a single-layer design.

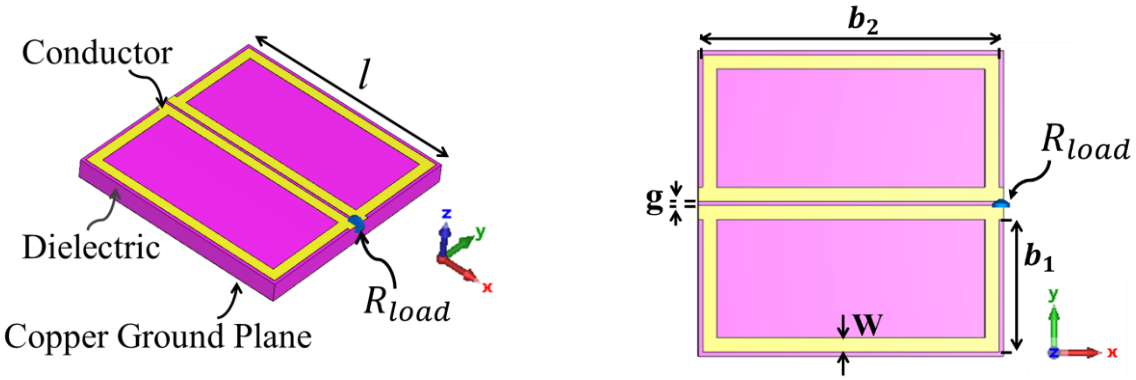

(a) (b)

Figure 2.1 Geometry of the proposed unit cell: (a) 3D view; (b) Top view.

Table 2.1 Parameters of the proposed metasurface unit cell.

Parameter	Description	Value
g	Width of the gap between the two microstrip lines	0.35 mm
l	Periodicity of the cell	27.3 mm
b_1	Length of the rectangular ring in the y-direction	11.8 mm
b_2	Length of the rectangular ring in the x-direction	26.5 mm
W	Width of the strip lines	1.26 mm
R_{load}	Resistive load	700 Ω

The copper thickness in the unit cell design is 0.035 mm. The periodicity of this square unit cell is 27.3 mm ($\approx 0.22\ \lambda_0$), which is more compact in comparison with [91, 93, 96-98].

For electromagnetic waves to be absorbed efficiently by a metasurface, its surface impedance must match that of free space. The goal is to increase the amount of usable energy collected and not let the absorbed energy be dissipated in the substrate. As a result, a low-loss dielectric should be chosen to serve this goal. Arlon DiClad 880, with permittivity equal to 2.17, a loss tangent of 0.0009, and a thickness of 2.36 mm, has been chosen as the substrate due to the desired low-loss property and its availability in the lab. To satisfy the impedance matching between the metasurface harvester and free space, the resistive load (R_{load}) is introduced into the design. By carefully choosing the load value, the reflection of the incident electromagnetic waves is minimized, thereby enabling maximum energy absorption by the metasurface. Note that the resistive load not only facilitates impedance matching but also serves as an energy collection element within the metasurface.

The polarization of the incident plane wave is along the y-axis. The design and optimization of the proposed metasurface are obtained using the EM simulation software CST Studio Suite, with a full-wave frequency domain solver. It is important to mention that the unit cell is simulated under periodic boundary conditions (see Figure 2.2 (a)) for emulating the infinite array in the x-y plane while a normal incident plane wave illuminates the structure towards the –z-axis.

The magnitude of the simulated reflection coefficient for the proposed metasurface unit cell when R_{load} = 700 Ω is depicted in Figure 2.2 (b), where the minimum reflection coefficient is -20 dB at 2.45 GHz. In the absence of the resistive load within the metasurface harvester, the absorption efficiency significantly decreases. This occurs because the surface impedance of the metasurface cannot be effectively matched to that of free space (Z_0=377 Ω). As a result, most of the incident RF power is reflected back rather than being absorbed by the metasurface. This is depicted in Figure 2.2 (b), which demonstrates the vital role of the resistive load in enhancing the performance of the proposed metasurface harvester at the desired frequency.

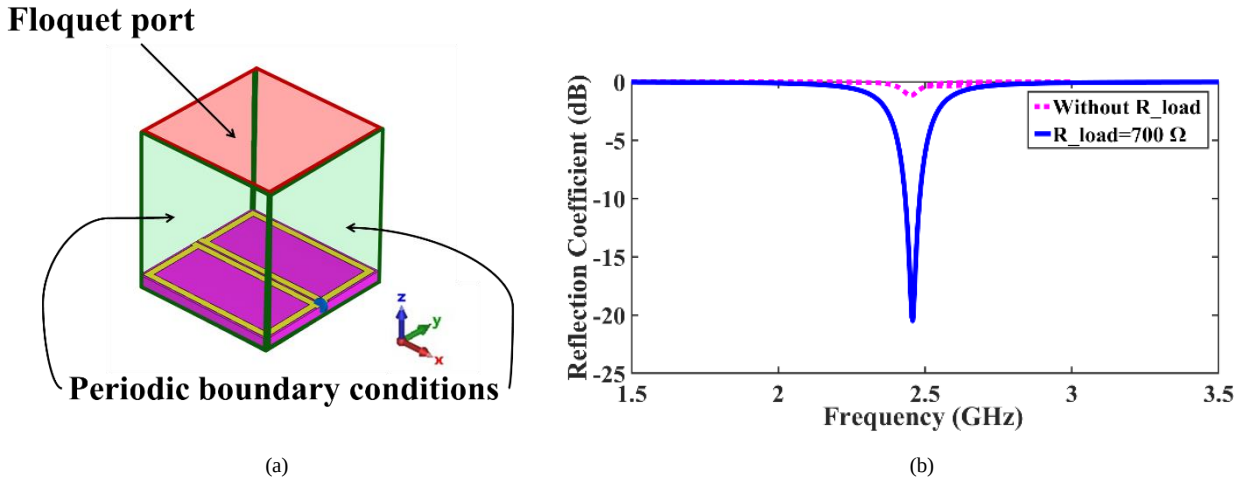

(a) (b)

Figure 2.2 (a) Periodic boundary conditions of the unit cell, and (b) comparison of simulated reflection coefficients of the proposed unit cell with Rload = 700 Ω and in the absence of the resistor.

The absorption efficiency of the proposed metasurface harvester (Equation (1.7)) equals 99% at 2.45 GHz (near unity absorption). Figure 2.3 shows the distribution of the absorbed RF power, of which less than 5% is dissipated in the metallic parts and dielectric substrate, as well as the fraction of power successfully collected by the resistor (94% at 2.45 GHz). The capturing efficiency is calculated according to Equation (1.9) of Chapter I, which is restated for convenience below:

$$\eta_{MS} = P_{dl}/P_{in} \tag{2.1}$$

P_{in} is the available incident power over the metasurface area. P_{dl} is the power delivered to the load and can be calculated by:

$$P_{dl} = \frac{{V_{RMS}}^2}{R_{load}} \tag{2.2}$$

with V_{RMS} denoting the root mean square (RMS) voltage across the resistive load (R_{load}).

The full width at half maximum (FWHM) absorption bandwidth ($\triangle f$) is 0.154 GHz (2.38 to 2.534 GHz) for the proposed single-band unit cell, as shown in Figure 2.3. Its quality-factor (Q-factor) can be calculated by the equation below [99-101].

$$Q(f) = \frac{f}{\triangle f} \tag{2.3}$$

In this equation, f is the resonance frequency where the maximum absorption occurs. Therefore, the Q-factor for the proposed unit cell, with the corresponding center frequency of 2.45 GHz, is 16. The Q-factor is introduced here as a metric to assess the broadband absorption characteristics of the design.

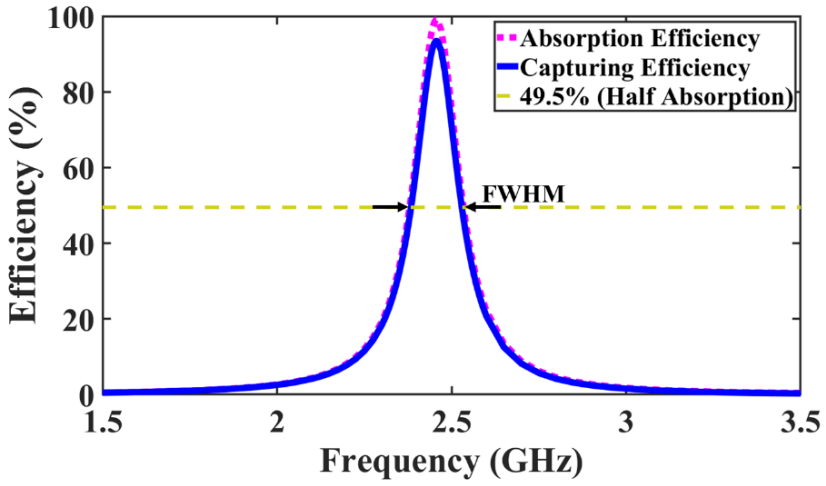

Figure 2.3 Simulated efficiencies of the proposed unit cell.

An additional study is carried out to evaluate the impact of the line width "W" on the performance of the design. In Figure 2.4 (a), the rectangular rings have inner and outer lengths of b1-W and b1 along the y-axis, and b2-W and b2 along the x-axis, respectively. Figure 2.4 (a) indicates, with a red dashed line, the average length La1 of the inner and outer length of the ring. La1 comprises the lengths of two rectangular rings, excluding the two microstrip lines in the middle and the gap "g" between them; see also Equation (2.4). As the line width "W"

increases, the inner length decreases while the outer length remains constant, leading to an overall reduction in La1. In addition, by increasing the microstrip widths and keeping the length b1 fixed, the rings are getting closer to the edge of the cell, and, as a result, the gap between the adjacent cells along the x-axis decreases. Figure 2.4 (b) illustrates the impact of varying the width "W" on the performance of the proposed unit cell: An increase in W results in a lower resonance frequency, indicating that the reduced gap between neighboring cells has a higher impact on the frequency than the reduced average length La1 (see Equation (2.4) below).

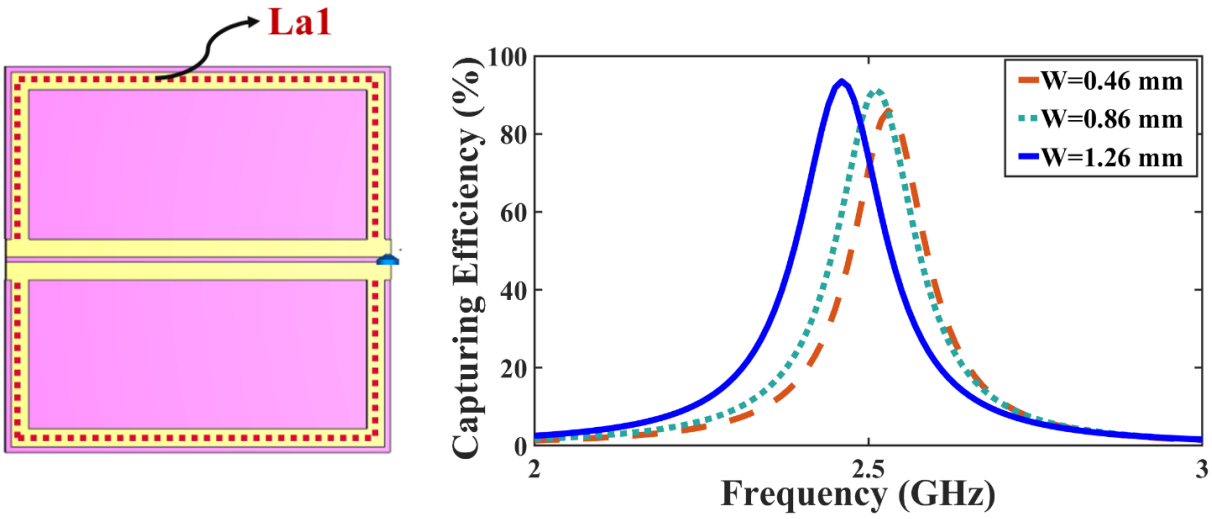

(a) (b)

Figure 2.4 (a) The average length La1 is indicated with a red dashed line, (b) the impact of varying "W" on the performance of the single-band unit cell.

$$La1=4\times b_1+2\times b_2-4\times W \tag{2.4}$$

Table 2.2 summarizes the Q-factors of each design with the corresponding width values "W" and the operating frequencies. As can be seen, increasing the width causes the associated Q-factor to decrease. The design has satisfactory performance with a width of 1.26 mm. While the study in Figure 2.4 (b) suggests that the absorption bandwidth of the design could be enhanced by increasing the width of the lines, this modification would require increasing the cell size. This is because, in the current design, b1 is already very close to the edge of the unit cell, leaving insufficient space to further expand its width.

Table 2.2 additionally provides the corresponding approximate characteristic impedances (Z_c) of different line widths for the single-band metasurface harvester. By increasing the width "W", the characteristic impedance of the microstrip line decreases, and

the capturing efficiency of the unit cell is increased slightly. The characteristic impedance of the microstrip lines is calculated using the ADS LineCalc tool.

Table 2.2 Performance values of the single-band design for various width values "W".

W (mm)	Frequency (GHz)	Capturing efficiency (%)	FWHM (GHz)	Q-factor	Z_c (Ω)
0.46	2.53	86	2.464-2.597 (0.133)	19	167
0.86	2.51	91	2.44-2.58 (0.14)	18	139
1.26	2.45	94	2.38-2.534 (0.154)	16	122

Figure 2.5 depicts the distribution of the surface current of the proposed unit cell at 2.45 GHz; from simulations at other frequencies, it can be concluded that the strongest current does indeed occur at 2.45 GHz. The two red arrows in Figure 2.5 represent the observed resonances. Each of these arrows extending between the two purple stars indicates the current amplitude going from least to highest (in the center) and again back to least. The length L_r of each resonance equals half the length of La1 (see Equation (2.4)),

$$L_r = 2\times b_1+b_2-2\times W = 47.58 \text{ mm} \tag{2.5}$$

where the values of b1, b2, and W follow from Table 2.1.

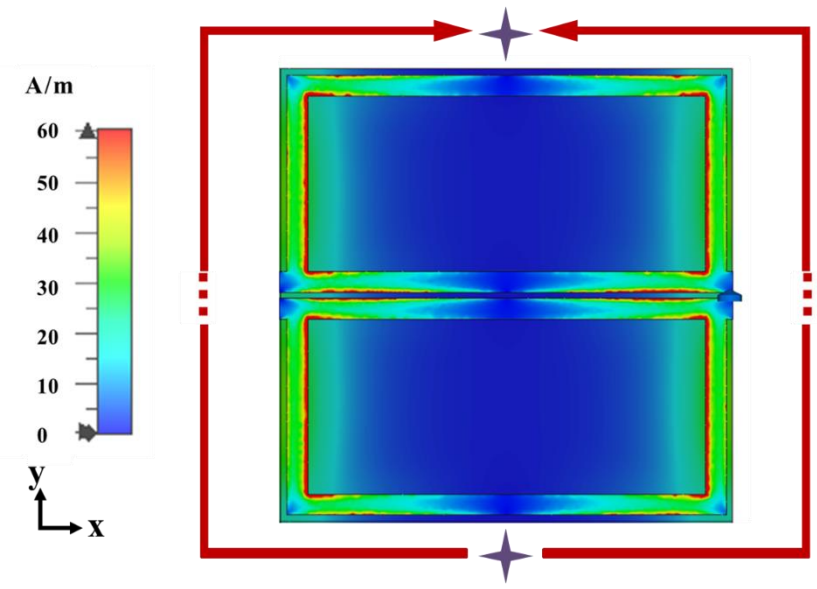

Figure 2.5 Surface current distribution at 2.45 GHz; the two resonances are indicated with the red arrows. (The dashed lines do not contribute to the length of L_r.)

We observe that L_r is close to the half-guided wavelength at the resonant frequency of 2.45 GHz (~46.82 mm), which is calculated according to [102]

$$\lambda_g = \frac{C}{f\sqrt{\varepsilon_e}}, \tag{2.6}$$

where c is the speed of light, f is the resonance frequency, and the effective permittivity ε_e equals approximately 1.71 and is obtained according to the formula below [102]:

$$\varepsilon_e = \frac{\varepsilon_r+1}{2} + \frac{\varepsilon_r-1}{2} F\left(\frac{W}{h}\right) - \frac{\varepsilon_r-1}{4.6}\frac{t/h}{\sqrt{w/h}} \tag{2.7}$$

$$F\left(\frac{W}{h}\right) = \begin{cases} (1+\frac{12h}{W})^{-0.5} + 0.04(1-\frac{W}{h})^2 & if\ \frac{W}{h} \leq 1 \\ (1+\frac{12h}{W})^{-0.5} & if\ \frac{W}{h} \geq 1 \end{cases} \tag{2.8}$$

with W and h denoting the width of the microstrip lines and the thickness of the substrate, respectively; with t denoting the thickness of the copper; and ε_r being the relative permittivity of the dielectric. Note that the design corresponds to the W/h ≤1 regime of Equation (2.8).

It is worth mentioning that if the mutual coupling between adjacent cells is too strong, it will influence the resonance frequency and its value will deviate slightly from the expected value based on L_r.

Figure 2.6 (a) shows the surface current vectors, with the zoom section indicating the differential output of the two microstrip lines in the middle. The differential impedance corresponding to the microstrip lines in the middle is approximately 121 Ω (calculated using the ADS LineCalc tool).

The power flow diagram in Figure 2.6 (b) depicts the distribution of the absorbed power within the proposed metasurface design. As intended, the majority of the power is concentrated in the resistive load, validating the metasurface's design for efficiently transferring the absorbed power to the resistor.

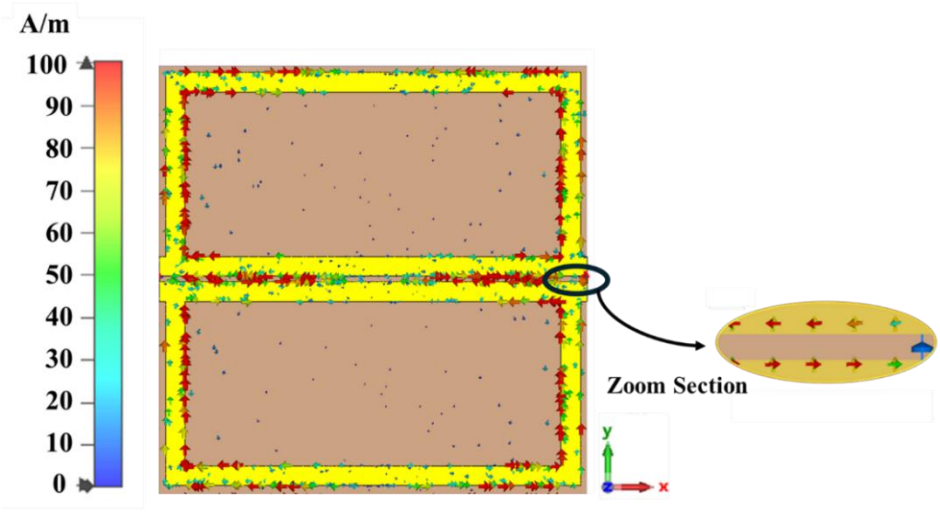

(a)

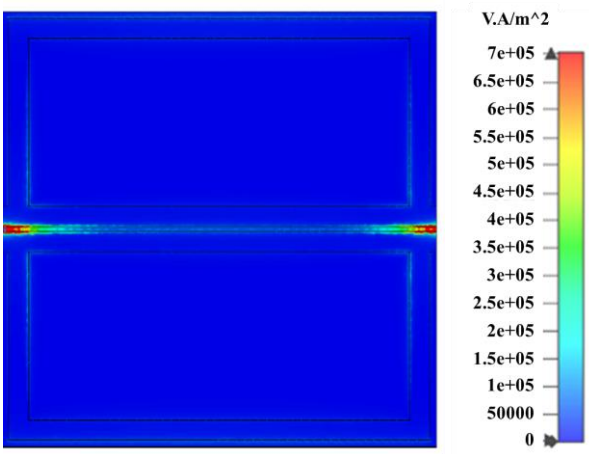

(b)

Figure 2.6 Simulated results of the proposed unit cell at 2.45 GHz: (a) the surface current vector distribution with the highlighted differential output, (b) the power flow distribution.

To ensure the optimal performance of the metasurface harvester, detailed parameter studies were undertaken. They will be discussed in the following section.

2.2.1 Parameter Study

During the design of the proposed metasurface harvester to capture the RF energy efficiently, parameter studies help identify the optimal combination of the geometric parameters (e.g., unit cell periodicity and metallic pattern dimensions) and the resistive load value. These optimizations ensure maximal concentration of the RF energy at the resistive load at the target frequency (2.45 GHz) and minimal losses in the metallic parts and dielectric substrate. In addition, parameter studies can demonstrate the sensitivity of the performance of

the metasurface harvester (absorption at the desired frequency) by varying the mentioned parameter values.

To identify the impact of each parameter on the capturing efficiency as well as on the resonant frequency, we vary each parameter alone while keeping the others fixed. The first parameter study was done on the impact of increasing b1 (length in the y-direction), as shown in Figure 2.7 (a). As seen in Figure 2.5, Lr is representing the length of a resonance; by increasing b1, Lr increases as well, and, as result, the resonance frequency decreases. Analogously, when b1 decreases, the resonance frequency increases. Analogously to the parameter study for b1, the impact of varying b2 (length in the x-direction) on the resonance frequency is depicted in Figure 2.7 (b), and the values are listed in Table 2.3. While qualitatively, the same behavior is observed, quantitatively, we notice that the resonance frequency is less sensitive to varying b2.

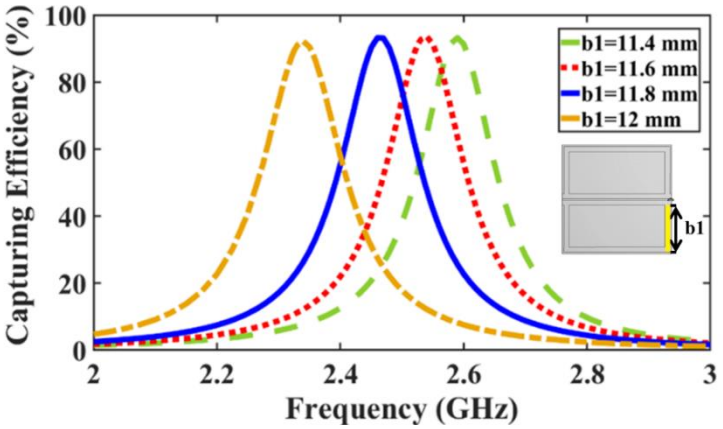

(a)

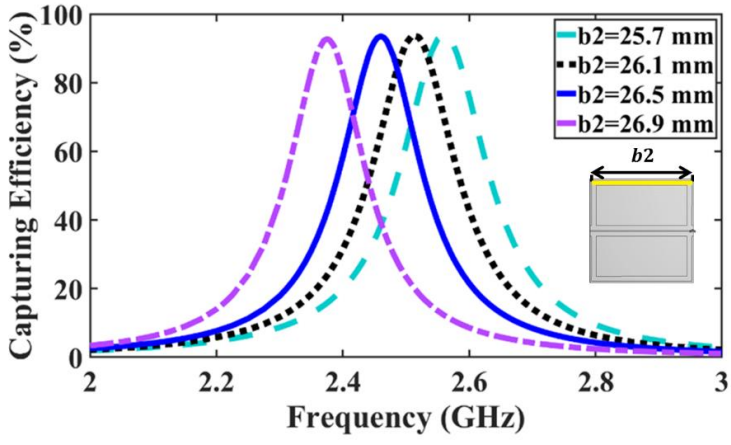

(b)

Figure 2.7 Impact on the performance of the cell by varying the lengths (a) b1 and (b) b2.

Table 2.3 Capturing efficiency and operating frequency as a function of b1 and b2.

b1 (mm)	Frequency (GHz)	Capturing efficiency (%)
11.4	2.59	~ 93
11.6	2.54	~ 93
11.8	2.45	94
12	2.34	~ 92
b2 (mm)	**Frequency (GHz)**	**Capturing efficiency (%)**
25.7	2.56	~ 93
26.1	2.51	~ 93
26.5	2.45	94
26.9	2.37	~ 92

The last parameter to examine is the gap "g" as indicated in Figure 2.8, and the values are listed in Table 2.4. By increasing "g", the coupling between the two microstrip lines decreases. However, this simultaneously alters the spacing between the adjacent cells, which increases the mutual coupling between the neighboring cells. This dual effect makes the frequency-dependent trends challenging to predict, as can be seen in Figure 2.8. However, it can be concluded that the unit cell with parameter "g" equal to 0.35 mm has the best capturing efficiency at the targeted frequency.

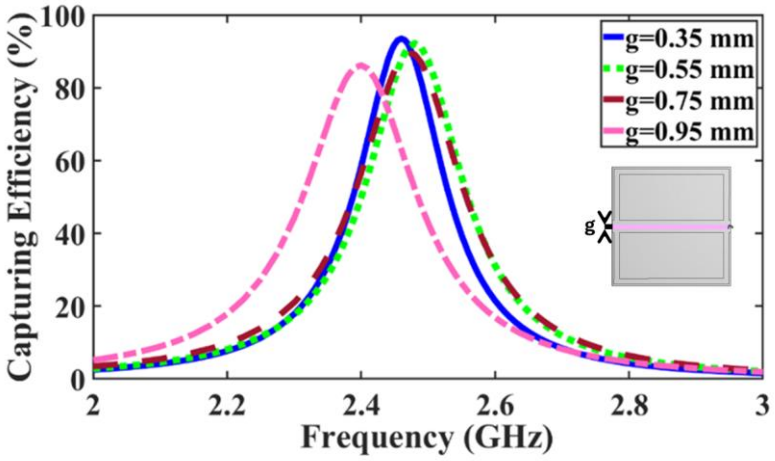

Figure 2.8 Impact on the performance of the cell by varying the gap between the two microstrip lines.

Table 2.4 Capturing efficiency and operating frequency as a function of g.

g (mm)	Frequency (GHz)	Capturing efficiency (%)
0.35	2.45	~ 94
0.55	2.8	~ 92
0.75	2.47	~ 89
0.95	2.4	~ 86

Note that the frequencies listed in Table 2.3 and Table 2.4 each correspond to the highest efficiency obtained. The parameter studies above illustrated the optimal combination for the discussed parameter values to collect the maximum available RF energy at the resistive load at the operating frequency of 2.45 GHz. Also, it showed the sensitivity of the performance of the metasurface harvester to the parameter varying, which can help to control the resonance frequency.

Following the unit cell design, the metasurface supercell design is next discussed.

2.3 Metasurface Supercell Design

As mentioned in the State of the Art in Chapter 1, the interconnected cells method has the key advantage of collecting RF power from multiple cells instead of a single one. Multiple unit cells connected to one another in a row, with the last cell also connected to a resistive load, are characterized as a supercell. Due to its larger area, a supercell naturally collects more power than a single cell. The power collected by the supercell is directed to a single resistive load, whose value is first the same as that obtained for the unit cell [91, 96].

The supercell of the proposed metasurface harvester comprises four interconnected cells (N=4) along the x-axis, as shown in Figure 2.9, where a single resistive load with the initial value of 700 Ω is placed at the end of the microstrip lines (in the gap) of the proposed metasurface unit cell. The supercell is designed in CST Studio Suite under periodic boundary conditions on both the x-axis and the y-axis, as depicted in Figure 2.9 (b).

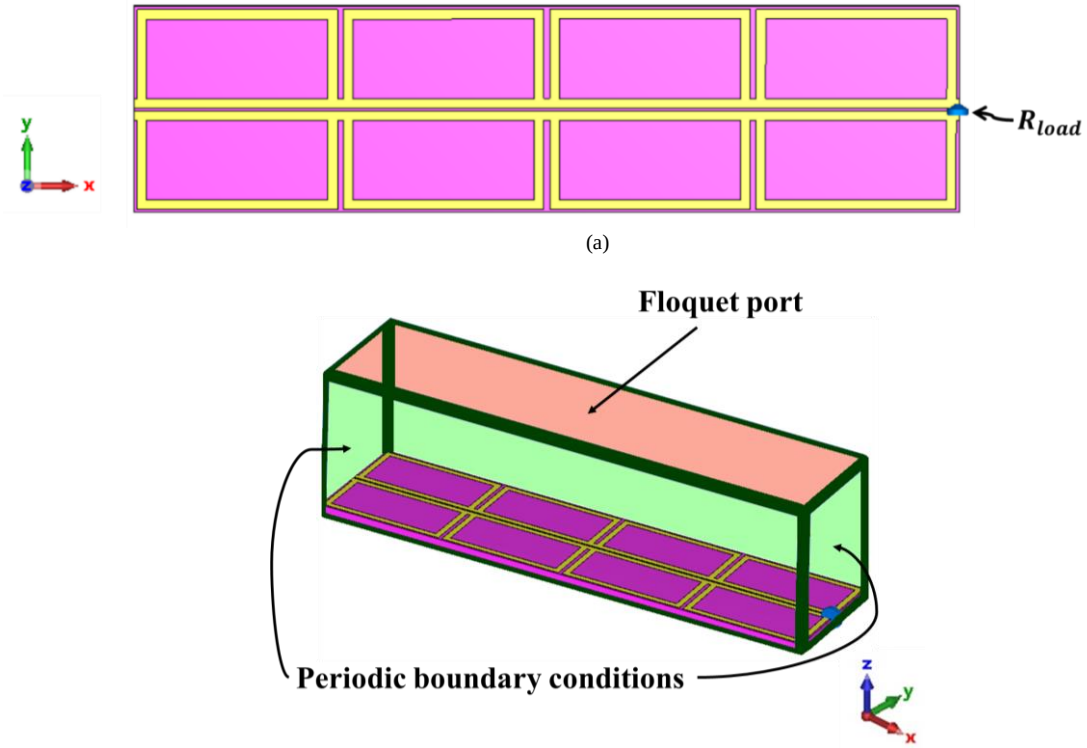

Figure 2.9 Schematic of the proposed supercell (a) top view, (b) 3-D view with the boundary conditions.

By keeping the resistive load value of the supercell the same as the unit cell, the capturing efficiency drops compared to that of the unit cell. This is due to the mismatched impedance between free space and the supercell, as the initial unit cell design was based on each cell being individually connected to a resistive load (recall that the simulation took place under periodic boundary conditions). The absorption features of the proposed metasurface structure are defined by the geometry of the metallic rings, the resistive load value, and the substrate characteristics. Taking all of this into account, an additional step in the supercell design is proposed, which is to reoptimize the resistive load value through a parameter study. The obtained optimum resistive load value is 115 Ω. The capturing efficiency of the single-band supercell with the optimum load compared to the one with the initial load value enhanced from 62% at 2.45 GHz to 92% at 2.49 GHz (see Figure 2.10). A slight frequency shift between the unit cell and the supercell simulation occurs because of the adjusted load value; this shift can be mitigated by adjusting the dimensions of the rectangular rings based on the parameter study (recall Section 2.2.1).

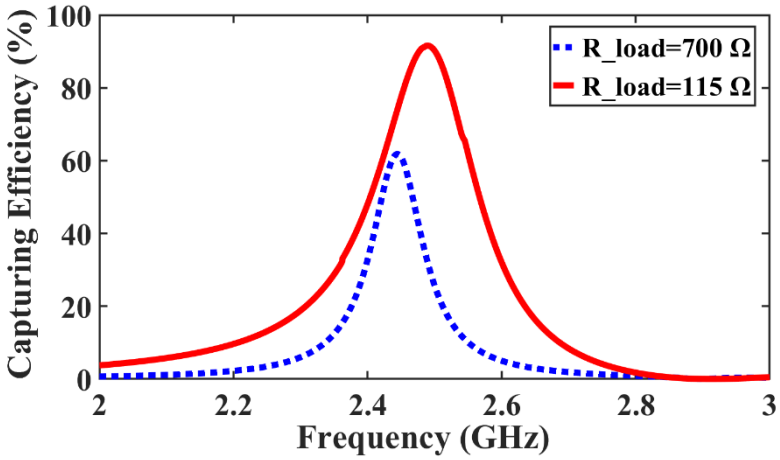

Figure 2.10 Comparison between the capturing efficiencies of the supercell for the optimum resistive load (115 Ω) and the initial resistive load value (700 Ω).

In Figure 2.10, the presented capturing efficiencies were for a supercell composed of 4 cells, with a resistive load value of 115 Ω. The capturing efficiency for the supercell configurations with N=2, 6, and 8 cells (all with a resistive load of 115 Ω) is 68% at 2.5 GHz, 86% at 2.47 GHz, and 79% at 2.46 GHz, respectively. Viewing the capturing efficiency as a function of the number of cells composing the supercell out of 4 unit cells yields an acceptable tradeoff between the capturing efficiency and the used surface area.

Following the supercell discussion, we can move to the last step in the metasurface harvester design, which is designing the finite array.

2.4 Metasurface Finite Array Design

For the final simulation step in the metasurface design, a finite array containing 5×4 cells (5 rows; Middle Row, Row 1, and Row 2, with the latter two replicated across the middle row) was designed as depicted in Figure 2.11. The polarization of the incident plane wave is along the y-axis. A resistive load of 115 Ω is positioned at the end of each of the five rows. The choice of this resistance value comes from the optimization of the supercell (N=4). The choice of the size of the array depends on several factors, such as the maximum allowed device size for an intended application, the level of available input power, etc.

To the best of the author's knowledge, in the works on the interconnected cells method presented in [91, 94], the total measured efficiency of the middle row of their proposed finite array design was presented (metasurface included the implemented rectifier). However, going

further than these works, we not only analyze the middle row of the metasurface independently, that is, aside from the rectifier, but also the other rows in detail. This leads us to introduce the concept of "central rows" to evaluate the performance of the metasurface harvester with higher accuracy. We shall first explain this concept in detail and thereafter discuss the motivation behind its introduction.

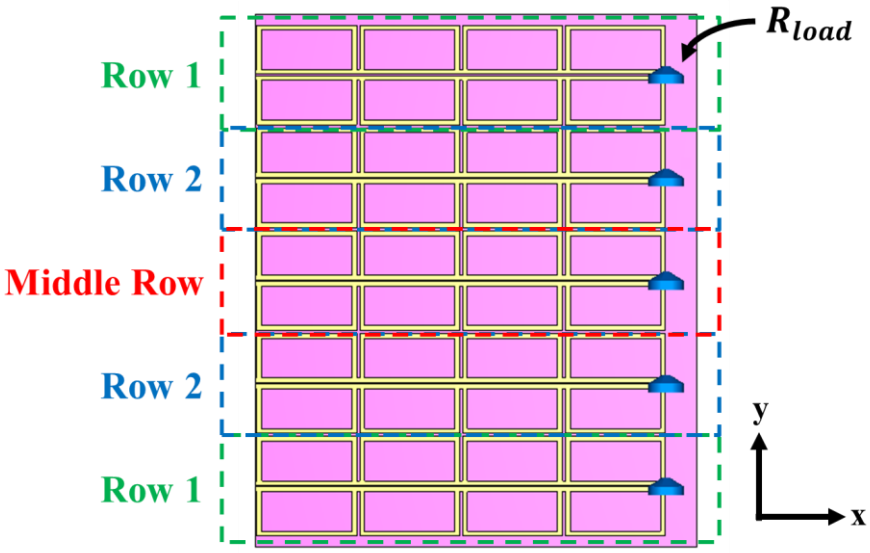

Figure 2.11 Proposed finite array with row labels.

The capturing efficiency of the finite array of the proposed metasurface can be calculated by Equation (2.1), where P_{in} is obtained by integrating the Poynting vector over the metasurface footprint. Figure 2.12 shows the comparison between the simulated capturing efficiency of each row (surface area equal to 0.00298 m²) with the initial (left) and reoptimized (right) resistive load values. The capturing efficiencies plotted in Figure 2.12 are tabulated in Table 2.5.

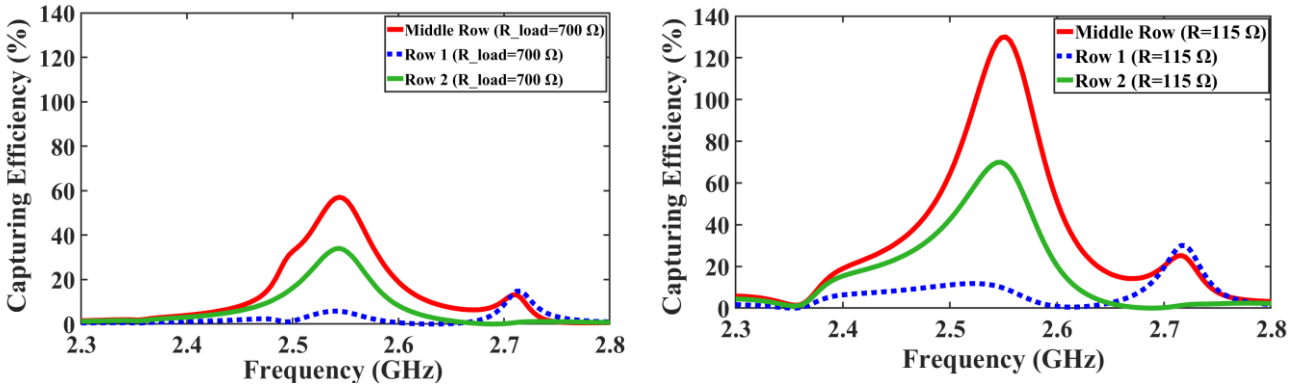

(a) (b)

Figure 2.12 Comparison between the simulated capturing efficiency of different rows for: (a) the initial R_{load} (700 Ω) and (b) the reoptimized R_{load} (115 Ω).

Table 2.5 Capturing efficiencies of different rows at 700 Ω and 115 Ω.

Row number	Frequency (GHz)	Capturing efficiency (%)	R_{load} (Ω)
1	2.54	6	700
2	2.54	34	700
Middle	2.54	57	700
1	2.52	12	115
2	2.54	70	115
Middle	2.54	130	115

Two key points can be derived from the comparative plots in Figure 2.12. First, focusing individually on the sub- Figure 2.12 (a) and (b), it can be seen that the capturing efficiency varies across the rows, with the middle row having the highest. Second, comparing the two sub-figures 12 (a) and (b) shows the increase of the capturing efficiency of each row when reoptimizing the resistive load value.

Regarding the second point above, it is important to note the difference between the supercell and finite array simulation conditions. When a supercell is simulated in periodic boundary conditions, infinitely many supercells are carefully positioned next to each other; as a result, there is a uniform mutual coupling among them. However, when simulating the finite array, the power distribution within the array is affected by the non-uniform mutual coupling among the cells. As a result, the middle row witnesses a higher collected power in comparison with the other rows; this is not only due to absorbing the direct incident power but also due to the coupled power from the adjacent rows around the middle one. This is demonstrated by the efficiency of the middle row (Figure 2.12b) which exceeds 100%! However, the capturing efficiency of the whole array is 58%. We must therefore take care to consider more than only the middle row for evaluating the performance of the final metasurface harvester. Indeed, as the edge rows are less efficient than the others (due to the absence of adjacent rows on each side), a sufficient number of central rows (the rows around and including the middle row) are required. Accordingly, the proposed finite array comprises five rows, of which the three central rows have the most similarity to the supercell simulation conditions. So, to have a more accurate conclusion on the performance of the proposed metasurface, we calculate the capturing efficiency of the central rows, which is more informative in comparison with previous works [91, 94, 96, 98] where only the middle row of the whole structure was considered.

The capturing efficiency of the central rows is equal to

$$\eta_c = \frac{\sum P_{dl\_i}}{P_{in\_c}} = \frac{P_{dl\_2}+P_{dl\_m}+P_{dl\_2}}{P_{in\_c}} \quad (2.9)$$

where *i* indicates the row number (either middle row or Row 2; see Figure 2.11), and P_{in-c} is the incident power over the surface area of the central rows, which equals 3 times the incident power of a single row $P_{in\text{-}r}$:

$$P_{in-c} = 3 \times P_{in-r} \quad (2.10)$$

Note that P_{in-r} has the same value for all rows as their surface areas are equal. Substituting Equation (2.10) into Equation (2.9) yields:

$$\eta_c = \frac{P_{dl\_2}+P_{dl\_m}+P_{dl\_2}}{3\times P_{in\_r}} \quad (2.11)$$

Which can be simplified to the average efficiency of the three central rows:

$$\eta_c = \frac{\eta_2+\eta_m+\eta_2}{3} \quad (2.12)$$

Where η_2, and η_m are the capturing efficiency of row 2 and the middle row, respectively.

Figure 2.13 depicts a comparison between the simulated capturing efficiency of the central rows of the metasurface array, with the initial resistive load value of 700 Ω and the reoptimized value of 115Ω. It can be seen that the capturing efficiency of the central rows of the finite array improved by 50% (from 40% to 90%) at 2.54 GHz.

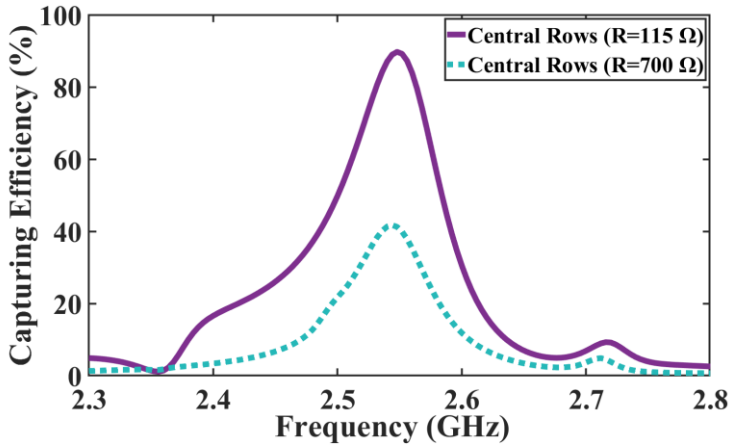

Figure 2.13 Comparison between the simulated capturing efficiencies of the central rows for the optimum R_{load} (115 Ω), and the initial R_{load} value of the unit cell (700 Ω).

The presented finite array simulation results demonstrate the impact of reoptimizing the resistive load value, which significantly improves the level of collected power. This aligns with the discussion presented for the supercell, validating the effectiveness of the proposed additional design step. However, due to the fact that the supercell was simulated under periodic boundary conditions, whereas the finite array was simulated with open boundary conditions, there is a slight shift in the resonating frequency. To adjust back the operating frequency to 2.45 GHz, the dimensions of the rectangular rings can be modified based on the parameter studies in Section (2.2.1). One may remark that the proposed design is polarization sensitive, as the capturing efficiency of the array excited by a normal incident plane wave with polarization along the x-axis is zero.

The next step is to separately measure the metasurface so as to validate its behavior. This is in contrast to the way of the presentation of most of the works that used the interconnected cells method [91, 94, 96, 98], where they presented the measured total efficiency (the product of the capturing efficiency of the metasurface and rectification efficiency). However, as stated at the outset, our objective is to analyze the behavior of the metasurface design and the rectifier independently to make sure that the designed metasurface and rectifier operate efficiently at the same target frequency and to prevent mismatches caused by frequency shifts. Accordingly, the next section presents the fabrication and measurement setup, as well as the results, for the proposed metasurface design only; the rectifier is discussed later in Chapter III.

2.5 Realization and Measurement

In order to evaluate the capturing efficiency of the designed metasurface harvester at the operating frequency, the collected power in the resistive load of the finite array needs to be measured. However, due to the limitations of the conventional RF measurement instruments and the geometry of the proposed structure, it is necessary to introduce a few modifications in the metasurface design and validate them by simulation before proceeding with the measurement.

As shown in Figure 2.1 and Figure 2.11, the resistor is placed between two metallic strips of the upper layer. But to perform this measurement, we use a 50 Ω power sensor (Keysight U8488A 10MHz - 67GHz power sensor.) Moreover, the gap between the two strips

is small. Consequently, the design was modified to measure the output power. It is essential to highlight that these modifications are temporary and, in the future, will not be necessary as the 115 Ω resistor will be replaced by a rectifier implemented on the same layer as the metasurface.

The adjustments to the metasurface design are restricted to its middle row, as modifying all rows would introduce significant mismatches, leading to a substantial reduction in the capturing efficiency of the metasurface finite array. Indeed, this row is less affected by edge effects and is modified to serve as a representative row to evaluate the capturing efficiency, identify the frequency at which its peak occurs, and compare the measurement results with the simulation incorporating the same modifications. To do so, we aim to measure the RF power collected in the resistor of the middle row of the finite array, and the other rows are terminated with a 120 Ω Surface Mount Resistor (SMD) each due to their availability in the lab. Thus, the 115 Ω load at the end of the middle row is removed, and an oblique extension of the lines is added to connect two 50 Ω SMA connectors. In the simulation, each connector is substituted with a 50 Ω load positioned between the end of the lines (points A and B) and the ground, as shown in the zoomed-in section of the middle row in Figure 2.14 .

It is noted that the simulation has been performed while taking into account the modifications made for measurement purposes. As can be seen in Figure 2.14, the substrate is cut to accommodate the shape of the connectors. These modifications result in a drop in the simulated capturing efficiency of the middle row from 130% at 2.54 GHz to 106% at 2.54 GHz, as illustrated in Figure 2.15. However, their only purpose is to enable measuring RF output power and comparing the performance of the metasurface design with the simulation.

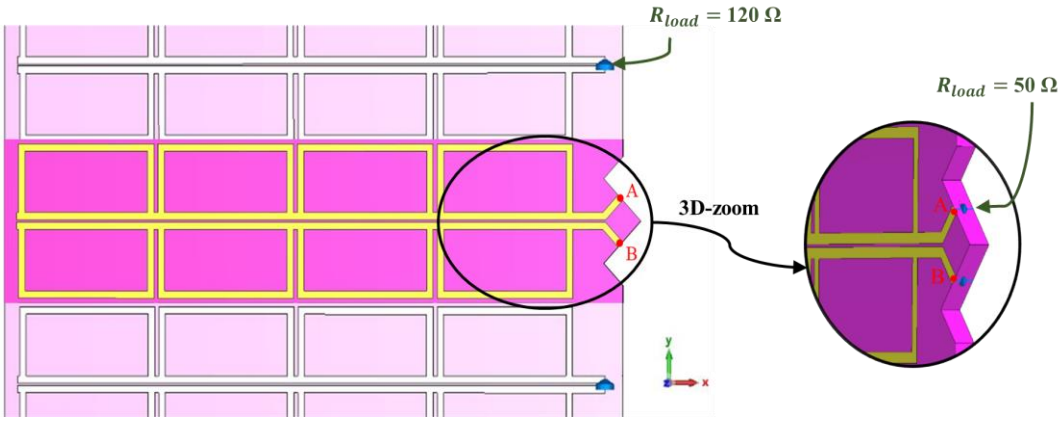

Figure 2.14 Temporary modification of the middle row of the metasurface design.

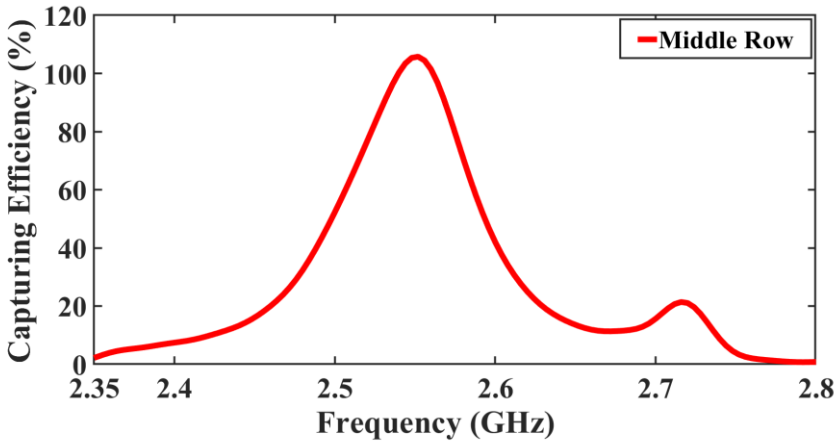

Figure 2.15 Simulated capturing efficiency of the modified middle row of the proposed metasurface finite array.

The array composed of 5×4 cells with the mentioned modifications was fabricated with a LPKF ProtoLaser machine on a 2.36 mm Arlon DiClad 880 dielectric substrate, as illustrated in Figure 2.16; the copper thickness is 0.035 mm, and the area of the substrate is 141.5 ×121 mm^2.

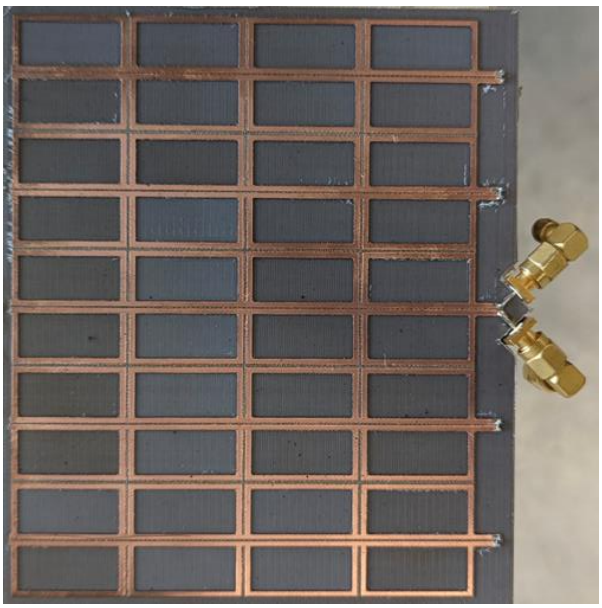

Figure 2.16 Prototype of the proposed modified metasurface design with the soldered connectors.

In Figure 2.17, the full measurement setup in the anechoic chamber is shown, and the configuration parameters at 2.54 GHz are provided in Table 2.6. The incident power on the middle row of the metasurface design is obtained by the Friis formula:

$$P_{in} = \frac{G_h.Ps}{4\pi R^2} \times A_s \tag{2.13}$$

G_h is the gain of the horn, and *Ps* is the emitted power; R is the distance between the horn and the prototype; and A_s is the effective area of the metasurface array, which, in this measurement, is the area of the middle row. The fabricated metasurface is located in the far field distance so that the wave emitted by the horn is locally considered a plane wave.

Table 2.6 Transmitter and Propagation Parameters.

Description	Value	Unit
Distance between antenna and prototype	2.39	m
Gain of the horn at 2.54 GHz	6.5	dBi
Emitted power measured at the horn input	24.4	dBm
Effective area of the metasurface array	0.00298	m^2

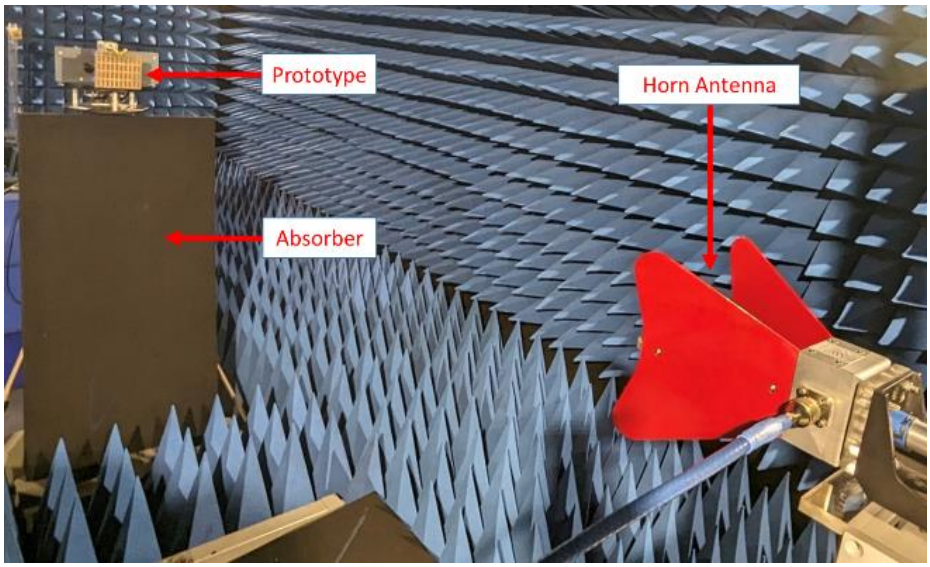

Figure 2.17 Measurement setup in the anechoic chamber.

The capturing efficiency of the fabricated metasurface harvester is obtained by Equation (2.1), where the collected RF power for the middle row P_{dl} is the addition of the power measured at each connector (the other being connected to a 50 Ω load). The measured capturing efficiency under normal incidence is 61% at 2.49 GHz, as presented in Figure 2.18.

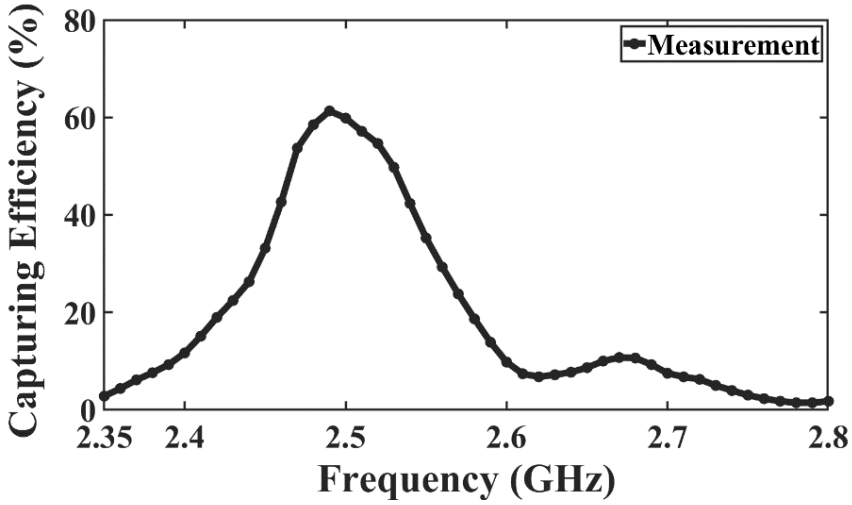

Figure 2.18 The capturing efficiency of the middle row of the fabricated prototype.

The observed discrepancies between the simulated and measured performance of the proposed metasurface harvester (see Figure 2.15 and Figure 2.18) can be mainly attributed to the sensitivity of the design to the parameter dimension changes (which may occur, among other reasons, due to fabrication errors). The observed change in performance could be due to the fact that by varying the design parameters, the mutual coupling between the cells is impacted.

We observe that the simulated capturing efficiency of the central rows resembles more closely the measured capturing efficiency of the middle row. Recalling the definition and the formula for the efficiency of the central rows (Equation (2.12)), the latter is defined as the arithmetic mean of the efficiencies of the middle row and its two neighbors. In Figure 2.19, the measured capturing efficiency of the middle row and the simulated capturing efficiency of the central rows are compared; note that the figure refers to the latter as “an average row”, a terminology that we introduce to emphasize that we treat the three central rows as a single row when referring to their averaged capturing efficiency. The observed agreement in Figure 2.19 can be due to the mutual coupling in the fabricated array introducing a behavior resembling that of the average row.

In Figure 2.19, for the normal incidence, FWHM capturing bandwidth for the simulated average row is 0.092 GHz (2.494 to 2.586 GHz), and 0.11 GHz (2.45 to 2.56 GHz) for the measured middle row. The corresponding Q-factor of the former is 27.6 and of the latter 22.6, with the center frequencies of 2.54 GHz and 2.49 GHz, respectively.

Knowing the performance of the device as a function of the angle of incidence is crucial information for the application, so Figure 2.19 shows the comparison between the simulated and measured capturing efficiency of the proposed metasurface harvester at two oblique incidence angles. The corresponding data supporting a good agreement between measurement and simulation is given in Table 2.7.

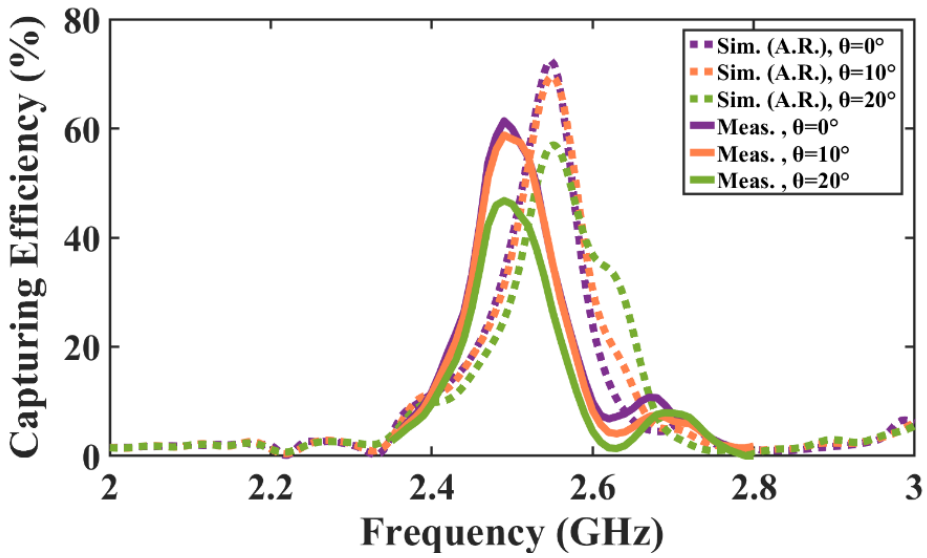

Figure 2.19 Comparison between simulated average row (A.R.) and measured capturing efficiency (middle row) at different incidence angles.

Table 2.7 Simulated and Measured Capturing Efficiency as a Function of the Incident Angle.

Incident angle	Capturing efficiency (simulation)	Frequency (simulation)	Capturing efficiency (measurement)	Frequency (measurement)
0°	73 %	2.54 GHz	61 %	2.49 GHz
10°	69.4 %	2.54 GHz	59 %	2.49 GHz
20°	57 %	2.55 GHz	47 %	2.49 GHz

As can be seen in Table 2.7 a 0.05 GHz frequency shift between the simulated and measured results is observed (2% deviation from 2.54 GHz). This shift could be due to other errors, such as in the substrate thickness (+-0.076 mm) or the permittivity (+-0.02). In conclusion, by analyzing the single-band metasurface design in detail, we were able to evaluate its performance.

As discussed in Chapter I, various methods have been explored to enhance the performance of RF metasurface harvesters. In this chapter, our proposed design offers several advantageous features. It is more compact with respect to λ_0 (free space wavelength) in comparison to [38, 42, 78, 91, 93, 96-98, 104], and it maintains a planar structure, thereby eliminating the challenges associated with multi-layer configurations and vias [40, 42, 45, 78, 86, 103, 104]. Additionally, our metasurface harvester minimizes the use of lumped elements within the finite array compared to [42, 45, 94, 97, 104], which helps reduce further losses when the resistors are replaced by rectifiers in subsequent stages.

Furthermore, we proposed an intermediate design process aimed at improving the capturing efficiency of metasurface harvesters based on the interconnected cells method. This approach was validated through its implementation in our single-band design. The following section outlines the key steps of our design methodology.

2.6 Methodology Summary

In planar structures, the interconnected cells method made it possible to increase the collected RF energy level at the resistive load. However, improving the total efficiency of an ambient RF energy harvester can be challenging. Our proposed solution to this challenge is a methodology to improve the capturing efficiency of such interconnected cells energy harvesters.

As the metasurface absorber is a finite periodic structure, firstly, the unit cell is designed under periodic boundary conditions, with the unit cell connected to a resistive load. This first step enables a fast pre-dimensioning of the geometry of the cell in order to collect the maximum possible RF ambient energy at the load at the targeted frequency.

Next follows the simulation of the supercell, a group of interconnected cells, which is connected at the end to a single resistive load with the same value as the unit cell, as shown in [91, 96]. This step aims to determine the number of cells of the supercell while keeping the same geometry as that of the unit cell. However, the performance of the unit cell and supercell are slightly different as each unit cell features a single resistor, whereas each supercell – consisting of multiple unit cells – also features a single resistor. Thus, the matching condition between the structure and free space needs to be re-satisfied. So, we propose an additional step with the optimization of the resistive load value of the supercell. In this way, its capturing

efficiency improves. The supercell design and the associated optimization procedure lead us to the last step, namely simulating the finite array.

2.7 Conclusion

In this chapter, a compact, efficient single-layer metasurface RF harvester operating at 2.45 GHz (Wi-Fi band) for energy harvesting applications was proposed. The unit cell of the metasurface harvester was presented; it showed near-unity absorption, owing to its geometry and the optimum resistive load (chosen so as to match the surface impedance to that of free space). Further, a parameter study was carried out to investigate the performance of the proposed unit cell and its sensitivity to varying parameters; this allowed us to identify the optimal geometry for the target frequency.

A supercell consisting of 4 unit cells and equipped with the load initially obtained for the unit cell was designed and simulated. Given the low level of ambient RF energy, an intermediate step in the design process of the metasurface harvester is introduced to increase the amount of collected power. Concretely, the resistive load value was reoptimized, whereby the simulating capturing efficiency of the supercell improved from 62% at 2.45 GHz to 92% at 2.49 GHz.

A finite array consisting of 5 rows was designed, and each row was analyzed in detail. We further introduced the new concept of "central rows", which aggregate the middle row and its two adjacent rows. The principal idea behind the "central rows" is to average the efficiency of its three defining rows to account for the fact that each of those rows collects a different amount of power at its load. The intermediate design process described in the previous paragraph was implemented on the proposed metasurface array, whereby the capturing efficiency of the central rows increased from 40% to 90% at 2.54 GHz (by 50%).

The proposed structure is very simple to fabricate, without any lumped element except the resistors that serve to simulate the rectifier input impedance. To validate the concept, a finite array of 5×4 cells was fabricated, and to perform the measurement, modifications were introduced in the metasurface design. It was also observed that the performance of the middle row showed sensitivity to varying parameters, which was much less the case for the central rows. Indeed, we found that the simulated efficiency of the central rows was in good agreement

with the measured efficiency; under normal incidence, the former is 73% at 2.54 GHz, whereas the latter is 61% at 2.49 GHz. It has been further demonstrated that the structure behaves well under oblique incidence up to an angle of 20°.

By following our design steps, we successfully conducted an independent analysis of the performance of our proposed metasurface harvester. Based on the content of this chapter, the work in [105] has been presented.

In the next chapter, the resistive load of the metasurface will be replaced with a rectifier to collect the DC output. Accordingly, the design process of the proposed rectifier and its simulation, along with its fabrication and measurement, will be discussed independently. In addition, the implementation of the proposed rectifier with the efficient single-band metasurface will be presented.

3 Proposed Rectifier and its associated performance with the Single-Band Metasurface

3.1 Introduction

As discussed in Chapter I and II, metasurface harvesters due to their favorable absorption features can serve as suitable receivers to collect ambient RF energy. In addition to the metasurface design performance, the design of a rectifier - whose purpose it is to convert the collected RF power to DC power - represents the second stage of the energy harvester design. Finally, the converted DC power is transferred to energy storage devices or used.

In Chapter II, we proposed a metasurface harvester whose captured RF energy is directed to a resistive load. Here, we replace the resistive load with a rectifier designed to convert the captured RF into DC power; to that end, the metasurface load value of 115 Ω equals the input impedance of the rectifier circuit.

In this chapter, the focus is on the design of a suitable rectifier for our proposed single-band metasurface. The proposed rectifier is designed to operate at 2.49 GHz, that is, at the measured operating frequency of the metasurface harvester.

We begin by presenting a brief background on rectifiers and their working principles including a discussion of the different rectifier topologies commonly employed [22, 106-108]. According to the number of diodes, the latter can be broadly classified into single-diode and multi-diode configurations. Following the background discussion, we present our differential rectifier featuring a Schottky diode that was chosen for its low threshold voltage, making it well-suited for harvesting the typically low ambient RF power. The goal of our design is to optimize its operation at relatively low input power levels.

Following the rectifier design and analyzing its simulated results, the fabrication and measurement of our design are presented. The fabricated rectifier is first tested independently to evaluate its performance before being connected to the proposed metasurface harvester.

Finally, the fabricated rectifier is connected to the previously fabricated metasurface harvester to form a complete RF to DC energy harvester. The corresponding measurements are presented and discussed.

3.2 Background on Rectifiers

Rectifier is a common component of many modern devices, where there is a need to convert alternating current (AC) to DC, which flows in one direction only. Examples of such devices include phone [109] and laptop chargers [110], power banks [103], gaming consoles [112]; their internal circuits generally operate on a stable DC power source, whereas outlets in households only provide AC. While rectifiers are adapted across a wide range of applications, their working principle remains fundamentally the same [113].

A simple rectifier for RF energy harvesting applications may comprise matching networks, rectifying components (such as diodes), dc pass filters, and, at its output, a load or storage device [114, 115] as shown in Figure 3.1.

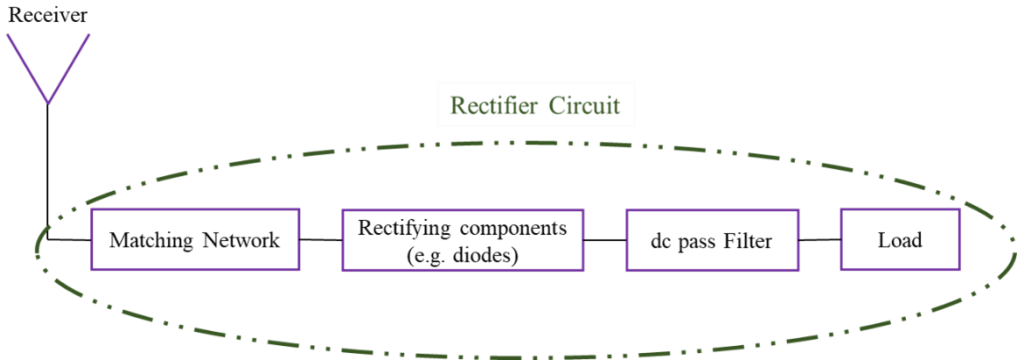

Figure 3.1 A simple rectifier for RF energy harvesting applications.

Impedance matching for rectifiers is crucial to maximize power transfer from an antenna or a metasurface harvester and so improve the overall efficiency of RF energy harvesting systems. To achieve impedance matching, several techniques may be employed, including reactive matching, transmission line matching, or a combination of both [116]. Reactive matching utilizes capacitors and inductors to adjust impedance. Depending on the application, different network configurations can be considered as show in Figure 3.2.

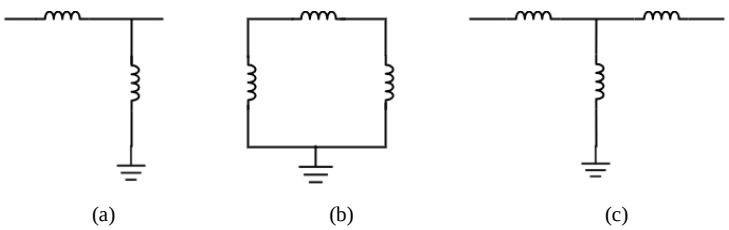

Figure 3.2 Some common configurations for matching networks (a) L- network, (b) π-network, and (c) T-network.

Transmission line matching involves the use of microstrip lines or stubs, such as radial stubs, short-circuit stubs, and open-circuit stubs, to adjust impedance. A combination of reactive matching and transmission line matching can be employed to leverage the benefits of both techniques. In particular, reactive components may help to fine-tune the matching behavior of microstrip lines, especially for fabricated designs.

As shown in Figure 3.1, a diode can be used as a rectifying component in RF energy harvesting. An ideal diode is a component that exhibits perfect switching behavior. Considering an ideal conversion of AC to DC using a single ideal diode, during the positive half-cycle of the AC input across the diode, the latter behaves like a closed circuit (with zero resistance), and the current flows through the diode without a voltage drop. During the negative half-cycle of the AC input, the diode behaves like an open circuit (with infinite resistance), which prevents current from passing through it.

Real-world diodes are not ideal, rather, they approximate the behavior described in the paragraph above as non-linear electronic components. Current passing through a non-ideal diode can be calculated by the equation below [117]:

$$I_d = I_s \left(e^{\frac{V_d}{nV_t}} - 1\right) \tag{3.1}$$

where I_s denotes the reverse-bias saturation current, V_d is the voltage across the diode (also called forward voltage), V_t represents the thermal voltage, and n denotes the ideality factor of the diode.

Understanding this non-linear behavior is key to selecting specialized diodes, such as Schottky diodes, which are well suited for energy harvesting applications for the following reasons. First, they have a low threshold voltage [118]. Having a low threshold voltage is particularly important for energy harvesting applications. Besides a low threshold voltage, other positive features of Schottky diodes are the lower junction capacitance, which reduces their response time, and the lower forward voltage drop, which helps to reduce losses and have a more efficient device [119].

A standard Schottky diode model includes parasitic elements that represent the physical characteristics of the diode and its packaging; Figure 3.3 shows an example of these elements. R_j and C_j are the junction resistance and junction capacitance, respectively. They are nonlinear components, as they both vary with the input power. R_S is the series resistance, while C_P and

L_s are the parasitic capacitance and inductance, respectively. The values of these parameters associated with different types of diodes are provided as an example in Table 3.1.

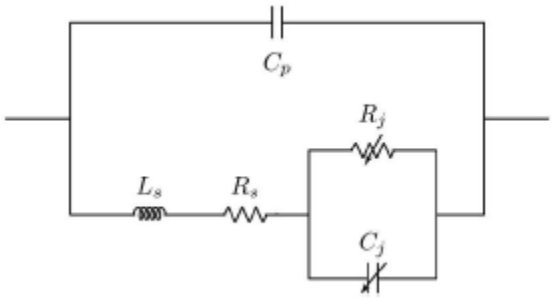

Figure 3.3 Diode equivalent circuit with the inclusion of parasitic components [120].

Table 3.1 Some common Schottky diode models and their key parameters [120-122].

Parameter	Description	SMS 7630	HSMS 2820	HSMS 2860
I_s (A)	Reverse-bias Saturation Current	5	0.022	0.05
R_s (Ω)	Series resistance	20	6	6
C_{j0} (pF)	Zero voltage capacitance	0.14	0.7	0.18
V_j (V)	Junction voltage	0.34	0.65	0.65
C_p (pF)	Parasitic capacitance	0.16	0.08	0.08
L_s (nH)	Parasitic inductance	0.8	2	2
Bv (V)	Breakdown voltage	2	15	7
n	Ideality factor	1.05	1.08	1.08
V_{th} (V)	Threshold voltage	0.09	0.15	0.25

As shown in Figure 3.1, after the diode, a dc pass filter (typically a low-pass filter) is used to block high order harmonics originating from the nonlinear behavior of the diode. This allows only the DC to reach the load or storage device, which ensures consistent and reliable power delivery that many devices rely on.

The load resistor positioned at the output of the rectifier plays an essential role in RF energy harvesters: it either directly consumes the harvested DC power - supplying low power devices like IoT sensors or microcontrollers - or it stores the power in a component such as a capacitor or battery for later use. It is important to highlight that the load also impacts the total input impedance of the rectifier circuit, thereby influencing the efficiency and overall performance of the matching network.

The rectification efficiency of a rectifier can be calculated by Equation (3.2).

$$\eta_{Rec} = (P_{DC}/P_r)\times 100 \tag{3.2}$$

where P_r is the input power of the rectifier circuit, and P_{DC} is its DC output power obtained as:

$$P_{DC} = \frac{V_{DC}{}^2}{R} \tag{3.3}$$

where V_{DC} is the output voltage across the load resistor (R) of the rectifier.

Several different topologies can be used for rectifying the AC/RF input [22], the most common rectifier topologies can be categorized into two general groups: single-diode configurations and multiple-diodes configurations. Single-diode configurations are used in RF energy harvesters due to their simplicity and higher efficiency at low input power levels. Two main types are the series diode rectifier [22] and the shunt diode rectifier [123]. In the series diode configuration, the diode is placed in series with the load, enabling the positive half-cycle of the AC input to flow and blocking the negative half, as shown in Figure 3.4.

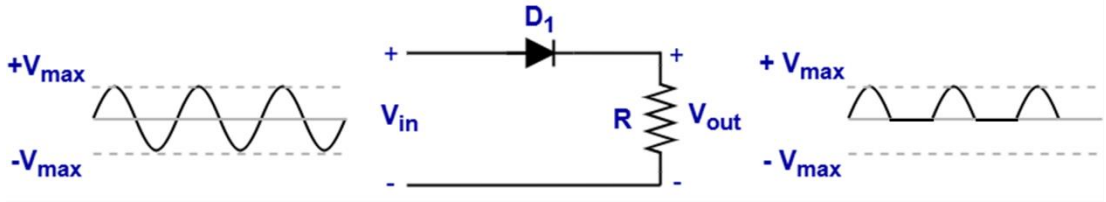

Figure 3.4 A simple rectifier in series-diode configuration.

On the other hand, the shunt diode configuration, illustrated in Figure 3.5, places the diode in parallel with the load. It works by blocking the positive half-cycle while allowing the negative half-cycle to pass through to the load.

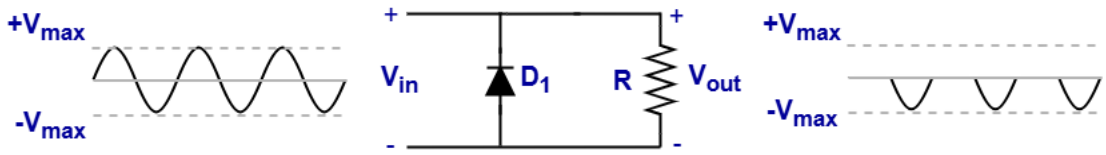

Figure 3.5 A simple rectifier in shunt-diode configuration.

The main advantage of these two topologies is their minimal component count and, as a result, reduced losses, making them more efficient for low ambient RF power. However, a single diode allows one half of the AC cycle to reach the load.

Multiple-diode configurations, such as the voltage doubler rectifier and bridge rectifier, capture both halves of the AC input [22]. The voltage doubler topology, depicted in Figure 3.6, uses two diodes and two capacitors to rectify both the positive and negative half-cycles, combining their voltages to produce an output that is approximately twice the peak input voltage. However, the added components introduce more losses, making this configuration less efficient at very low input power levels compared to single-diode.

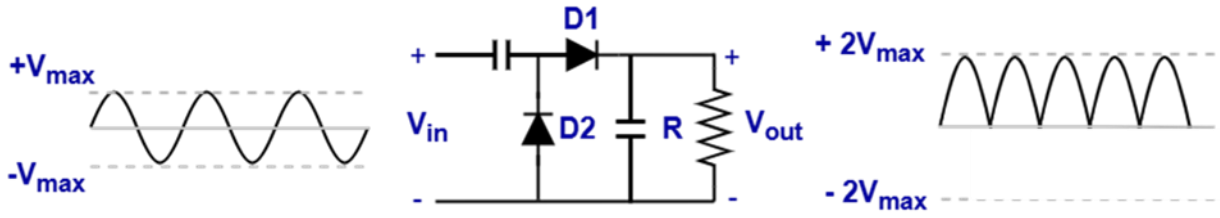

Figure 3.6 A simple voltage doubler configuration.

The bridge rectifier, shown in Figure 3.7, incorporating four diodes connected in a bridge arrangement, fully utilizes both halves of the AC input. Despite this, the bridge design suffers from higher losses since two diodes conduct during each half-cycle.

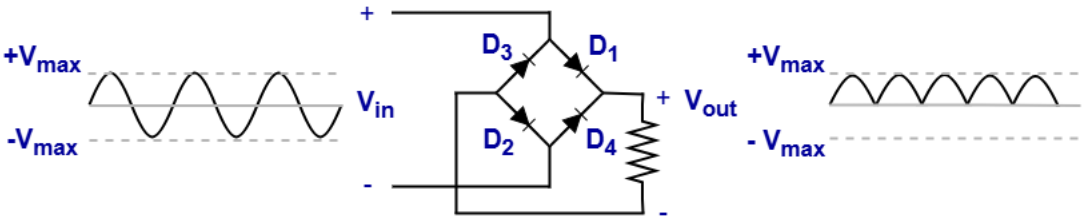

Figure 3.7 A simple bridge configuration.

Boaventura et al in [117] discussed the impact of number of diodes in a simple circuit on the rectification efficiency as shown in Figure 3.8. It can be seen the single diode configuration has a higher efficiency at lower input power levels.

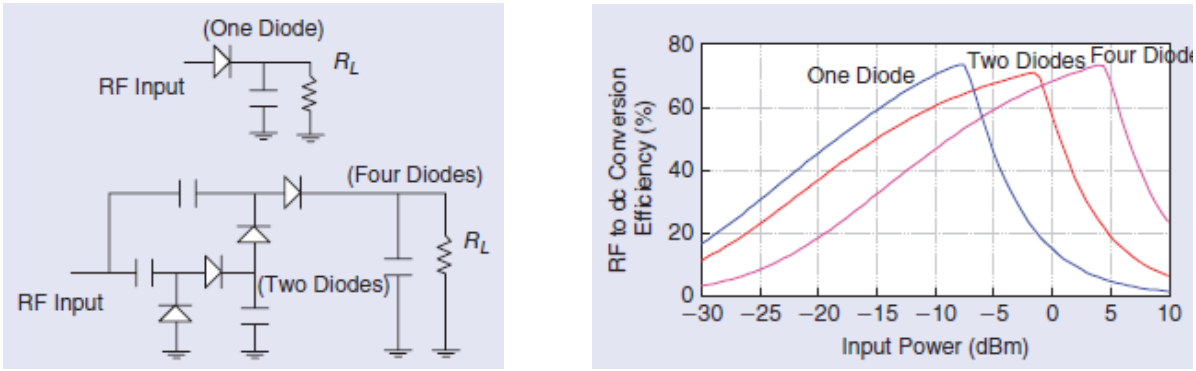

(a) (b)

Figure 3.8 (a) Configurations with different numbers of diodes and (b) impact of the number of diodes on the rectification efficiency [117].

The choice of topology depends on factors such as the available input power, and operating frequency. Since the output of our proposed metasurface harvester in Chapter II is differential, we require a rectifier topology that corresponds to this configuration. Rather than a single input, note that the differential rectifier observes two inputs of equal amplitude, shifted by 180 degrees [124-130]. The idea behind a differential rectifier is to have both inputs contributing to a common DC output; this idea can be implemented in different ways, using rectifier circuits with multiple diodes [124] (such as based on the voltage doubler [128, 129]) or only a single diode [130]. Keeping in mind our goal of a compact overall topology, we selected the rectifier topology of [130] for our work. In the next section the design and performance of the proposed differential rectifier will be discussed.

3.3 Proposed Differential Rectifier

Our proposed rectifier is designed such as to accommodate a differential input comprising two RF signals of equal magnitude but with a 180-degree phase shift. This input corresponds to the output at the end of the microstrip lines of our metasurface absorber as described in Section 2.2 of Chapter II. While in Chapter II the harvested RF energy was directed to a resistive load, here it is directed to a rectifier that will convert the collected RF to DC. Note that since we have optimized the load resistance for maximum absorption in Chapter 2, the input impedance of our proposed rectifier equals that of the load in Chapter 2 (115 Ω). Furthermore, we design our rectifier to operate at 2.49 GHz, which corresponds to the measured operating frequency of the single-band metasurface harvester.

The rectifier depicted in Figure 3.9 receives two inputs (P_s) that are 180 degrees out of phase. Due to the diode's orientation, the negative half-cycle of the top source passes through the diode, as does the positive half-cycle of the bottom source. As a result, the output comprises both the positive and negative cycles in a rectified waveform. Observe that the single-diode configuration is chosen to reduce component usage and to limit associated losses.

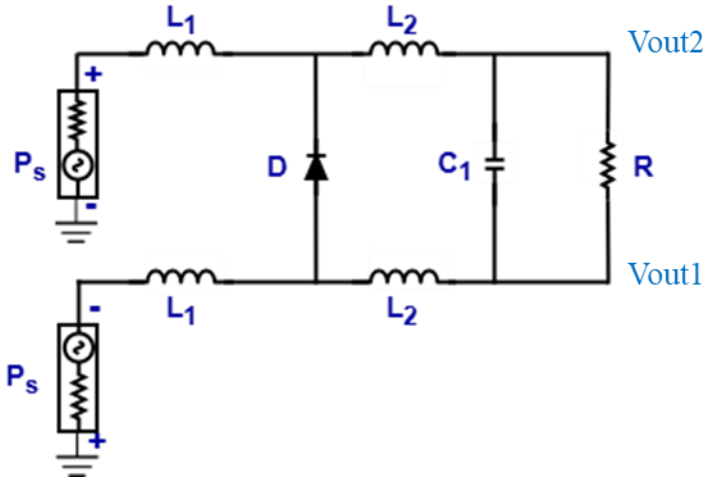

Figure 3.9 Simplified schematic of our proposed differential rectifier.

In this topology, the output voltage across the load resistor (R) of the rectifier, denoted as $V_{DC-diff}$ can be obtained from [124]:

$$V_{DC-diff} = Vout2 - Vout1 \tag{3.4}$$

A SMS7630 Schottky diode is used in the rectifier circuit, which is chosen for its low threshold voltage that is particularly suited for a low-power environment. The parasitic package effects of the diode are included in the circuit whose complete values are given in Table 3.1. The harmonic balance (HB) simulation is performed in ADS to evaluate the rectifier's performance. The operating frequency is 2.49 GHz, and the total input power level of the rectifier (P_r) is -2.7 dBm, corresponding to the single input power of P_s= -5.7 dBm at the rectifier. While previous works [79, 87, 91, 94, 96, 97] designed their circuits at relatively high input power levels, the proposed rectifier is designed and optimized for a noticeably lower power range, which is closer to real life scenarios.

Besides the main components of the rectifier, the circuit depicted in Figure 3.10 consists of 3 other sections that each serve a different purpose: the matching network, the DC filter, and the load. As already discussed, the matching network guarantees that the input impedance of the rectifier matches the output impedance of the metasurface harvester, thus maximizing the amount of transferred power. The matching network was designed and optimized to minimize the number of lumped elements components. C_3 in Figure 3.10 acts as a DC block, with its value provided in Table 3.2. The role of the DC filter at the end of the circuit is to remove undesired harmonics introduced by the nonlinear diode of the rectifier, that is, it acts as a DC pass filter. The parameter values are provided in Table 3.2, Table 3.3 and Table 3.4.

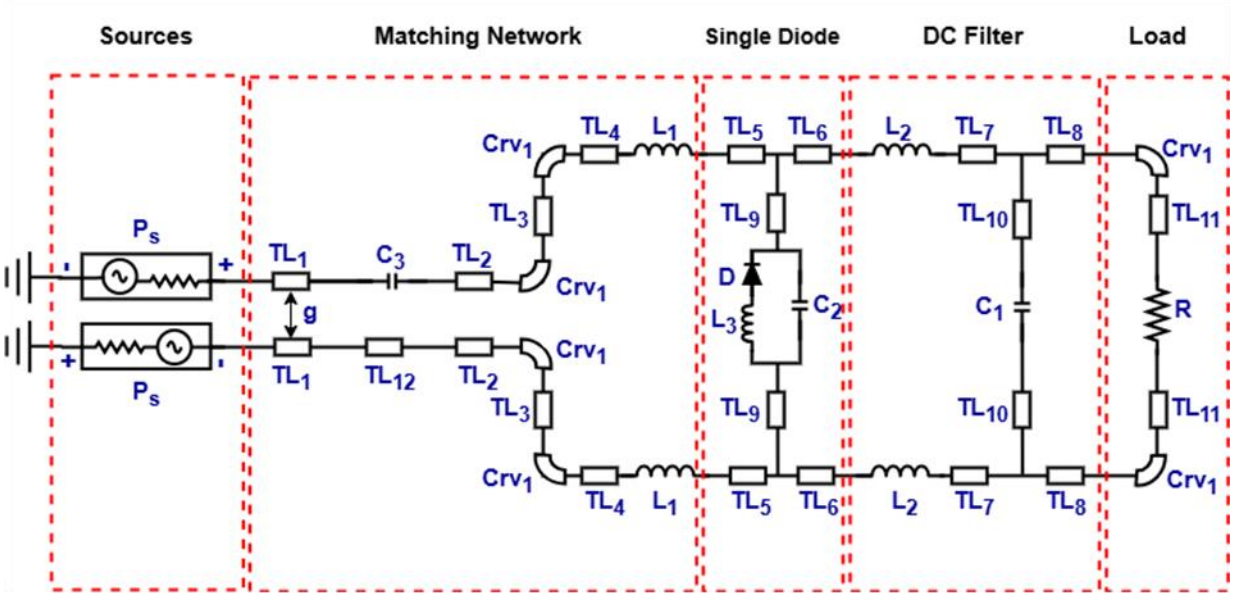

Figure 3.10 The proposed differential rectifier circuit with indicated sections.

Table 3.2 Parameters of the proposed differential rectifier.

Parameter	Values	Unit
C_1	100	pF
C_2	0.25	pF
C_3	100	pF
L_1	5.6	nH
L_2	3.3	nH
L_3	0.6	nH
R	2000	Ω

Table 3.3 Physical parameters of the proposed differential rectifier.

Parameter	Length/ width (mm)	Parameter	Length/ width (mm)
TL_1	11.06/1.26	TL_8	3/1.26
TL_2	2/1.26	TL_9	2.72/1
TL_3	0.1/1.26	TL_{10}	3.02/2
TL_4	1.2/1.26	TL_{11}	2/1.26
TL_5	1.6/1.26	TL_{12}	0.5/1.26
TL_6	2/1.26	TL_{13}	0.58/1.26
TL_7	4.3/1.26	TL_{14}	0.25/2

Table 3.4 Parameters of the curves in the proposed differential rectifier.

Parameter	Radius (mm)	Width (mm)
Crv1	1.5	1.26
Crv2	1.27	1.26
Crv3	2.05	2

To ensure accurate simulation results, models of real components are used: the inductors are from Coilcraft, the capacitors from Murata, and the resistor is an SMD with the value of 2 kΩ. The rectifier is designed on the same substrate as the metasurface harvester, namely Arlon DiClad 880, with permittivity of 2.17, a loss tangent of 0.0009 and a thickness of 2.36 mm.

The proposed rectifier circuit is simulated additionally in co-simulation Momentum, (see Figure 3.11) to allow for more realistic simulation results. Given the detailed physical description of our circuit, an electromagnetic (EM) simulation is performed in Momentum to evaluate its performance.

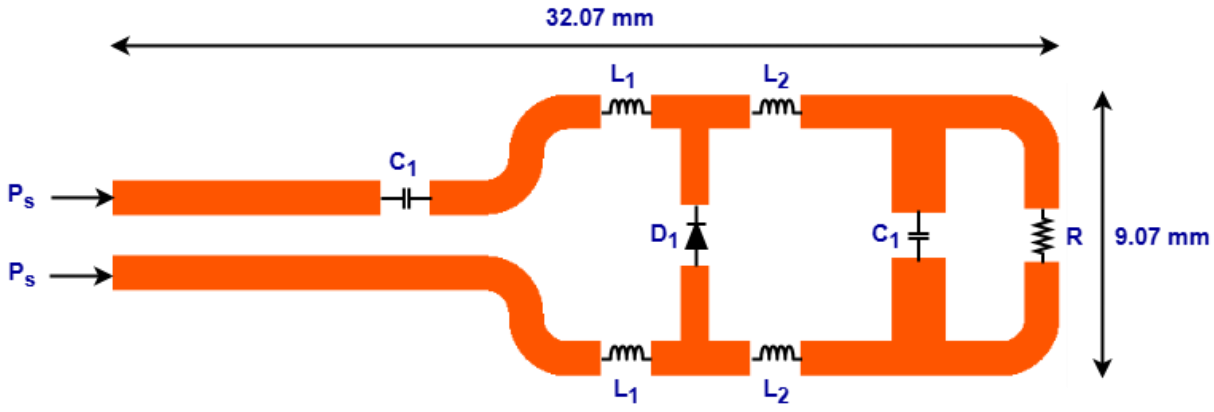

Figure 3.11 Momentum layout of our proposed differential rectifier.

The rectification efficiency is calculated using Equation (3.2), where the input power 2×Ps is considered for both differential ports. The simulated rectification efficiency results are plotted in Figure 3.12 (a), showing that at -2.7 dBm total input power, the rectifier achieves an efficiency of 58% at 2.49 GHz. Furthermore, Figure 3.12 (b) presents the rectification efficiency as a function of the frequency at -2.7 dBm total input power, confirming that the maximum efficiency of 58% does indeed occur at 2.49 GHz.

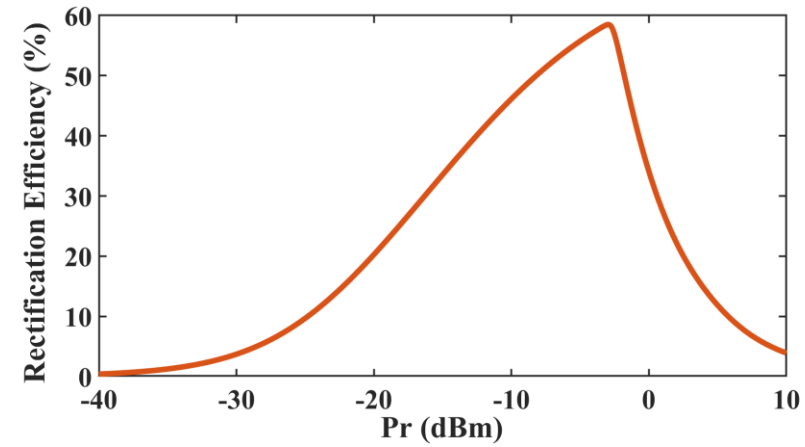

(a)

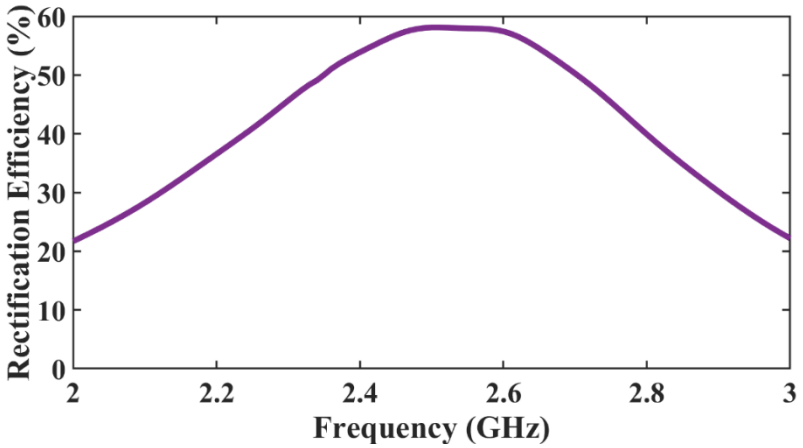

(b)

Figure 3.12 Simulated rectification efficiency vs. (a) total input power at 2.49 GHz and (b) frequency for a total input power of -2.7 dBm.

Just as for the metasurface, we intended to measure the rectifier alone but soon ran into the limitations of standard measurement instruments, as the gap "g" between the two sources (0.35 mm) was too small to accommodate typical SMA connectors. To overcome this issue, an optimized extension was added to the rectifier circuit to ensure its compatibility with the measurement equipment. Additionally, the input impedance of the rectifier was adjusted to match a 50 Ω standard SMA connectors. Importantly, the extension was designed to ensure that it does not affect the operating frequency, although it does result in a slight reduction in rectification efficiency.

The rectifier layout with the tuned extension is illustrated in Figure 3.13 (s= 8.25 mm), and the corresponding parameter values are summarized in Table 3.2, Table 3.3 and Table 3.4. The rectification efficiency of the modified rectifier circuit is plotted in Figure 3.14, revealing a 4.3% decrease at 2.49 GHz, which can be attributed to mismatches introduced by the modifications.

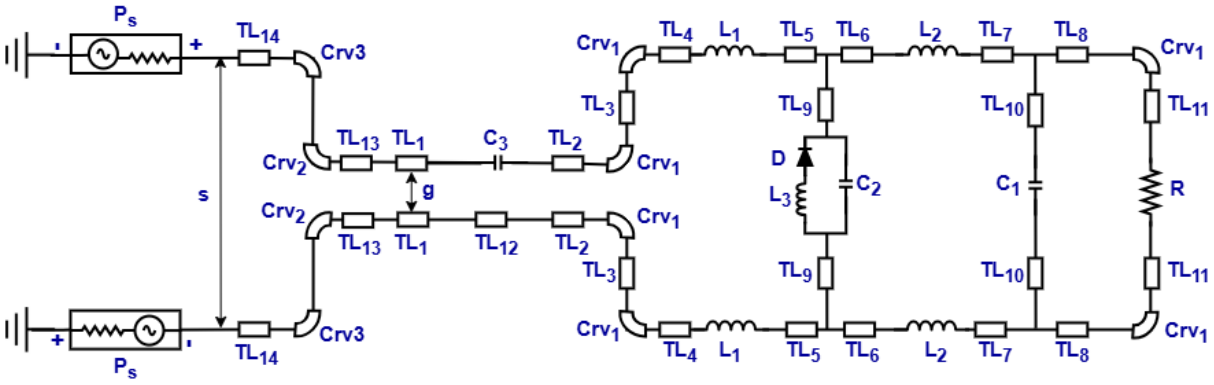

(a)

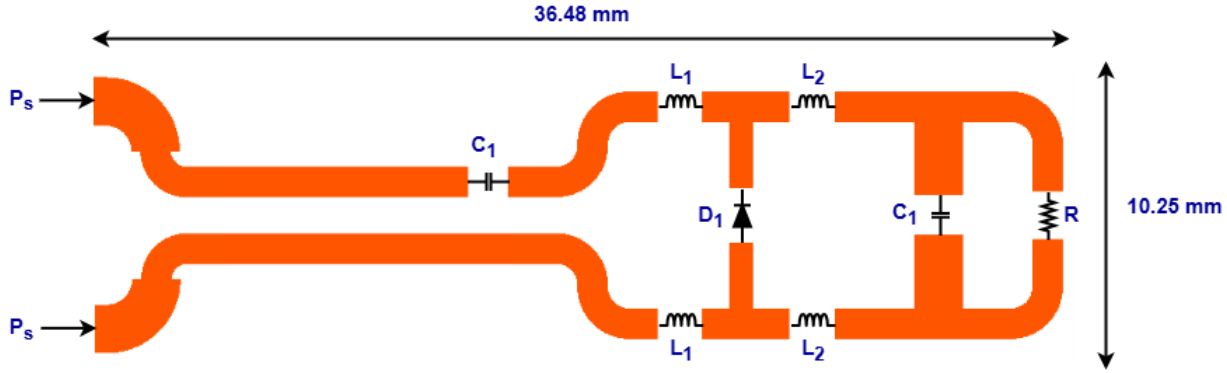

(b)

Figure 3.13 (a) the modified proposed differential rectifier circuit and (b) the corresponding Momentum layout.

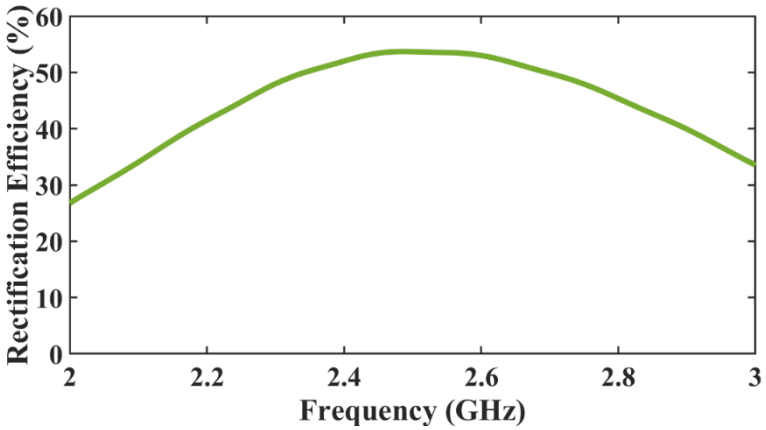

Figure 3.14 Simulated rectification efficiency of the modified rectifier varying with frequency for an input power level of -2.7 dBm.

A similar trend is observed in the rectification efficiency vs. input power of the rectifier. As shown in Figure 3.15, at -2.7 dBm total input power of the rectifier, the rectification efficiency remains at 53.7%.

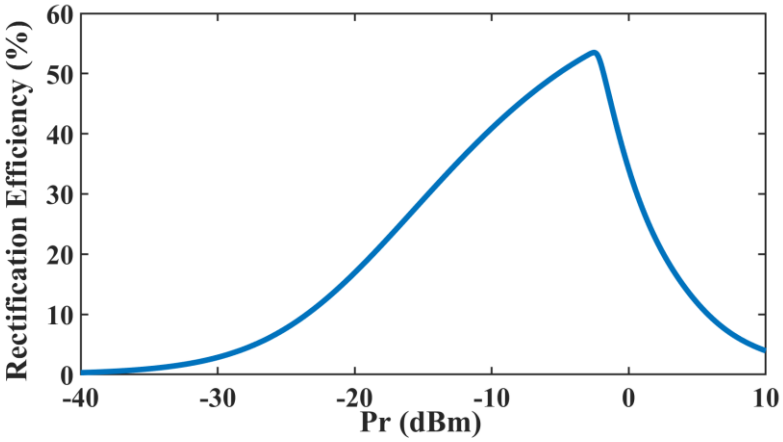

Figure 3.15 Simulated rectification efficiency of the modified rectifier varying with total input power (P_r).

The modifications caused a drop of around 4% in the rectification efficiency, indicating minor losses introduced by the extension. Despite this reduction, the extension remains a necessary adjustment for measurement purpose and can be removed if required without affecting noticeably on the performance of the original rectifier circuit. After incorporating the necessary modifications in the proposed rectifier circuit, in the next section, the measurement of the fabricated rectifier is discussed and a comparison to some existing works on metasurface harvesters that include a rectifier circuit is presented.

3.4 Realization and Measurement of the Proposed Rectifier

The modified differential rectifier is fabricated on a 4.6×3.1 mm^2 Arlon Diclad 880 substrate with a thickness of 2.36 mm, as illustrated in Figure 3.16.

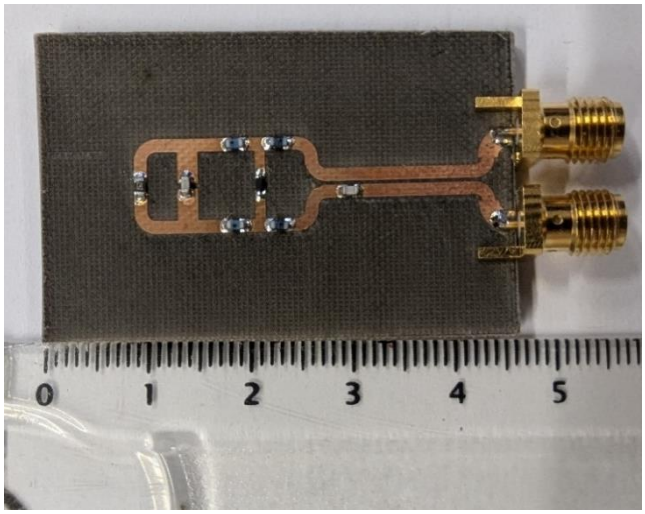

Figure 3.16 Fabricated differential rectifier with modifications.

While a differential rectifier requires two inputs (of equal magnitude and with a 180° phase shift), most RF measurement equipment—such as network analyzers and signal generators—only provide a single output. We therefore employed the BAL-0026 balun [123] (operating from 300 kHz to 26.5 GHz) to ensure that the input power is evenly divided into two signals with equal amplitude but opposite phase, thus enabling differential operation.

The input of the balun is connected to the 50 Ω RF output of the signal generator via an SMA connector, while each of the two outputs of the balun is connected to one of the inputs of the differential rectifier, as shown in Figure 3.17. The signal generator supplies power at a level that results in -2.7 dBm at the total input of the rectifier at 2.49 GHz.

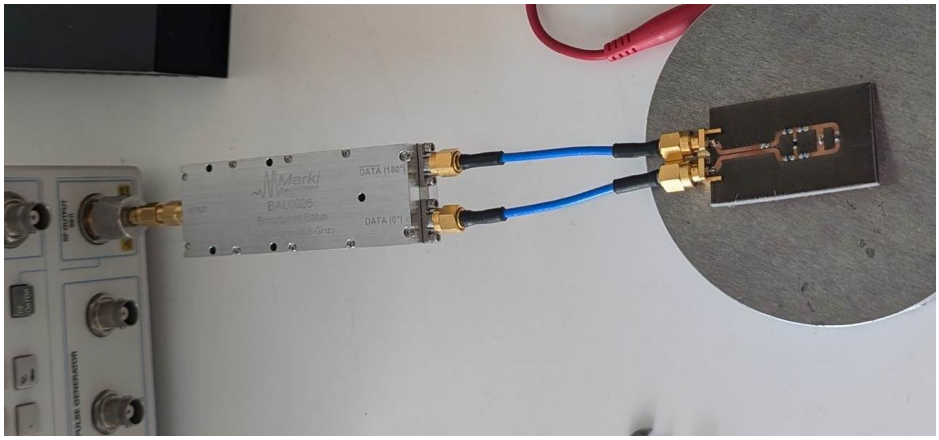

Figure 3.17 Connection of the fabricated prototype with the balun.

The DC output voltage (V_{DC}) of the proposed rectifier is measured using a digital multimeter (Velleman, DVM345DI). The corresponding DC output power (P_{DC}) is calculated using Equation (3.3), while the rectification efficiency is determined using Equation (3.2). Here P_{in} is the total input power at the rectifier's input from both ports, with each port receiving an input power of P_s. A comparison of the simulated and measured rectification efficiency vs. frequency at -2.7 dBm total input power is shown in Figure 3.18 (a). The peak of the measured rectification efficiency occurs at 2.45 GHz, with the value of 46.4%, which, in turn, leads us to measure the rectification efficiency vs. power being at this frequency, as shown in Figure 3.18 (b). This plot also presents the simulated rectification efficiency vs. total input power at 2.45 GHz for comparison.

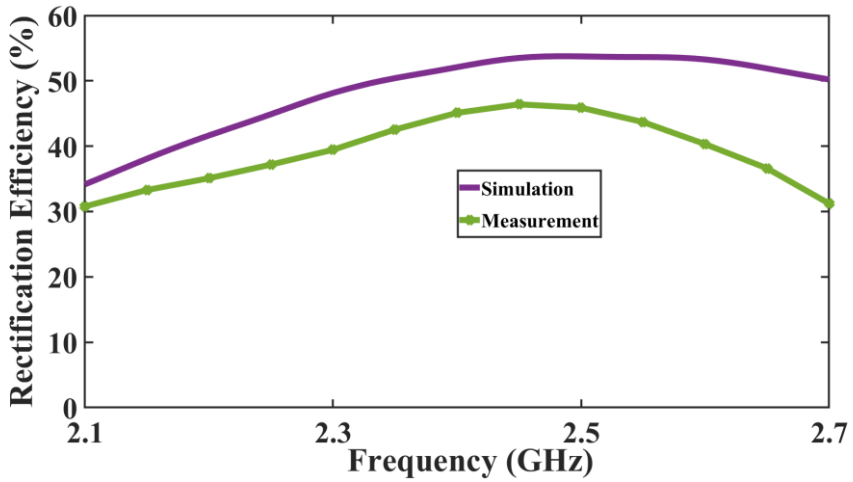

(a)

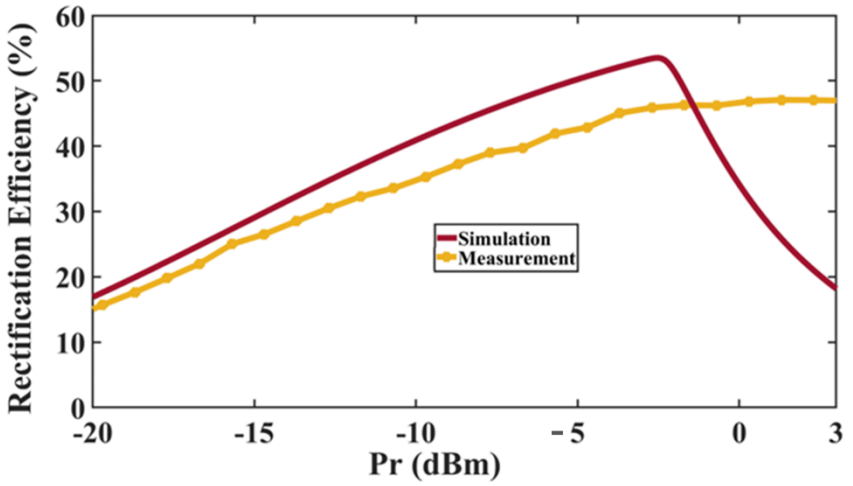

(b)

Figure 3.18 Comparison between the measured and simulated rectification efficiency varying with (a) frequency for a power level of -2.7 dBm and (b) P_r at 2.45 GHz.

There is good agreement between the simulated and measured rectification efficiencies up to -1.5 dBm. Beyond this power level, the simulated rectification efficiency begins to drop, the simulated rectification efficiency begins to drop, while the measured efficiency does not follow the same trend. This is due to the actual breakdown voltage in the SMS7630 SPICE model being higher than the 2 V specified in the official datasheet [124].

However, a few differences that are observed can be attributed to factors such as the imperfection of the measurement equipment and balun. Another contributing factor is the accuracy of the diode model used in the simulation. Since not all parasitic package parameters are provided in the datasheet, some values were obtained from [120]; this approximation may introduce slight deviations between the actual parasitic effects and the modeled values.

After evaluating the proposed rectifier individually, the fabricated rectifier is used to convert the collected RF power of the proposed single-band metasurface (Chapter II) to DC output, which will be discussed in the next section.

3.5 Measurement of the Proposed Metasurface Harvester Connected with the Rectifier

As discussed in the introduction, the rectifier circuit serves as the second stage of the complete RF metasurface energy harvester (hereafter also called the whole device), with the metasurface harvester being the first stage.

For the whole device measurement, the proposed modified single-band metasurface harvester, presented and analyzed in Chapter II, is used again to collect RF power, while the proposed rectifier is used to convert the captured RF input into a DC output. The integration of the metasurface and rectifier enables the full evaluation of the RF to DC conversion performance.

Figure 3.19 illustrates how the RF outputs of the middle row of the modified metasurface are connected to the inputs of the rectifier via two cables. Recall that each of the remaining rows of the single-band metasurface is terminated with a 120-ohm SMD resistor.

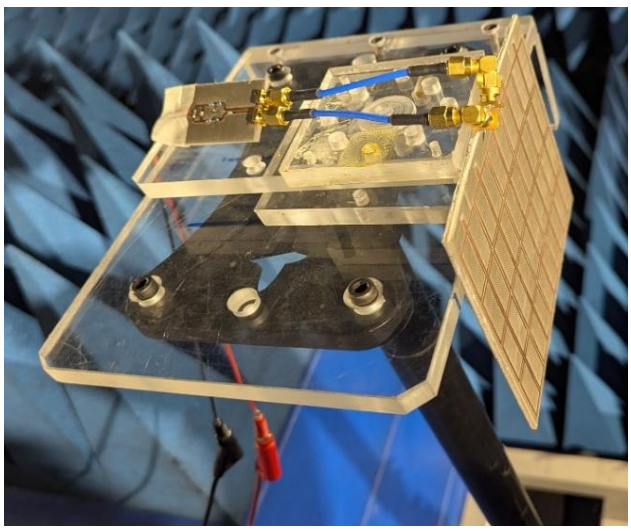

Figure 3.19 Connection of the fabricated metasurface harvester and the rectifier.

The measurement setup of the whole device, illustrated in Figure 3.20, is performed in an anechoic chamber where the metasurface is positioned in the far field of the horn to ensure that the incident wave may be considered a plane wave. The same horn antenna used in the

single-band metasurface measurement (Chapter II) is employed, with a gain of 6.4 dBi at 2.5 GHz. The distance between the horn and the metasurface prototype is 1.07 meters. To achieve a power of -2.7 dBm at the input of the rectifier (P_r) at 2.5 GHz, an amplifier is used to boost the output power of the horn.

Figure 3.20 Measurement setup of the whole device in the anechoic chamber.

The DC output voltage is measured using a Velleman DVM345DI digital multimeter. The total measured RF to DC efficiency (total efficiency) of the whole device is calculated according to the equation below:

$$\eta_t = P_{DC}/P_{in} \tag{3.5}$$

where P_{DC} is the output DC power of the rectifier (obtained according to Equation (3.2)) and P_{in} is the incident power on the metasurface harvester, which can be calculated according to Equation (2.7). The effective area of the metasurface is 0.00298 m². The total measured efficiency versus frequency is obtained when the total input power (P_r) is at -2.7 dBm at 2.5 GHz, as shown in Figure 3.21. The peak of the total efficiency occurs at 2.51 GHz with the value of around 20%. Note that the 0.2 dB loss per cable (two cables total) between the metasurface and the rectifier was not considered in the calculation of the total efficiency. Including these cable losses would result in a slightly higher total efficiency value.

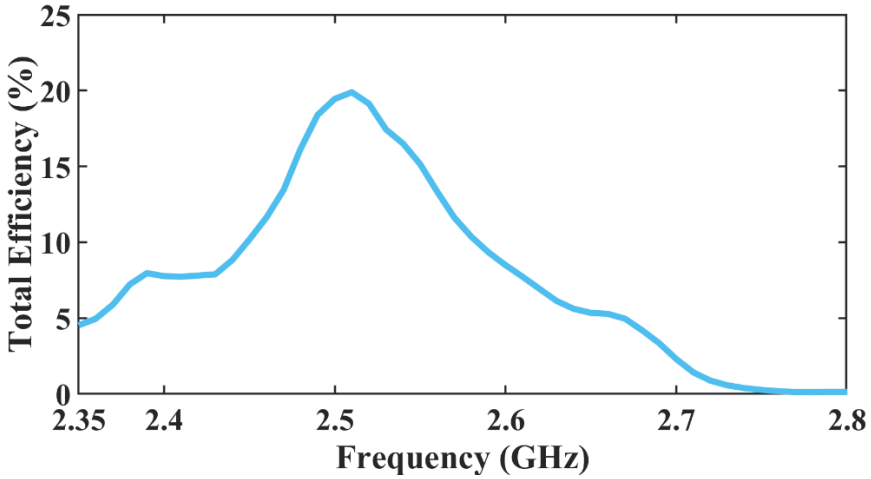

Figure 3.21 Measured total efficiency vs. frequency for a power of -2.7 dBm.

As seen in Figure 3.21 the peak of the total measured efficiency occurs at 2.51 GHz, as a result the measured total efficiency vs. P_r is shown in Figure 3.22 at this frequency.

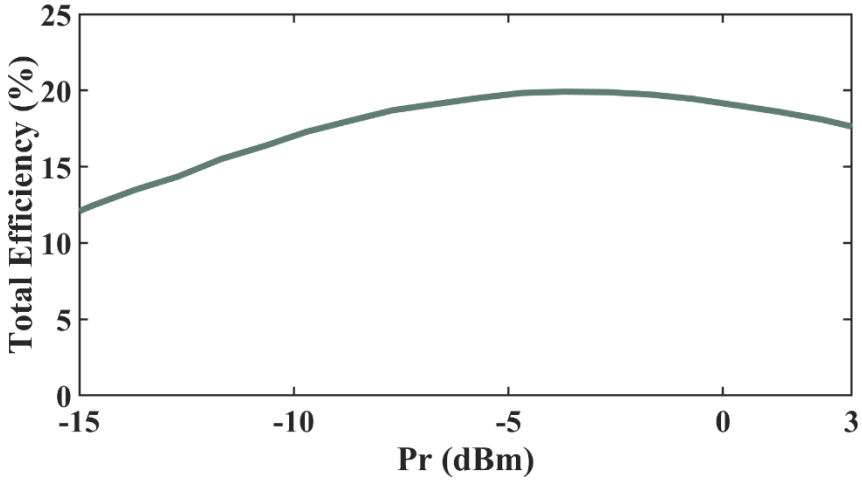

Figure 3.22 Measured total efficiency vs. Pr at 2.51 GHz.

It is important to note that this measurement was conducted with the extensions included for both the modified metasurface and rectifier. This approach allowed for a quick evaluation of the entire device's performance, as both components had already been fabricated and measured individually. However, we acknowledge that removing the extensions and fine-tuning the metasurface's operating frequency to 2.45 GHz would expected to noticeably enhance the total efficiency.

Table 3.5 provides a summary of the performance of some existing works on metasurface RF energy harvesters that incorporate a rectifier. The table relies on the following abbreviations:

Abbreviation	**Description**
Ref	References
Freq	Frequency
No. Rect	Number of used rectifiers
Sim η_{MS-s}/η_{MS-AV} /η_{MS-w}	Simulated capturing efficiency of the supercell/average row/whole finite array
Sim η_{Rec}	Simulated rectification efficiency
Meas Total η_{t-SP} /η_{t-MR}/η_{t-W}	Measured total efficiency of the supercell/middle row/whole finite array

Table 3.5 Performance comparison of some reported RF metasurface harvesters with the integrated rectifiers.

Ref	**Freq (GHz)**	**No. Rect**	**Cell size (array)**	**Sim η_{MS-AV}/η_{MS-w} (%)**	**Sim η_{Rec} (%)**	**Meas Total η_{t-SP}/η_{t-MR}**
[87]	2.4	18 (in array)	$0.56\lambda_0 \times 0.56\lambda_0$ (12×12)	η_{MS-w} with feed network 92% at 2.4 GHz	~ 80% at around 9 dBm at 2.1 GHz	η_{t-SP} 70% at around 9 dBm at 2.1 GHz
[79]	2.45	36 (in array)	$0.163\lambda_0 \times 0.163\lambda_0$ (6×6)	-	72.9% at 5 mW/cm^2 at 2.45 GHz	η_{t-w} 66.9% at 5 mW/cm^2 at 2.45 GHz
[94]	2.4	2 Rect. per supercell (N=7)	$0.168\lambda_0 \times 0.168\lambda_0$ (7×7)	-	67.1% at 3 dBm at 2.2 GHz	η_{t-MR} 64% at 3 dBm at 2.2 GHz
	12.6	2 Rect. per supercell (N=7)	$0.882\lambda_0 \times 0.882\lambda_0$ (7×7)		60.4% at 14 dBm at 12.3 GHz	η_{t-MR} 55% at 14 dBm at 12.3 GHz
[91]	2.45	1 Rect. per supercell (N=6)	$0.285\lambda_0 \times 0.469\lambda_0$ (6×5)	η_{MS-s} 79% at N/A	-	η_{t-MR} 61% at 15 dBm at 2.2 GHz

Ref	Freq (GHz)	No. Rect	Cell size (array)	Sim η_{MS-AV}/η_{MS-w} (%)	Sim η_{Rec} (%)	Meas Total η_{t-SP}/η_{t-MR}
[96]	1.85	1 Rect. per supercell (N=4)	$0.21\lambda_0 \times 0.271\lambda_0$ (2-connected array 4×5)	η_{MS-s} 80% at 1.8 GHz	79% at 15 dBm at 1.85GHz	η_{t-MR} 43% at 15 dBm at 1.8 GHz
	2.5		$0.283\lambda_0 \times 0.367\lambda_0$ (2-connected array 4×5)	η_{MS-s} 37% at 2.3 GHz	78% at 15 dBm at 2.45GHz	η_{t-MR} 31% at 15 dBm at 2.3 GHz
[97]	5.2	12 Rect. (4 capacitors per cell) (in array)	$0.59\lambda_0 \times 0.59\lambda_0$ (6×6)	-	-	-
This work	2.45	1 Rect. per supercell (N=4)	$0.22\lambda_0 \times 0.22\lambda_0$ (5×4)	η_{MS-AV} 90% at 2.54 GHz (without modification)	58% at 2.49GHz (without modification)	-
				η_{MS-AV} 73% at 2.54 GHz (with modification)	53.7% at 2.49GHz (with modification)	η_{t-MR} ~20% at -2.7 dBm at 2.51 GHz

The simulated data of the rectification efficiency is included in the Table 3.5 as the measurement of the rectifier standalone was not presented in [79, 87, 91, 94, 96, 97]. As mentioned in Chapter II, the proposed single-band metasurface has the advantages of being compact and single-layer, while a single rectifier per supercell is used to convert the collected RF power to DC. Despite the extensions and modifications, the whole device demonstrated good performance at low input power levels in comparison to many existing works on metasurface RF harvesters [79, 87, 91, 94, 96, 97]. This demonstrates its promising potential for RF energy harvesting applications such as for IoT devices.

3.6 Conclusion

The aim of this chapter was to propose a compact differential rectifier operating efficiently at low input power levels, and to demonstrate the feasibility of employing the

proposed rectifier in combination with our proposed metasurface to obtain an efficient RF to DC energy harvester.

Among the commonly employed rectifier topologies, we opt for a single-diode configuration so as to obtain a structure as compact as possible. Moreover, owing to the differential output of the metasurface harvester – which is rectifier's input – we opt for a differential rectifier. The schematic of the rectifier circuit includes the three sections; the matching network (that maximizes the transferred power from the metasurface harvester); the diode (the heart of the rectifier, which is chosen to be a SMS7630 Schottky diode due to its low threshold voltage, which is advantageous for low input powers); and a DC filter (which removes higher harmonics originating from the diode's nonlinearities).

In addition to the circuit schematic, the physical dimensions of all elements and the parasitic components are incorporated in a Momentum simulation. The simulation investigates the rectification efficiency vs. the input power level as well as the rectification efficiency vs. the frequency; an efficiency of 58% at an input power level of -2.7 dBm and at frequency of 2.49 GHz (so as to match the highest capturing efficiency of the metasurface harvester designed in Chapter II).

An important limitation that we had to consider when designing the rectifier was the incorporation of an extension, necessary to facilitate the measurement of the fabricated structure. Similarly to the extension required for the measurement of the metasurface harvester (see again Chapter II), the extension for the rectifier was necessitated by the small gap between the inputs that was incompatible with standard measurement instruments. The extensions incur no substantial changes to designed rectifier performance.

The rectifier was fabricated on an Arlon Diclad 880 substrate. To facilitate a differential input, a BAL-0026 balun was employed that split the input provided by the signal generator into two equal-amplitude, opposite-phase inputs. The measurement conditions match those of the simulation, namely a total input power level of -2.7 dBm and a frequency of 2.49 GHz. A good agreement is observed between measurement and simulation.

Finally, the entire structure with the rectifier connected to the metasurface harvester was measured. The same horn antenna used in the single-band metasurface measurement is employed along with an amplifier to achieve a total input power of -2.7 dBm at the rectifier. The total efficiency of around 20% is achieved at 2.51 GHz.

In light of the above results, we may conclude this chapter by noticing that the rectifier and metasurface harvester may be designed and optimized separately and later combined into a single, efficient structure.

Note that the whole device without inclusion of any extensions in both metasurface and rectifier designs, would have enhanced the total efficiency.

4 An Efficient Compact Dual-Band Metasurface Energy Harvester

4.1 Introduction

Metasurface RF energy harvesters offer various solutions for capturing ambient electromagnetic energy, as introduced in the State of the Art and further discussed in later chapters. Single-band designs collect power at a specific resonance frequency, while multi-band designs provide an advantage by harvesting energy from multiple frequency bands [14, 54].

Several studies have explored multi-band RF energy harvesting designs [44, 75, 94-96]. However, a crucial challenge is to develop a compact multi-band harvester that collects RF power across multiple frequency bands using the fewest possible lumped elements/rectifiers. Moreover, can this be achieved while improving capturing efficiency?

The interconnected cells method, by virtue of collecting RF power from multiple cells and transferring it to a single rectifier positioned at the same layer of the metasurface, has the important advantage of eliminating multilayer challenges. However, due to low ambient RF energy, we proposed in Chapter II the reoptimization of the resistive load value of the design as an intermediary stage to increase the capturing efficiency of the structure.

Building on the foundation that we introduced for a single-band structure, in this chapter we broaden our ambitions to collect RF energy at two desired frequencies with a single device. To do so, we introduce an efficient single-layer dual-band metasurface energy harvester operating at the Wi-Fi bands 2.45 GHz and 5.2 GHz (IEEE 802.11ax/be). A dual-band harvester can enable us to collect power at two distinct frequencies and so increase the total amount of power collected. Additionally, the proposed intermediate step in the design process is applied to the proposed dual-band metasurface harvester to improve its capturing efficiency.

In this chapter, first, the geometry of the proposed dual-band unit cell is presented and its performance is evaluated, including a parameter study, to ensure optimized behavior at both target frequencies. Next, a dual-band supercell consisting of four unit cells is presented. After that, the proposed additional step in the design process is applied to the dual-band design to demonstrate its effectiveness on the capturing efficiency of the metasurface harvester. Subsequently, a finite array of 5×4 cells is presented, and its performance is evaluated. Finally,

temporary modifications that are incorporated into the design are discussed, and the fabricated prototype and the measurement results are presented.

4.2 Metasurface Unit Cell Design

The absorption characteristics and the number of operating frequencies of metasurface harvesters are influenced by the shape and the number of resonators within the structure. By combining multiple resonators of different sizes or shapes, each resonator and their combination can resonate at its operating frequency, allowing the structure to absorb energy at multiple distinct frequency bands. We propose a dual-band metasurface harvester operating at 2.45 GHz and 5.2 GHz. These frequency bands correspond to the 2.45 GHz Wi-Fi band already introduced in Chapter II and the 5.2 GHz Wi-Fi band, which is an increasingly common Wi-Fi standard (IEEE 802.11ax/be). Due to the ubiquitous availability of Wi-Fi signals, both frequencies are ideal for capturing ambient RF energy.

As we are targeting two frequencies, the design of our proposed dual-band metasurface harvester proceeds in two steps. First, a single-band metasurface harvester is designed and optimized individually for each of the two desired frequencies; the respective single-band metasurface harvesters are labeled as “M1” and “M2” in Figure 4.1 (a) and Figure 4.1 (b), respectively. Recall that the top layer of the unit cell consists of two rectangular metallic rings of equal dimensions, positioned on the opposite sides of a gap of width g.

M1 is the single-band metasurface harvester operating at 2.45 GHz that was introduced in Chapter II. A resonance analysis for M1 was also discussed, providing a valuable design tool to determine the dimensions of M2, which is tailored for the target frequency of 5.2 GHz.

To design M2, the half-guided wavelength at the resonant frequency of 5.2 GHz is calculated using Equation (2.6) and found to be 22.06 mm. Similar to the discussion for M1 in Chapter II, for M2 the rectangular rings have inner and outer lengths of b3-W2 and b3 along the y-axis, and b4-W2 and b4 along the x-axis, respectively. The average of these inner and outer lengths is denoted by the red dashed line (La2) in Figure 4.1 (b). In calculating this length, the widths of the two microstrip lines in the middle and the gap “g” between them are subtracted as depicted in Equation (4.1).

$$La2=4\times b_3+2\times b_4-4\times W2 \tag{4.1}$$

The dimensions of the M2 geometry are computed so that half the length of La2 closely approximates the half-guided wavelength at 5.2 GHz. Subsequently, the design parameters are optimized to achieve maximum capturing efficiency at this frequency. The final optimized parameters, as presented in Table 4.1, result in a half-length of La2 equal to 25.68 mm — a value not so far from to the half-guided wavelength at 5.2 GHz.

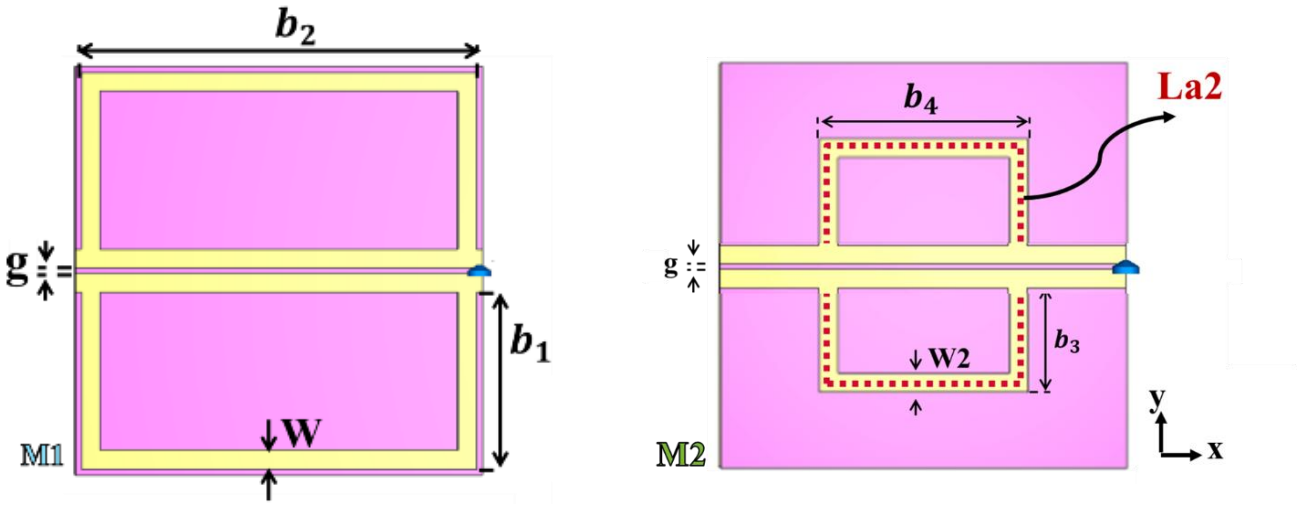

(a) (b)

Figure 4.1 The geometry of the single-band metasurface unit cell for (a) M1 and (b) M2.

In Figure 4.1, at the end of the gap between the two microstrip lines, a resistive load is placed in each design of M1 and M2 to collect most of the absorbed power. The values of these resistive loads are obtained individually for each design (see Table 4.1) by optimizing the collected power at the load at the targeted frequency. The top layer of both designs is placed on the 2.36 mm thick Arlon DiClad 880 substrate. The design and optimization of the proposed structures are carried out using the EM simulation software CST Studio Suite 2021, with a full-wave frequency domain solver, where the unit cell—that is implicitly in a periodic boundary condition—was excited by a normal incident plane wave with polarization along the y-axis. The periodicity of the metasurface unit cell is 0.22 λ_0 at 2.45 GHz, and 0.47 λ_0 at 5.2 GHz.

Table 4.1 Resonator parameters.

Design	b_1 (mm)	b_2 (mm)	b_3 (mm)	b_4 (mm)	R_{load} (Ω)	g (mm)	*l* (mm)	W=W2 (mm)
M1	11.8	26.5	-	-	700	0.35	27.3	1.26
M2	-	-	7.1	14	250	0.35	27.3	1.26

Figure 4.2 (a) and (b) show the simulated efficiencies of the single-band unit cell of the metasurface harvesters M1 and M2, respectively. The absorption and capturing efficiencies of M1 are 99% and 94% at 2.45 GHz, whereas, for M2, they are 99% and 96% at 5.2 GHz. As the chosen substrate is low-loss, only a small amount of the absorbed energy is dissipated in it. Recall from Chapter II that the capturing efficiency is given by the ratio of power delivered to the resistive load and the available incident power at the metasurface (Equation (2.1)).

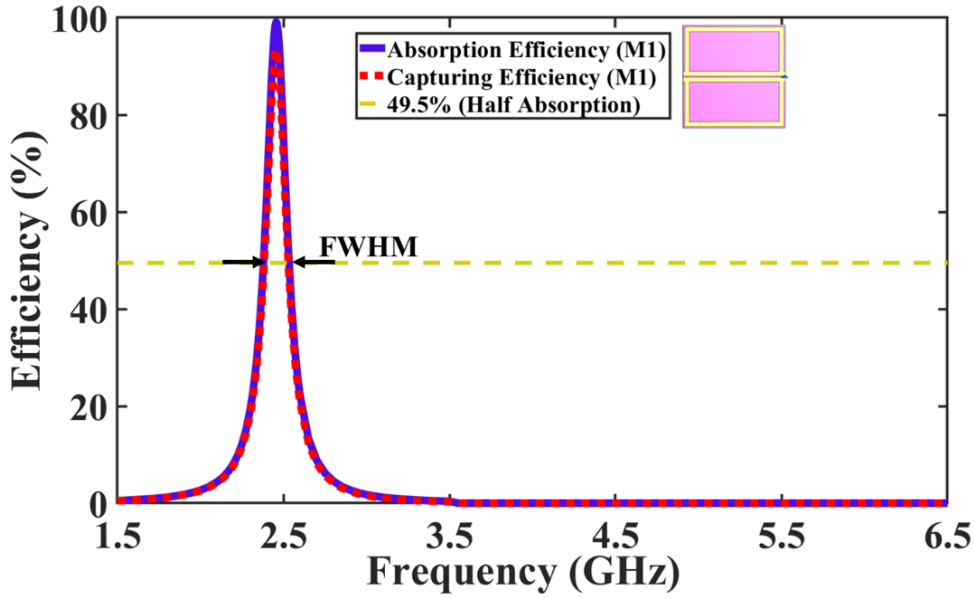

(a)

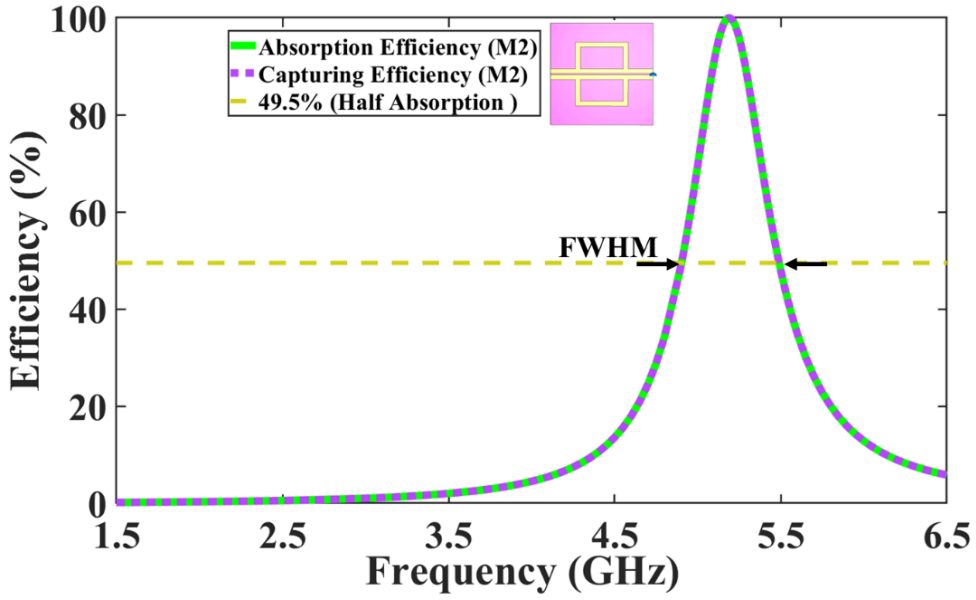

(b)

Figure 4.2 Individually simulated efficiencies for (a) M1 and (b) M2.

The full width at half maximum (FWHM) absorption bandwidths ($\triangle f$) are 0.154 GHz (2.38 to 2.534 GHz) for M1 and 0.59 GHz (4.9 to 5.49 GHz) for M2, as shown in Figure 4.2. The Q-factor of each resonator M1 and M2 can be calculated by Equation (2.3).

The Q-factors for M1 and M2, with the corresponding center frequencies of 2.45 GHz and 5.2 GHz, are 16 and 9, respectively. Q(f1) has a lower value compared to Q(f2), which demonstrates that M1 has sharper resonance compared to M2.

The single-band design M2 demonstrates a wider absorption bandwidth compared to M1, which can be attributed to both designs maintaining the same line width (W=W2) as seen in Figure 4.1. Typically, as the operating frequency increases, the dimensions of the corresponding resonator must decrease to preserve the absorption bandwidth.

Building on the discussion in Chapter II regarding the effect of varying the line width "W" of M1, Figure 4.3 illustrates the impact of adjusting the line width W2 on the performance of the M2 design. As W2 increases, the average length La2 decreases since the inner length is reduced while the outer length remains unchanged. Consequently, the corresponding resonance frequency increases, as shown in Figure 4.3.

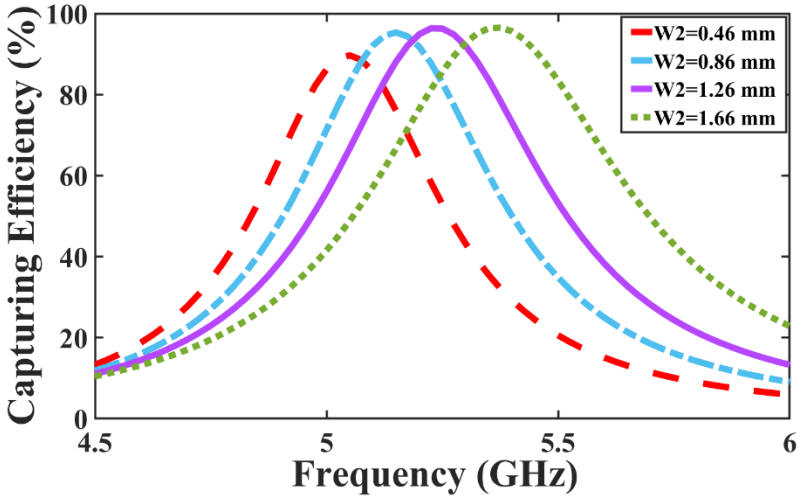

Figure 4.3 Impact of varying "W2" on the performance of the single-band unit cell of M2.

Table 4.2 presents the Q-factor, capturing efficiencies, and approximate characteristic impedances (Zc) for the M2 design at various W2 values. As shown, increasing the line width W2 reduces the Q-factor while slightly enhancing the capturing efficiency—consistent with the behavior observed for M1, as discussed in Chapter II. As the line width increases, the corresponding characteristic impedance decreases, leading to a slight improvement in the unit

cell's capturing efficiency. The characteristic impedances are computed using the ADS LineCalc tool.

Notably, the M2 design achieves a satisfactory performance with a line width of 1.26 mm at the targeted frequency, aligning with the results for M1, which also demonstrated good performance at this width, as discussed in Chapter II.

Table 4.2 Performance values of the single-band M2 design for various width values "W2".

W2 (design M2)	Frequency (GHz)	Capturing efficiency (%)	FWHM (GHz)	Q-factor	Z_c (Ω)
0.46 mm	5.05	90	4.81-5.29 (0.48)	10.5	167
0.86 mm	5.15	95	4.894-5.41 (0.516)	10	139
1.26 mm	5.2	96	4.958-5.53 (0.572)	9	122
1.66 mm	5.37	96	5.046-5.709 (0.663)	8	110

After evaluating the performance of M1 and M2 individually, we can now move to the next step in designing our metasurface harvester, namely, integrating the two resonators M1 and M2 into a single structure. This is done in the dual-band design shown in Figure 4.4. A resistive load (R_{load}) is positioned at the end of the gap between the two microstrip lines. The value of the load (300 Ω) is obtained by optimizing the capturing efficiency of the design, which is a compromise between the optimum load values of the single-band designs at 2.45 GHz and 5.2 GHz. The resonance frequencies of the dual-band design with the initial dimensions of M1 and M2 are 2.24 GHz and 5.12 GHz. These frequency shifts are due to the integration of M1 and M2 into a single structure with common microstrip lines. Therefore, inspired by the parameter study discussed in Chapter II, the lengths b1, b2, b3, and b4 are slightly readjusted to account for the coupling introduced between M1 and M2. These lengths have been chosen as they can be easily adjusted without impacting the periodicity of the cell. This readjustment of the dimensions and the load value allows the proposed metasurface design to work efficiently at both targeted frequencies. The corresponding dimensions of the readjusted dual-band design are provided in Table 4.3.

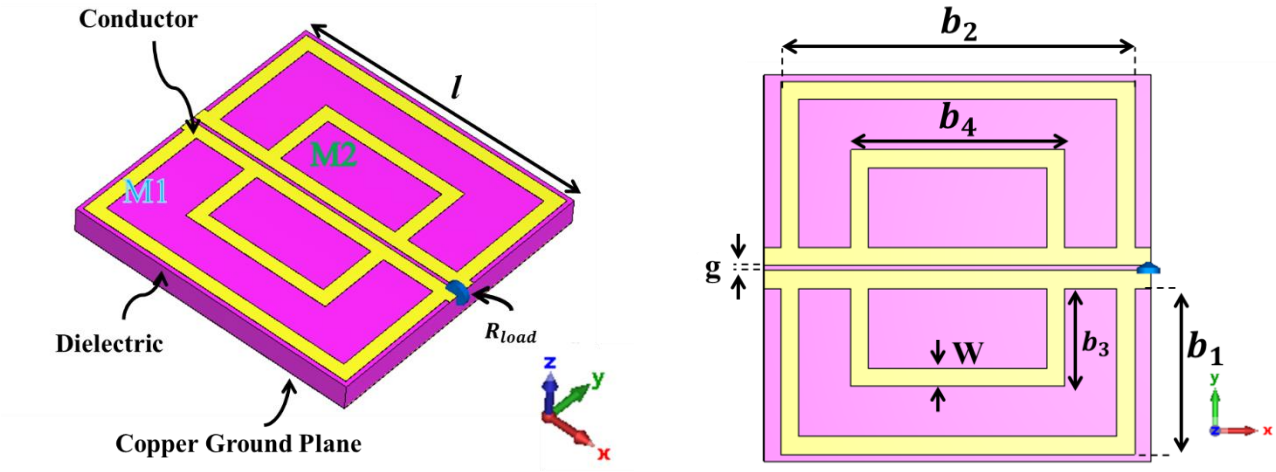

(a) (b)

Figure 4.4 Schematic of the proposed dual-band metasurface unit cell: (a) 3-D view; (b) top view.

Table 4.3 Dual-band parameter values.

Design	b_1 (mm)	b_2 (mm)	b_3 (mm)	b_4 (mm)	R_{load} (Ω)	g (mm)	*l* (mm)	W=W2 (mm)
Dual-band	11.7	25	6.9	13.9	300	0.35	27.3	1.26

Figure 4.5 compares the magnitudes of the reflection coefficient for the proposed dual-band metasurface unit cell with the inclusion of the 300 Ω resistive load at the end of the microstrip lines and in its absence. Without the presence of the resistive load, the metasurface harvester exhibits two weak resonances, and its surface impedance fails to match that of free space. However, with the optimum $R_{load,}$ two minima of -13 dB at 2.45 GHz and -14 dB at 5.2 GHz are observed. Note that the inclusion of the resistive load within the metasurface unit cell has a negligible effect on the resonance frequencies.

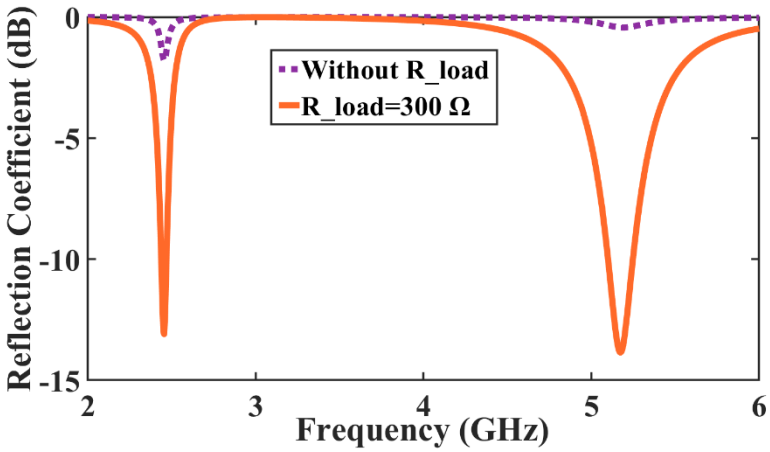

Figure 4.5 Simulated reflection coefficients of the proposed dual-band unit cell without load and with R_{load} = 300 Ω.

The absorption efficiency of the dual-band metasurface harvester is presented in Figure 4.6, reaching maxima of 94% at 2.45 GHz and 96% at 5.2 GHz. Additionally, the figure shows the capturing efficiency, with peak values of 88% at 2.45 GHz and 92% at 5.2 GHz. Therefore, the energy dissipation in the dielectric layer and metallic conductors is at most 6% for both resonance frequencies, and most of the absorbed RF energy is collected by the resistive load.

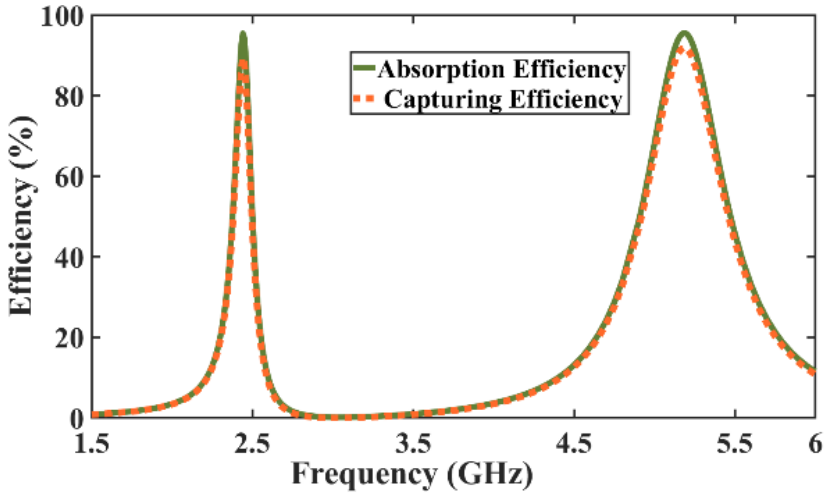

Figure 4.6 Simulated efficiencies for the dual-band metasurface harvester.

Figure 4.7 illustrates the intended resonances at 2.45 GHz and 5.2 GHz, highlighting the surface current distribution. The subfigure (a), corresponding to 2.45 GHz, shows the surface current primarily distributed along the outer ring, with two red arrows placed outside the unit cell to indicate the resonance location. The second subfigure, corresponding to 5.2 GHz, depicts the surface current concentrated on the inner ring, with red arrows positioned between the two rings to represent the inner ring resonance. In both subfigures, the arrows start

from a purple star — representing a point of minimum current — increase to a maximum at the center, and then return to a minimum at the opposite purple star. As observed in Chapter II for the single-band design, this pattern indicates the resonance as occurring between two points of minimum current and a maximum in between.

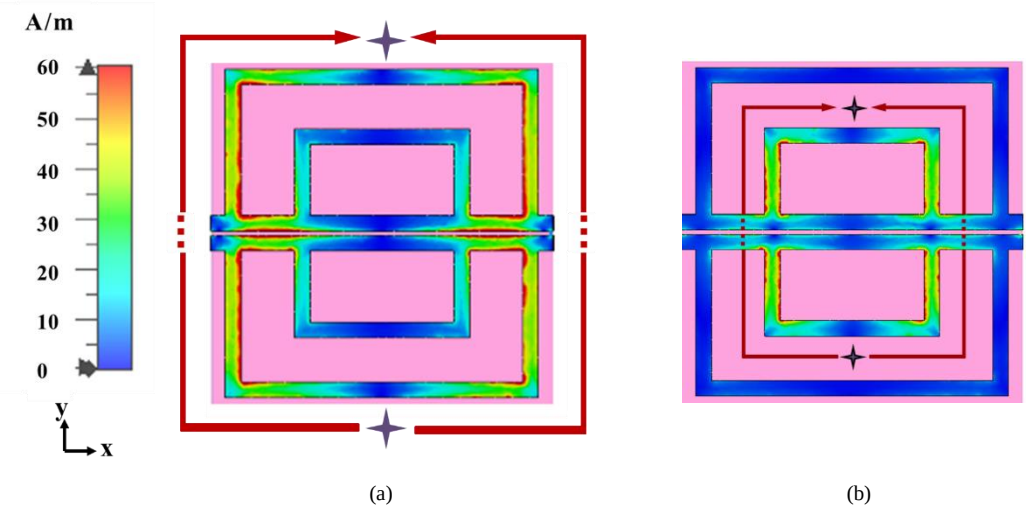

(a) (b)

Figure 4.7 Surface current distribution at: (a) 2.45 GHz, (b) 5.2 GHz.

A parameter study is presented in the following section to investigate the performance of the dual-band metasurface harvester further.

4.2.1 Parameter Study

Based on the resonances observed in Figure 4.7, where the resonance paths are primarily influenced by the lengths of b1 and b2 for the outer ring and b3 and b4 for the inner ring, this section presents the impact of varying these lengths on the operating frequencies. In all parameter studies, only a single parameter is varied at a time while the others are kept constant.

The lengths b1 and b2 of the outer ring are expected to influence the lower resonance frequency, whereas the lengths b3 and b4 of the inner ring are expected to influence the higher resonance frequency. As discussed in Chapter II.2.1, we expect that increasing either length results in a decrease in the corresponding resonance frequency. This is indeed observed in Figure 4.8 and Figure 4.9; the detailed values are listed in Table 4.4 and Table 4.5.

It can be observed that the two resonators operate almost independently, as the changes in the lengths of each resonator (M1 or M2) only slightly affect the resonance frequency of the other resonator.

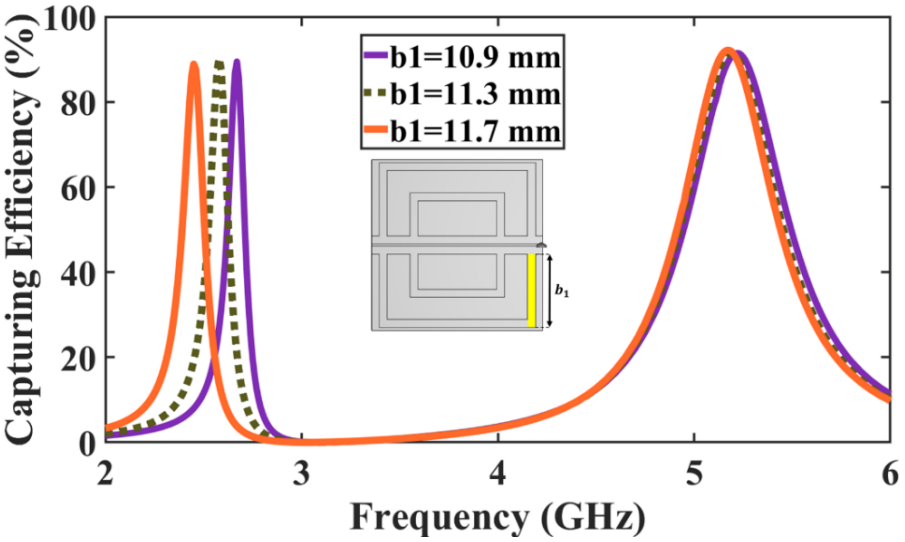

(a)

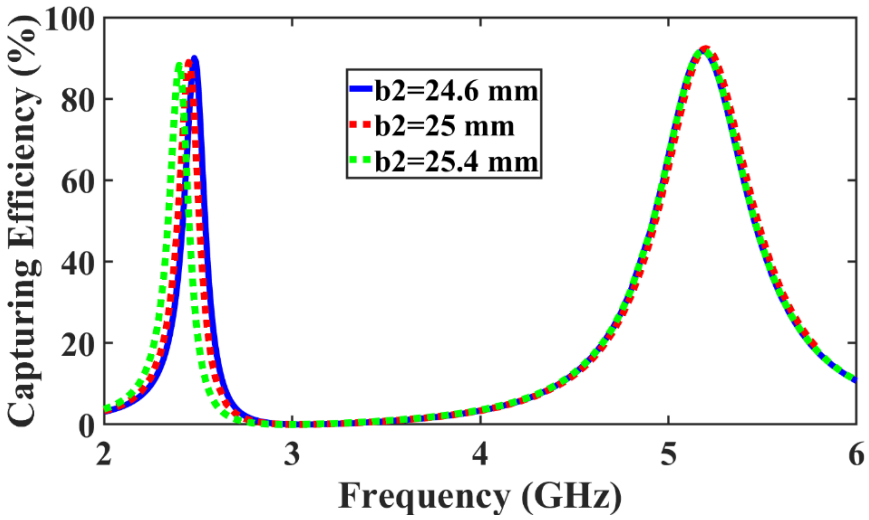

(b)

Figure 4.8 Impact on the operating frequency by changing the lengths (a) b1 and (b) b2.

Table 4.4 Capturing efficiency as a function of b1 and b2.

b1 (mm)	Frequency (GHz)	Capturing efficiency (%)	Frequency (GHz)	Capturing efficiency (%)
10.9	2.67	~ 88	5.22	~ 91
11.3	2.58	~ 88	5.21	~ 91
11.7	2.45	88	5.2	92
b2 (mm)	**Frequency (GHz)**	**Capturing efficiency (%)**	**Frequency (GHz)**	**Capturing efficiency (%)**
24.6	2.48	~ 90	5.2	92
25	2.45	88	5.2	92
25.4	2.4	~88	5.2	92

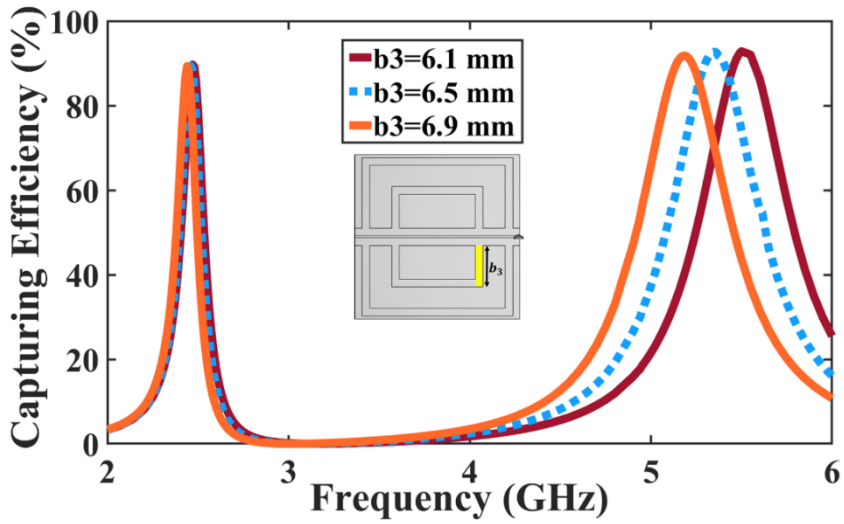

(a)

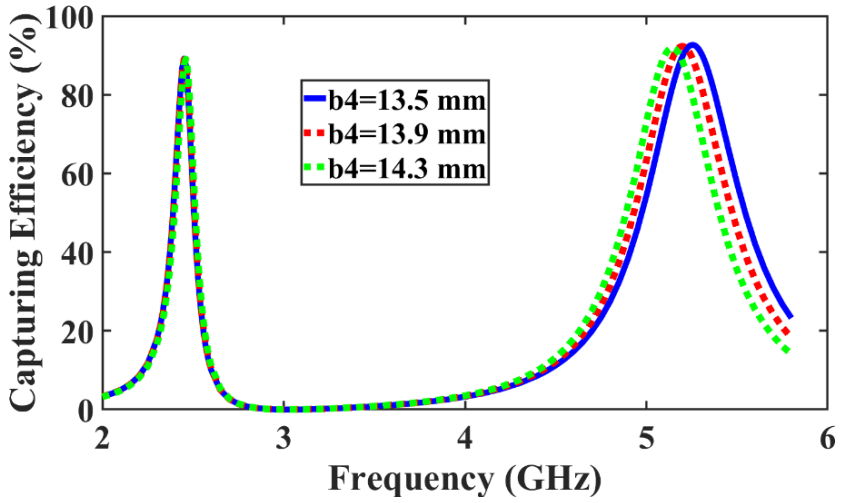

(b)

Figure 4.9 Impact on the operating frequency by changing the lengths (a) b3 and (b) b4.

Table 4.5 Capturing efficiency as a function of b3 and b4.

b3 (mm)	Frequency (GHz)	Capturing efficiency (%)	Frequency (GHz)	Capturing efficiency (%)
6.1	2.46	~ 88	5.5	~ 92
6.3	2.46	~ 88	5.35	~ 92
6.9	2.45	88	5.2	92
b4 (mm)	**Frequency (GHz)**	**Capturing efficiency (%)**	**Frequency (GHz)**	**Capturing efficiency (%)**
13.5	2.45	88	5.15	~ 92
13.9	2.45	88	5.2	92
14.3	2.45	88	5.26	~ 92

Analyzing the major parameters helped to identify the geometry of the dual-band metasurface harvester at the desired frequencies. In the following section, we move to the next step of the design methodology, namely that of the supercell, which is discussed below.

4.3 Metasurface Supercell Design

Following the unit cell design, we study the supercell which is obtained by connecting cells to one another in rows, with the cell terminating the row being connected to a resistive load. Thus, the total collected power of each row is directed to a single load.

Figure 4.10 (a) shows that our proposed dual-band supercell consists of 4 cells (N=4) along the x-axis with a single resistive load. Periodic boundary conditions along both the x-axis and y-axis are applied, and a Floquet mode is utilized as the excitation port within the CST software for simulating the supercell.

As discussed in Chapter II, the number of cells in the supercell should be chosen to balance the size of the intended application and the amount of power collected at the resistive load.

Based on observations from the single-band design, a supercell with 4 unit cells offers a good tradeoff between size and capturing efficiency. Consequently, we adopted the same configuration for the dual-band design. However, this chapter does not explore configurations with a higher number of cells, as the performance across both bands was satisfactory relative to the supercell size.

As described in the methodology, first, the supercell is designed with an initial load value equal to that of the unit cell (300 Ω). In the next step, the load value needs to be reoptimized; contrary to Chapter II, where we only had to reoptimize it for a single frequency, here we need to find a single load value that is simultaneously good – but not necessarily optimal – for both targeted frequencies. We found said load value to be 140 Ω, which leads to a capturing efficiency of 85% at 2.46 GHz and 66% at 5.18 GHz. This corresponds to an increase in the capturing efficiency compared to its initial value of 66% at 2.45 GHz and 44% at 5.17 GHz for a load of 300 Ω. Figure 4.10 (b) illustrates the comparison plot between the corresponding capturing efficiency for the dual-band supercell with the initial 300 Ω load, and the reoptimized 140 Ω.

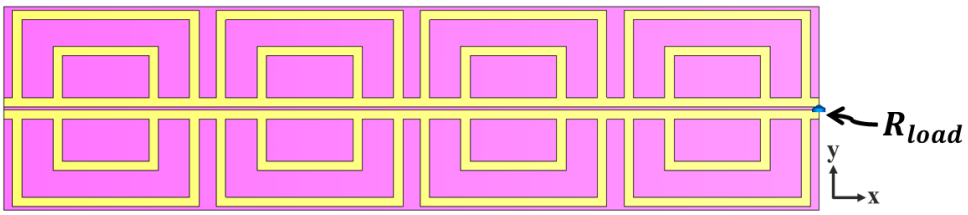

(a)

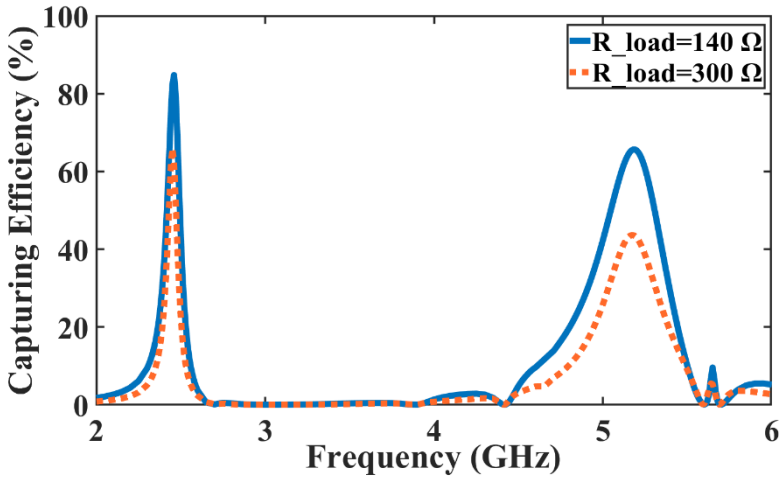

(b)

Figure 4.10 (a) Schematic of the proposed supercell and (b) compared simulated capturing efficiency for an initial load value of 300 Ω and reoptimized 140 Ω.

The intermediate design step resulted in an improvement in the capturing efficiency of the dual-band supercell by at least 19% for each targeted frequency. In the next section, a finite array will be presented, along with a discussion of its simulated results.

4.4 Metasurface Finite Array Design

Following the proposed design strategy, a finite array of 5×4 cells was designed and simulated with a time domain solver under plane wave excitation with a linear polarization along the y-axis in CST software. The 4 cells in each row are chosen based on the supercell study, and the five rows are due to having sufficient rows in the center (at least three rows in the middle; recall the discussion about the central rows in Chapter II). These choices are considered to keep the array as compact as possible.

Figure 4.11 depicts five rows consisting of 4 single cells each; every row is terminated by a 140 Ω resistive load. To calculate the capturing efficiency of the finite array of the proposed dual-band metasurface, we proceed as in the calculation for the single-band array

(Equation (2.1)), where P_{in} is obtained from the integration of the Poynting vector over the metasurface area.

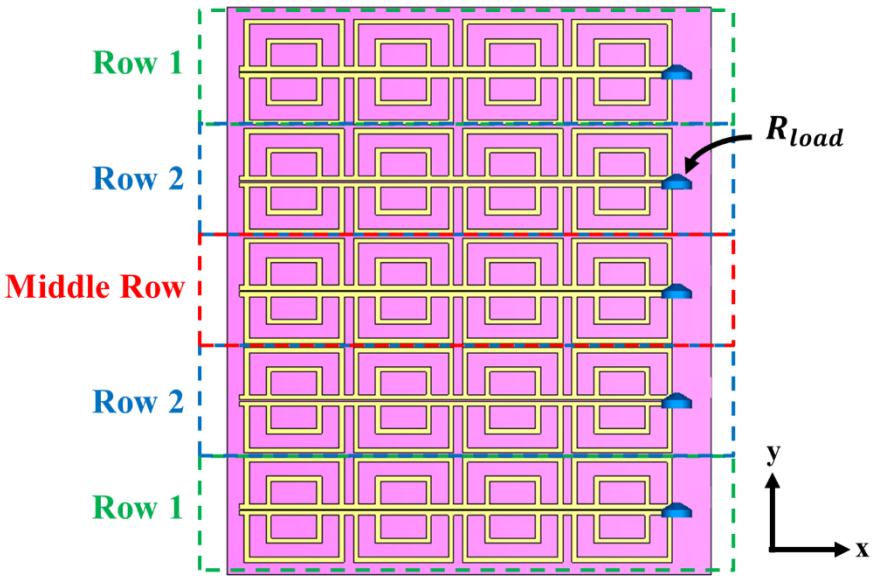

Figure 4.11 Finite array of 5×4 unit cells of the proposed dual-band metasurface harvester with row numbers.

As discussed in Section II.4 regarding the finite array, the middle row and Row 2 exhibit a better performance at the targeted frequencies; as a result Figure 4.12 presents only the capturing efficiency of these rows. Figure 4.12 (a) and (b) correspond to the capturing efficiency with a resistive load of 300 Ω (initial) and 140 Ω (reoptimized), respectively. The corresponding values are summarized in Table 4.6 and Table 4.7.

As in the single-band design, the capturing efficiency of the middle row of the dual-band design is higher than the one for Row 2. Comparing the performance of the middle row at 2.45 GHz and 5.2 GHz shows that the dual-band design is experiencing lower efficiency at the second frequency. Note that in comparison to the supercell, there is a more pronounced difference between the performance at 2.45 GHz and 5.2 GHz. This is because the array is of finite dimension, whereas the supercell is simulated in periodic ones.

A comparison of Figure 4.12 (a) and (b) confirms that reoptimizing the resistive load leads to an enhancement in the capturing efficiency, as anticipated.

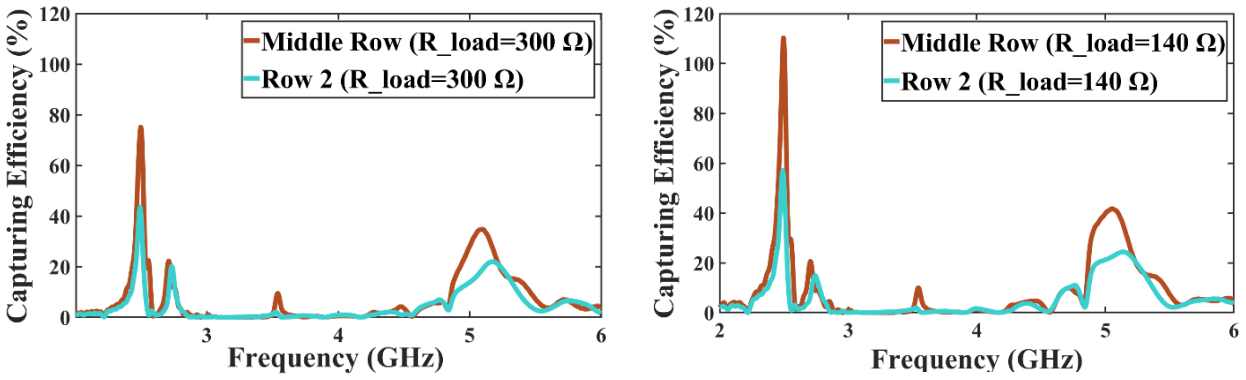

(a) (b)

Figure 4.12 Simulated capturing efficiencies of the middle row and Row 2 of the proposed dual-band design corresponding to (a) R_{load} =300 Ω and (b) R_{load} =140 Ω.

Table 4.6 Capturing efficiencies of different rows at the low frequency for the load of 300 Ω and 140 Ω.

Row number	Frequency (GHz)	Capturing efficiency (%)	R_{load} (Ω)
2	2.5	43	300
Middle	2.5	75	300
2	2.5	57	140
Middle	2.5	110	140

Table 4.7 Capturing efficiencies of different rows at the high frequency for the load of 300 Ω and 140 Ω.

Row number	Frequency (GHz)	Capturing efficiency (%)	R_{load} (Ω)
2	5.16	21	300
Middle	5.09	32	300
2	5.12	25	140
Middle	5.04	42	140

The middle row has the highest capturing efficiency at the two frequencies compared to the other rows. However, as discussed in Chapter II, the middle row is not a suitable representative for evaluating the performance of the design; rather, its adjacent rows (Row 2) should be considered as well. As discussed in Chapter II, indeed, central rows are more appropriate as they account for differences between the capturing efficiencies of its rows.

Compared to the initial value of the load (300 Ω) of the unit cell, when the load is derived from the supercell optimization, the capturing efficiency of the central rows of the proposed finite array increases from 53% at 2.5 GHz to 74% at 2.5 GHz, and from 24% at 5.13 GHz to 30% at 5.09 GHz, as shown in Figure 4.13.

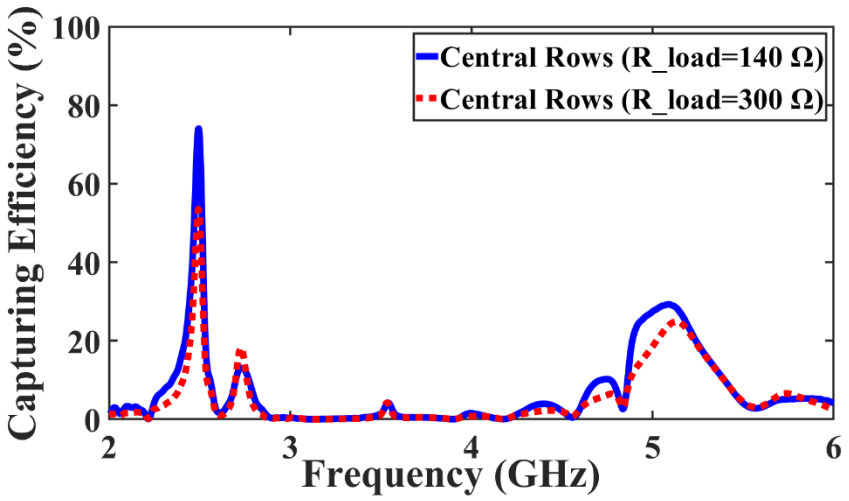

Figure 4.13 Simulated capturing efficiency of the central rows for the initial R_{load} =300 Ω and reoptimized R_{load} =140 Ω.

In Figure 4.13, the FWHM capturing bandwidth corresponding to the reoptimized load of 140 Ω is 0.064 GHz (2.456 to 2.52 GHz) for the low frequency and 0.518 GHz (4.872 to 5.39 GHz) for the high frequency. The corresponding Q-factors, calculated using Equation (2.3), are 39 and 10. The higher Q-factor indicates a relatively narrower bandwidth at 2.5 GHz, whereas the lower Q-factor indicates a wider bandwidth at 5.2 GHz.

Similarly to the single-band metasurface, the proposed dual-band design exhibits polarization sensitivity, with the array demonstrating zero capturing efficiency when excited by a normal incident plane wave with polarization along the x-axis.

As the final step in analyzing the design performance, we follow the discussion of fabrication and measurement of our proposed dual-band metasurface harvester.

4.5 Realization and Measurement

As argued in the analysis of Section II.5, the middle row of the metasurface finite array is chosen for measuring the capturing efficiency as its edge effects are minimal (effective area 0.00298 m^2). A modification same as for the single-band metasurface design is made at the end of this row in order to measure the RF output power.

To have a fair comparison between the simulation and measurement result, a finite array with the same modifications is designed and simulated under plane wave excitation with a linear polarization along the y-axis. In the simulation, the modification of the middle row is

implemented in four steps: first, the 140 Ω resistive load between the two microstrip lines is removed. Second, slanted extensions are added to the ends of the microstrip lines to increase the gap between them. Third, a 50 Ω load is placed between the end of each line and the ground to replicate the input impedance of the SMA connectors. The remaining rows are each terminated with a 150 Ω resistive load due to the availability of Surface Mount Resistors (SMD) in our lab. In the fourth and final step, the substrate is cut to accommodate the shape of the connectors.

The simulated capturing efficiency of the modified metasurface harvester is illustrated in Figure 4.14. At 2.5 GHz, the capturing efficiency is 58%, with an FWHM of 0.058 GHz (2.472 GHz to 2.53 GHz) and a Q-factor of 43. At 5.1 GHz, the efficiency is 60%, with an FWHM of 0.248 GHz (4.98 GHz to 5.228 GHz), corresponding to a Q-factor of 20. The temporary modifications in the middle row of the finite array led to an increase in efficiency at 5.1 GHz, while a decrease was observed at 2.5 GHz. This effect can be attributed to the fact that the unmodified dual-band design already showed a higher capturing efficiency at 2.5 GHz than at 5.1 GHz (Figure 4.13), indicating better matching conditions with free space. Incorporating extension lines into the original design altered the matching condition at 2.5 GHz. Although this enhancement is beneficial at 5.1 GHz, it was unintended, as the extensions were introduced solely for preliminary metasurface measurements and are not a permanent part of the proposed design.

Nonetheless, we recognize that the performance at the second frequency requires further enhancement, which could be achieved by increasing the number of rows in the array, resulting in greater similarity between the array and the supercell in the sense that we are closer to the periodic boundary conditions implicit in the simulation of the supercell. We therefore would expect the larger array of the dual-band metasurface harvester to exhibit a higher capturing efficiency at the second frequency of 5.1 GHz (since the supercell showed a good performance at both frequencies as shown in Figure 4.10.)

Figure 4.14 further illustrates the sensitivity of the dual-band design's capturing efficiency to small variations in the lengths b1 and b3. At the low frequency of 2.5 GHz, the capturing efficiency changes by around 15% for each 0.1 mm increase in b1, while the high frequency of 5.1 GHz remains unaffected by these changes, as shown in Figure 4.14 (a). Conversely, the design shows less sensitivity to 0.1 mm variations in b3 at 5.1 GHz, with the low frequency of 2.5 GHz remaining unchanged, as shown in Figure 4.14 (b). While these

length variations primarily affect the capturing efficiency, they cause only small shifts in the resonant frequencies — changes in b1 result in small frequency shifts around 2.5 GHz, and changes in b3 produce minimal shifts around 5.1 GHz. It is important to note that b1 and b3 are presented as representative parameters to highlight the design's sensitivity to these length changes. Other geometric factors, such as the line width and additional lengths like b2 and b4, may also influence the design's overall performance.

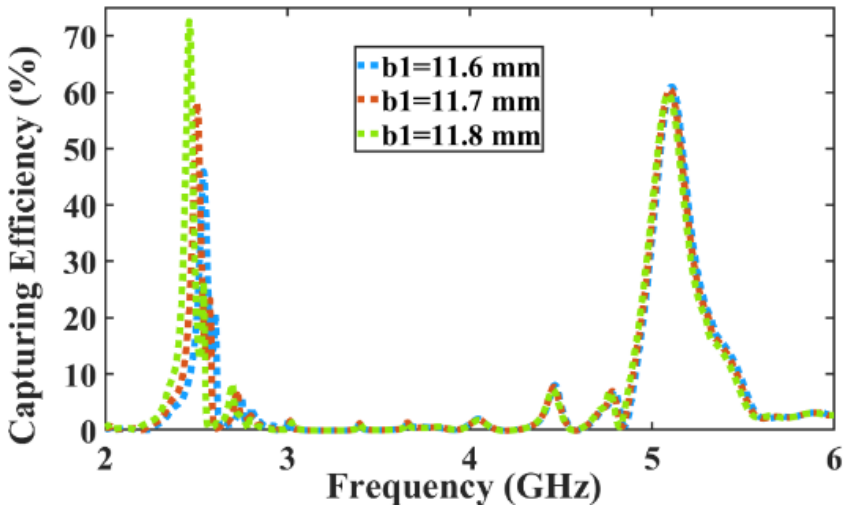

(a)

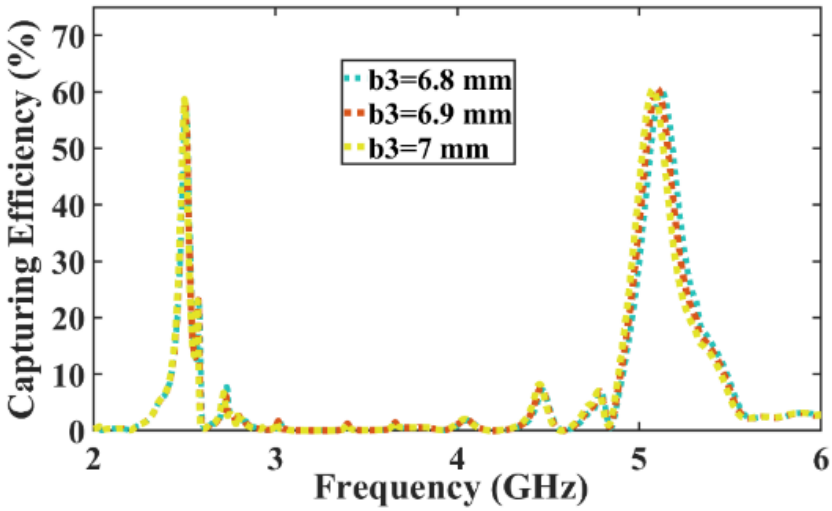

(b)

Figure 4.14 Simulated capturing efficiencies of the middle row of the modified finite array for (a) different lengths of b1 and (b) different lengths of b3.

Figure 4.15 depicts the simulated capturing efficiency of the average row (A.R.); we remind that the latter is the arithmetic mean of the capturing efficiencies of the central rows that we have introduced and motivated in Chapter II. Table 4.9 provides the corresponding performance values. Additionally, Figure 4.15 illustrates the simulated capturing efficiency of

the average row under the oblique incidence angle of 20 degrees; this comparison plot shows that the proposed dual-band design has a good performance under an oblique incidence of 20 degrees (41% at 2.51 GHz and 33% at 5.11 GHz).

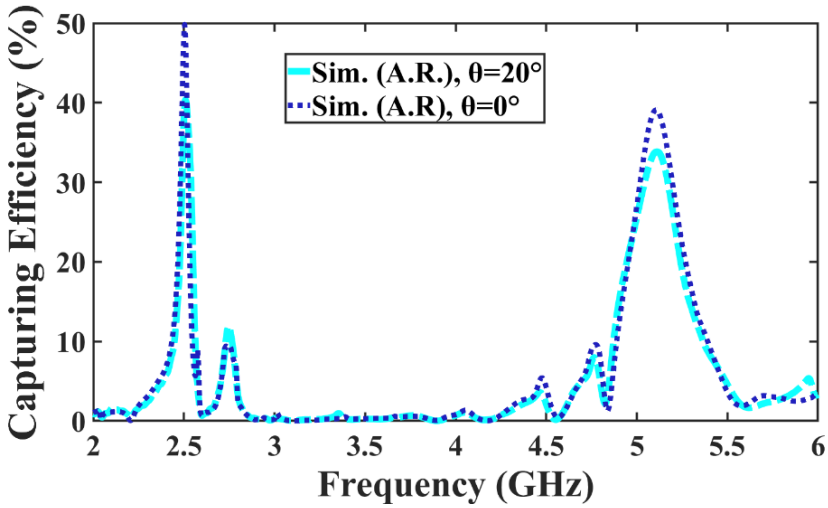

Figure 4.15 Comparison between simulated average row (A.R.) at different incidence angles.

A dual-band metasurface harvester finite array consisting of 5 rows was fabricated on a 2.36 mm thick Arlon DiClad 880 dielectric substrate, as shown in Figure 4.16. As done for the single-band, to measure the collected RF power (P_{dl}) from the middle row of the dual-band design, a power sensor (Keysight U8488A 10MHz - 67GHz power sensor) is used. The full measurement is performed in an anechoic chamber, where the metasurface is located at the far field distance of 2.39 m from the horn. The incident power on the middle row of the array can be found by Friis' equation. The gain of the horn and the emitted power by the generator for both frequencies are presented in Table 4.8.

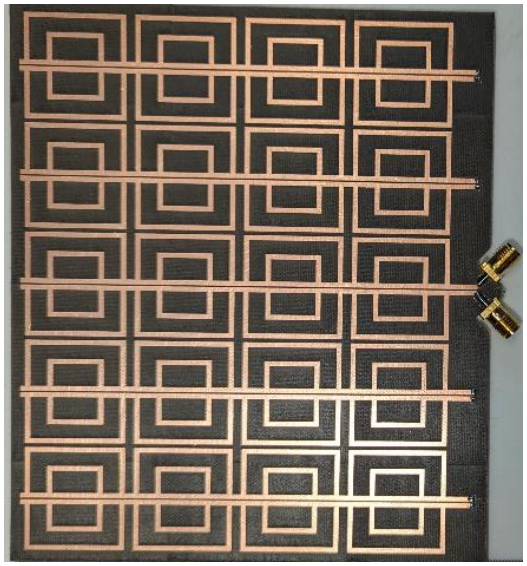

Figure 4.16 Fabricated dual-band metasurface array with the soldered connectors.

Table 4.8 Transmitter and propagation parameters.

Frequency (GHz)	Gain of the horn (dBi)	Emitted power measured at the horn input (dBm)
2.5	6.4	24.4
5.1	9.7	23.1

Figure 4.17 illustrates the comparison between the simulated average row and measured capturing efficiency under normal incidence; the corresponding values are summarized in Table 4.9.

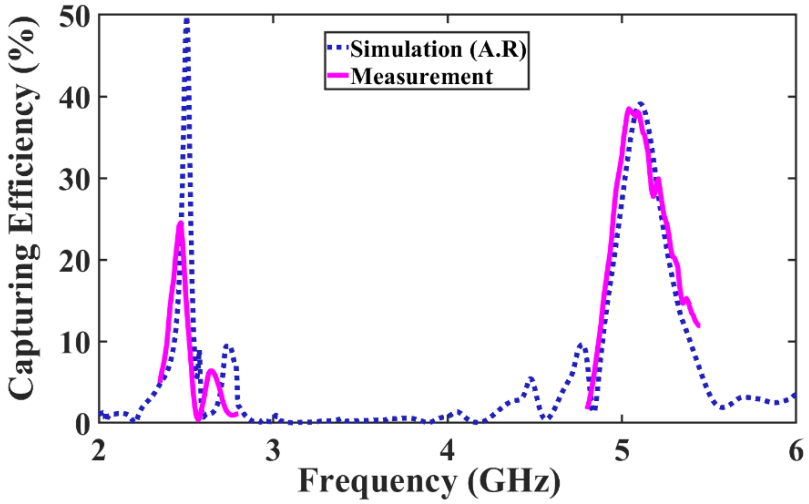

Figure 4.17 Comparison between the simulated capturing efficiency of the average row (A.R.) and measured middle row at normal incidence.

Table 4.9 Performance values for simulated middle row (M.R.), average row (A.R.), and measurement.

Sim/Meas.	Capturing efficiency (%)	Frequency (GHz)	FWHM ($\triangle f$ (GHz))	Q-factor	Step frequency size (MHZ)
Sim. (A.R)	49.8	2.5	2.474-2.528 (0.054)	46	1
Meas.	25	2.47	2.4-2.51 (0.11)	22	10
Sim. (A.R)	40	5.1	4.95-5.268 (0.318)	16	1
Meas.	38.5	5.05	4.92-5.31 (0.39)	13	10

Recall from the comparison plot in Figure 2.19 in Section II.5 that for the single-band design, the simulation, and measurement of the capturing efficiency reveal a good agreement at the low frequency. However, in the case of the dual-band design, the measured capturing efficiency at the low frequency is less than the simulated one. This difference can be attributed to several factors. First, the dual-band design exhibits a narrower bandwidth at the low frequency, corresponding to a higher Q-factor for the average row of 46. However, the Q-factor for the average row in the single-band design is 27. As a result, the capturing efficiency of the dual-band design at the low frequency can be more sensitive with respect to dimensional variations (similar to the discussion in Figure 4.14) and fabrication tolerances. Another minor reason for the observed discrepancy could be the difference in frequency resolution between simulation and measurement. The frequency step size was 1 MHz when performing the simulation, while in the measurement it was 10 MHz. Given the sharp resonance of the dual-band design at the low frequency, it is plausible that the exact peak capturing efficiency was missed during measurement.

At the high frequency, however, the agreement between simulation and measurement is significantly better. This can be attributed to the wider bandwidth (lower Q-factor) of the dual-band design at said frequency, which reduces the sensitivity to dimensional variations and fabrication tolerance, thereby enhancing consistency between simulated and measured results.

Fabrication tolerances, such as variations in substrate thickness or permittivity, can contribute to frequency shifts. According to specifications provided on the substrate packaging (by the manufacturer), the substrate thickness has an error margin of ±0.076 mm, while the permittivity varies by ±0.02.However, generally the measurement is in support of our proposal dual-band metasurface harvester design performance.

Table 4.10 summarizes some existing RF metasurface harvesters proposed in the state of art. In Table 4.10 the following abbreviations are used:

Abbreviation	**Description**
Ref	References
Freq	Frequency
L/Rect	Lumped elements / rectifier present
R/C	Resistor / capacitor present
η_{abs-c}	Unit cell absorption efficiency
η_{MS-c}	Unit cell capturing efficiency
Sim η_{MS-AV} / η_{MS-w}	Simulated capturing efficiency of the average row / whole finite array
Meas η_{MS-MR} / η_{MS-MC}	Measured capturing efficiency of the middle row / middle cell

Table 4.10 Performance comparison of some reported RF metasurface harvesters.

Ref	**Freq (GHz)**	**L/Rect**	η_{abs-c} **(%)**	η_{MS-c} **(%)**	**Cell size (array)**	**Sim** η_{MS-AV}/η_{MS-w} **(%)**	**Meas** $\eta_{MS-MR}/\eta_{MS-MC}$ **(%)**
[42]	5.8	1 R per cell (via used)	93	88	$0.278\lambda_0 \times 0.323\lambda_0$ (5×5)	-	η_{MS_MC} 80% at 5.91 GHz
[83]	3	1 R per cell (RF feed network-Via used)	92	-	$0.153\lambda_0 \times 0.153\lambda_0$ (8×8)	η_{MS_w} without/ with feed network more than 80%	η_{MS_W} with feed network 78% at 2.9 GHz
[133]	2.4	1 R per cell (via used)	99.9	97	$0.2\lambda_0 \times 0.2\lambda_0$ (5×5)	-	η_{MS_MC} 85% at 2.8 GHz
	5.4		99.9	94	$0.45\lambda_0 \times 0.45\lambda_0$ (5×5)		η_{MS_MC} 83% at 5.43 GHz
[97]	5.2	4 C per cell, 12 Rect. (in whole array)	99.9	-	$0.59\lambda_0 \times 0.59\lambda_0$ (6×6)	-	-

Ref	Freq (GHz)	L/Rect	η_{abs-c} (%)	η_{MS-c} (%)	Cell size (array)	Sim η_{MS-AV}/η_{MS-w} (%)	Meas $\eta_{MS-MR}/\eta_{MS-MC}$ (%)
[95]	2.1	10 Rect. (in whole array)	-	-	$0.26\lambda_0 \times 0.26\lambda_0$ (5×5)	-	-
	5.8				$0.713\lambda_0 \times 0.713\lambda_0$ (5×5)		
[94]	2.4	2 Rect. per supercell (N=4)	Close to 100	96	$0.168\lambda_0 \times 0.168\lambda_0$ (7×7)	-	-
	12.6			92.9	$0.882\lambda_0 \times 0.882\lambda_0$ (7×7)		
[96]	1.85	1 Rect. per supercell (N=4)	-	86	$0.21\lambda_0 \times 0.271\lambda_0$ (2-connected array 4×5)	-	-
	2.5		-	83	$0.283\lambda_0 \times 0.367\lambda_0$ (2-connected array 4×5)		
This work	2.45	1 R per supercell (N=4)	94	88	$0.22\lambda_0 \times 0.22\lambda_0$ (5×4)	η_{MS-AV} 74% at 2.5 GHz (without modification)	-
						η_{MS-AV} 49.8% at 2.5 GHz (with modification)	η_{MS-MR} 25% at 2.47 GHz
	5.2		96	92	$0.47\lambda_0 \times 0.47\lambda_0$ (5×4)	η_{MS-AV} 30% at 5.09 GHz (without modification)	-
						η_{MS-AV} 40% at 5.1 GHz (with modification)	η_{MS-MR} 38.5% at 5.05 GHz

Our proposed design is not only compact, as is evident by comparison with [81, 91, 93, 95-97, 132], but it also uses the fewest lumped elements/rectifiers possible compared to [42-44, 75, 89, 94-97, 132-135]. Accordingly, our initial goal in this chapter can be considered satisfied: we have designed a compact single-layer dual-band metasurface harvester whose capturing efficiency was improved by our proposed intermediate design step.

In our work, we analyzed, simulated, and measured the metasurface harvester individually, without any implemented rectifier. The goal was to evaluate the performance of the metasurface design and to optimize its capturing efficiency. In contrast with typical ways of how works based on the interconnected cells method are presented - without discussing the measured capturing efficiency of their metasurface harvesters independently from the rectifier [91, 93-97, 132] - we analyzed and measured our proposed metasurface harvester alone.

Additionally, we have proved that it is conceptually and practically simple to extend our single-band to a dual-band design. Based on this chapter, we conjecture that the design has the potential to be similarly extended to a triple-band design, namely by adding another resonator ring whose dimensions can be found following our design analysis. However, it is important to design a bigger array to include more rows in the center that better resembles the periodic boundary conditions of the supercell that we optimized. In addition, it may prove helpful to increase the width “W” of the lines (accepting an increased cell size) in order to increase the bandwidth at the low frequency, which will in turn increase the resilience to manufacturing errors.

4.6 Conclusion

Building on our proposed single-band design of Chapter II, we have obtained a dual-band metasurface harvester by merging two single-band harvesters. Concretely, we began by individually designing two such metasurface harvesters whose parameters were chosen such as to attain resonance frequencies of 2.45 GHz and 5.2 GHz and near-unity absorption; both were subsequently combined into a single design by positioning them along the shared microstrip lines on either side of the gap. A parameter study confirmed the desirable behavior that changing the dimensions of one resonator has virtually no effect on the performance of the other – despite the fact that they are combined into a shared structure. The dual-band metasurface cell experienced a capturing efficiency of 88% at 2.45 GHz, and 92% at 5.2 GHz, demonstrating that most of the absorbed power was collected by a resistive load.

A key difference to the single-band design of Chapter II is that our proposed additional design step, namely reoptimizing the load of the supercell, is not carried out for one but for two resonance frequencies. Accordingly, we can no longer hope to achieve perfect impedance matching and, therefore, the highest possible capturing efficiency at both frequencies, but

rather, we must find middle ground: a load value resulting in a good efficiency at both frequencies. The capturing efficiency of the supercell with the initial resistive load of 300 Ω was 66% at 2.45 GHz, and 44% at 5.17 GHz while, after the reoptimization of the load to 140 Ω increased the capturing efficiency to 85% at 2.46 GHz, and 66% at 5.18 GHz.

Having identified the suitable load value, a 5×4 array was designed where the capturing efficiency of the central rows experienced its peak of 74% at 2.5 GHz, and of 30% at 5.09 GHz. This constitutes an improvement of 21% at the low frequency and of 6% at the high frequency compared to the initial values. The proposed finite array was fabricated with the necessary modification introduced in Chapter II to carry out the preliminary measurements. Taking into account the central rows, an acceptable agreement was observed between the measured and the simulated capturing efficiencies under normal incidence. The latter peaks at 2.5 GHz with 49.8% and at 5.1 GHz with 40%, while the former peaks at 2.47 GHz with 25% and at 5.05 GHz with 38.5%. Based on the content of this chapter, the work in [136] has been presented.

In summary, the proposed dual-band metasurface RF harvester is compact and capable of collecting RF power at two distinct frequencies using only one resistive load per supercell. Consequently, the entire array requires just five resistors, highlighting the design's minimal component count. Additionally, the harvester features a single-layer structure without vias, with the load positioned on the same layer as the supercells, thereby eliminating the need for a multilayer design. Importantly, we have demonstrated that our approach allows for a straightforward transition from a single-band to a dual-band design, with the potential for further extension to multi-band configurations in a conceptually and practically simple manner. However, it is important to note that the frequency bands may need to be sufficiently spaced apart to avoid mutual coupling and ensure optimal performance. This idea will be explored in future work.

Conclusions and Future Research Directions

Conclusions

Efficient compact RF metasurface energy harvesters operating at Wi-Fi bands (2.45 GHz and 5.2 GHz), targeting low-power IoT devices, are the focus of this thesis. Several key objectives were defined and successfully achieved. The first goal was to design an efficient single-band metasurface RF harvester operating at 2.45 GHz while utilizing a minimal number of lumped elements to collect ambient RF power. The second objective involved enhancing the capturing efficiency of the proposed single-band metasurface RF harvester. The third goal was to design a suitable rectifier circuit to be compatible with the proposed single-band metasurface harvester while employing the minimal components usage. We suggested analyzing and optimizing each design—metasurface and rectifier—individually to enhance the overall performance of the device. As a result, we aimed to simulate, fabricate, and measure both the metasurface and rectifier standalone and evaluate their performances independently. The final and more ambitious goal was to expand the single-band RF metasurface harvester into a dual-band design capable of operating at both 2.45 GHz and 5.2 GHz while maintaining the same low component count. All the proposed designs were targeted to be compact and simple to be fabricated.

After reviewing the existing works on metasurface RF harvesters and highlighting their key advantages and disadvantages, we took the first step towards satisfying our initial goals via Chapter II.

RF energy harvesters typically consist of two main components, a receiver that collects ambient RF power and a rectifier circuit that converts this power into usable DC. In this work, the receiver was implemented using a metasurface due to its high absorption efficiency, which is crucial for overcoming the challenge of low ambient RF power levels. Additionally, metasurfaces offer the advantage of being compact, which is critical for IoT devices such as sound, light, and temperature sensors, which is the target of this work.

In Chapter II, an efficient single-band metasurface RF harvester for IoT applications was proposed, and its design steps were presented. The interconnected cells technique was chosen to increase the collected power from multiple cells while maintaining a planar structure.

In the design steps, first, a compact unit cell was designed to operate at 2.45 GHz. The Arlon Diclad 880 substrate was chosen to minimize losses occurring in the dielectric, and a resistive load of 700 Ω was found as the optimum load value for the unit cell to maximize the collected RF power. A simulated capturing efficiency of 94% is achieved at 2.45 GHz, and less than 5% of the absorbed power is dissipated in the substrate and the metallic parts, which shows that the majority of the absorbed power is collected by the resistive load. The resonances of the proposed unit cell were analyzed, and a parameter study was carried out to identify the impact of varying geometric parameters on the performance and the operating frequency of the proposed single-band metasurface absorber. As the next step in the design's process, a supercell consisting of four cells connected to each other was designed and simulated initially with the same load value as the unit cell. An intermediate step design was proposed at this stage to improve the capturing efficiency of the proposed supercell, and a load value of 115 Ω was found as the optimum for the supercell. By reoptimizing the resistive load value of the supercell, an improvement of 30% in capturing efficiency was obtained, increasing from 62% at 2.45 GHz to 92% at 2.49 GHz. While the adjusted load value caused a frequency shift, it can be reversed by readjusting the dimensions of the resonators in the design. For the last design step, a finite array of 5×4 cells was proposed and simulated. In contrast with the majority of the existing works based on the interconnected cells method, we analyzed the finite array of the metasurface harvester alone, which involved a detailed analysis of each row of the proposed array. Furthermore, we introduced the concept of central rows to evaluate the performance of a metasurface harvester, as analyzing just one middle row was not sufficient to draw meaningful conclusions about a design's performance. A simulated capturing efficiency of 90% was achieved by the optimum load value of 115 Ω for the central rows of the finite array, which comprise three rows in the middle. The capturing efficiency of the central rows is the arithmetic mean of the efficiencies of the middle row and its two neighbors; accordingly, it can be considered as an average row.

To validate the simulated performance of the metasurface harvester, the design was fabricated with modifications introduced to enable measurements with typical RF instruments. However, these modifications caused the simulated capturing efficiency of the middle row to drop by 24%. The measured capturing efficiency of the middle row of the fabricated metasurface harvester shows a good agreement with the simulated average row. The former is 61% at 2.49 GHz, whereas the latter is 73% at 2.54 GHz.

By following our design steps, an individual analysis of the proposed single-band metasurface RF harvester was successfully conducted.

Once the RF power is collected, it can be converted to DC by means of a rectifier. The resistive load of the proposed metasurface harvester was representative of the rectifier's input impedance. Moreover, as the output of the metasurface harvester is differential, in Chapter III, the resistive load of the metasurface is replaced by a suitable differential rectifier.

In Chapter III, first a brief background regarding the rectifier and its primary components were brought. Then, the proposed differential rectifier is discussed, and the circuit is optimized to operate at 2.49 GHz to have the same operating frequency as the fabricated single-band metasurface. An SMS7630 Schottky diode was chosen due to the low threshold voltage, which makes it suitable for a low-power environment. The proposed differential rectifier was simulated using ADS and Momentum co-simulation, where the rectification efficiency of 58% at -2.7 dBm of the total input power of the rectifier is achieved at the operating frequency of 2.49 GHz. The designed layout was adjusted by adding an extension at the input of the circuit to be suitable for measurements using a typical RF instrument. The rectification efficiency drops by around 4.3% due to the introduced modifications. However, the extensions can be removed at any stage if necessary, as they do not affect the operating frequency and have a slight impact on the efficiency. The modified rectifier was fabricated and measured. The measured rectification efficiency at 2.45 GHz is 46.4% for -2.7 dBm of total input power, which is in a good agreement with the simulations. Then, the fabricated rectifier and single-band metasurface harvester were connected using two short cables in order to evaluate the measured total RF to DC efficiency. The total measured efficiency has a good performance for the low input power range level.

In Chapter IV, a dual-band metasurface RF harvester is proposed based on the single-band design and its design methodology presented in Chapter II. All the steps in the design of the single-band and dual-band metasurfaces were performed using CST Studio Suite 2021.

The dual-band design is achieved by combining two single-band structures, each operating at 2.45 GHz and 5.2 GHz. The final unit cell design was optimized to account for the mutual coupling added by two resonators. A resistive load of 300 Ω was found to be the best load trade-off between the two frequencies, as a result, one load is collecting RF power at these two distinct frequencies. The corresponding simulated capturing efficiency is 94% at 2.45 GHz

and 96% at 5.2 GHz. The metasurface harvester at the high frequency demonstrates a wider absorption bandwidth compared to the low frequency. Following the unit cell, a supercell of four cells was designed and simulated. Initially, with the load value of the unit cell, and after the additional step design was taken, which was reoptimizing the resistive load value. A good trade-off between the capturing efficiency of the supercell at 2.45 GHz and 5.2 GHz was obtained with the load value of 140 Ω. The capturing efficiency of the supercell improved from 66% at 2.45 GHz to 85% at 2.46 GHz and from 44 % at 5.17 GHz to 66% at 5.18 GHz. As a last step, a finite array of 5×4 was simulated; the capturing efficiency of the central rows is 74% at 2.5 GHz and 30% at 5.09 GHz at the optimum resistive load value. Similar to the proposed single-band metasurface RF harvester, the modifications were introduced to enable us to measure the output power of the dual-band design. The measured capturing efficiency of the middle row achieved 25% at 2.47GHz, and 38.5% at 5.05 GHz, whereas the simulated average row shows the capturing efficiency of 49.8% at 2.5 GHz and 40% at 5.1 GHz.

Both proposed single-band and dual-band metasurface RF harvesters are compact, and the fewest number of lumped elements as possible are employed within each design. By individually analyzing and optimizing each metasurface harvester, we were able to evaluate their standalone performance. Using our proposed methodology, we further enhanced their capturing efficiency. The dual-band design was developed with the objective of extending our single-band design into a multi-band harvester. The accomplishments presented in this manuscript provide a foundation that can be followed and expanded upon in future work.

Future Research Directions

For the single-band RF metasurface harvester, future work includes integrating it with the proposed single-band rectifier on the same layer. This approach eliminates the need for extension lines, enhancing both capturing and rectification efficiency and thereby improving the total RF to DC efficiency.

Regarding the dual-band metasurface RF harvester, while its capturing efficiency was enhanced through our proposed additional design step, the performance at the low frequency can be further improved. As future work, we propose readjusting the outer ring in the dual-band design to have a wider bandwidth performance. To achieve this, we suggest increasing the width of the microstrip lines of the outer ring, thereby accepting a larger cell size, to wider

the bandwidth at the low frequency, which will in turn increase the resilience to dimensioning and manufacturing errors. Furthermore, an additional resonator ring will be incorporated into the current dual-band design and optimized to form a multiband metasurface RF harvester. Additionally, a bigger size of finite array can be designed, as a larger array (with more rows) better resembles the periodic boundary conditions of the supercell that it is optimized for.

As we experienced some difficulties in performing the measurement via typical RF instruments, including accommodating a 50 Ω SMA connector, we propose to improve the methods for measuring the capturing efficiency as a function of the size of the structure.

A compatible dual-band rectifier can be designed to be integrated into the proposed dual-band metasurface harvester on the same layer to convert the collected RF power to DC. We suggest a design of a rectifier circuit based on a voltage doubler configuration in a differential topology operating at both 2.45 GHz and 5.2 GHz. For the diode selection, the Schottky diode SMS7630 remains a good choice.

List of Publications:

1- Based on Chapter II, the following contribution has been made [105]:

R. Sharifi, A. C. Lepage, K. Niotaki, and X. Begaud, “A single-layer efficient metasurface absorber for RF energy harvesting applications,” 2025 IEEE Int. Workshop Antenna Technol. (iWAT), pp. 1–4, 2025.

2- Based on Chapter IV, the following contribution has been made [136]:

R. Sharifi, A. C. Lepage, K. Niotaki, and X. Begaud, “An efficient compact dual-band metasurface RF energy harvester,” 2025 IEEE 19th Eur. Conf. Antennas Propag. (EuCAP), 2025.

- This work has been **selected** and **invited** for submission as an extended version to the **Special Issue of Reviews of Electromagnetics (RoE)**.

3- Based on Chapter IV, the following publication is currently under preparation for the special issue of RoE:

R. Sharifi, A. C. Lepage, K. Niotaki, and X. Begaud, “An Efficient Compact Single-Layer Dual-Band Metasurface RF Energy Harvester for IoT Applications,” under preparation for submission to the Special Issue of Reviews of Electromagnetics (RoE), 2025.

References

1. D.-J. Deng et al., “On quality-of-service provisioning in IEEE 802.11 ax WLANs,” IEEE Access, vol. 4, pp. 6086–6104, 2016.
2. D. Lopez-Perez et al., “IEEE 802.11 be extremely high throughput: The next generation of Wi-Fi technology beyond 802.11 ax,” IEEE Commun. Mag., vol. 57, no. 9, pp. 113–119, Sep. 2019.
3. V. V. Ratnam *et al*., “WiDRa—Enabling millimeter-level differential ranging accuracy in Wi-Fi using carrier phase,” IEEE J. Sel. Areas Commun., 2024.
4. Á. López-Raventós and B. Bellalta, “Concurrent decentralized channel allocation and access point selection using multi-armed bandits in multi BSS WLANs,” Comput. Netw., vol. 180, Art. no. 107381, 2020.
5. F. Soares and E. T. Rahardjo, “Development of a wearable wide band antenna in the frequency range of 2.4 GHz and 5.2 GHz,” Int. J. Electr. Comput. Biomed. Eng., vol. 2, no. 3, pp. 272–283, 2024.
6. H. H. R. Sherazi, D. Zorbas, and B. O’Flynn, “A comprehensive survey on RF energy harvesting: Applications and performance determinants,” Sensors, vol. 22, no. 8, Art. no. 2990, 2022.
7. M. Koohestani and A. Ghaneizadeh, “An ultra-thin double-functional metasurface patch antenna for UHF RFID applications,” Sci. Rep., vol. 11, no. 1, Art. no. 857, 2021.
8. S. Abdullah, G. Xiao, and R. E. Amaya, “A review on the history and current literature of metamaterials and its applications to antennas & radio frequency identification (RFID) devices,” IEEE J. Radio Freq. Identif., vol. 5, no. 4, pp. 427–445, 2021.
9. S. Priya and D. J. Inman, Eds., Energy Harvesting Technologies, vol. 21. New York, NY, USA: Springer, 2009.
10. T. J. Kazmierski and S. Beeby, Energy Harvesting Systems. Principles, Modeling and Applications. New York, NY, USA: Springer, 2011.
11. A. J. Williams, M. F. Torquato, I. M. Cameron, A. A. Fahmy, and J. Sienz, “Survey of energy harvesting technologies for wireless sensor networks,” IEEE Access, vol. 9, pp. 77493–77510, 2021.
12. M.-L. Ku, W. Li, Y. Chen, and K. R. Liu, “Advances in energy harvesting communications: Past, present, and future challenges,” IEEE Commun. Surveys Tuts., vol. 18, no. 2, pp. 1384–1412, 2nd Quart., 2016.
13. F. K. Shaikh and S. Zeadally, “Energy harvesting in wireless sensor networks: A comprehensive review,” Renew. Sustain. Energy Rev., vol. 55, pp. 1041–1054, Mar. 2016.
14. P. Sharma and A. K. Singh, “A survey on RF energy harvesting techniques for lifetime enhancement of wireless sensor networks,” Sustain. Comput. Informatics Syst., vol. 37, p. 100836, 2023.

15. T. Sanislav, G. D. Mois, S. Zeadally, and S. C. Folea, “Energy harvesting techniques for Internet of Things (IoT),” IEEE Access, vol. 9, pp. 39530–39549, 2021.

16. H. N. S. Aldin, M. R. Ghods, F. Nayebipour, and M. N. Torshiz, ‘‘A comprehensive review of energy harvesting and routing strategies for IoT sensors sustainability and communication technology,’’ Sensors Int., vol. 5, Jan. 2024.

17. N. Garg and R. Garg, “Energy harvesting in IoT devices: A survey,” in Proc. Int. Conf. Intell. Sustain. Syst. (ICISS), pp. 127–131, Dec. 2017.

18. H. Elahi, K. Munir, M. Eugeni, S. Atek, and P. Gaudenzi, ‘‘Energy harvesting towards self-powered IoT devices,’’ Energies, vol. 13, no. 21, p. 5528, Oct. 2020.

19. H. J. Visser and R. J. M. Vullers, “RF energy harvesting and transport for wireless sensor network applications: Principles and requirements,” Proc. IEEE, vol. 101, no. 6, pp. 1410–1423, Jun. 2013.

20. D. Bouchouicha, F. Dupont, M. Latrach, and L. Ventura, “Ambient RF energy harvesting,” in IEEE Int. Conf. Renewable Energies Power Quality (ICREPQ’10), pp. 486–495, Mar. 2010.

21. D. Mishra et al., “Smart RF energy harvesting communications: Challenges and opportunities,” IEEE Commun. Mag., vol. 53, no. 4, pp. 70–78, Apr. 2015.

22. M. Cansiz, D. Altinel, and G. K. Kurt, ‘‘Efficiency in RF energy harvesting systems: A comprehensive review,’’ Energy, vol. 174, pp. 292–309, May 2019.

23. H. Nishimoto, Y. Kawahara, and T. Asami, “Prototype implementation of ambient RF energy harvesting wireless sensor networks,” in Proc. IEEE Sens., Kona, HI, USA, Nov. 2010.

24. G. Chong, H. Ramiah, J. Yin, J. Rajendran, W. R. Wong, P.-I. Mak, and R. P. Martins, ‘‘Ambient RF energy harvesting system: A review on integrated circuit design,’’ Anal. Integr. Circuits Signal Process., vol. 97, no. 3, pp. 515–531, Dec. 2018.

25. S. Kitazawa, H. Ban, and K. Kobayashi, “Energy harvesting from ambient RF sources,” in Proc. IEEE MTT-S Int. Microw. Workshop Series Innovative Wireless Power Transm. Technol. Syst. Appl., Kyoto, Japan, pp. 39–42, May 2012.

26. W. C. Brown, “The history of power transmission by radio waves,” IEEE Trans. Microw. Theory Techn., vol. MTT-32, no. 9, pp. 1230–1242, Sep. 1984.

27. U. Muncuk, K. Alemdar, J. D. Sarode, and K. R. Chowdhury, “Multiband ambient RF energy harvesting circuit design for enabling batteryless sensors and IoT,” IEEE Internet Things J., vol. 5, no. 4, pp. 2700–2714, Aug. 2018.

28. H. Zeb, M. Gohar, M. Ali, A. U. Rahman, W. Ahmad, A. Ghani, J.-G. Choi, and S.-J. Koh, ‘‘Zero energy IoT devices in smart cities using RF energy harvesting,’’ Electronics, vol. 12, no. 1, p. 148, Dec. 2022.

29. N. A. Eltresy, O. M. Dardeer, A. Al-Habal, and E. Elhariri, ‘‘Smart home IoT system by using RF energy harvesting,’’ J. Sensors, vol. 2020, Dec. 2020.

30. S. Costanzo and F. Venneri, ‘‘Polarization-insensitive fractal metamaterial surface for energy harvesting in IoT applications,’’ Electronics, vol. 9, no. 6, p. 959, Jun. 2020.

31. S. Kim, R. Vyas, J. Bito, K. Niotaki, A. Collado, A. Georgiadis, and M. M. Tentzeris, ‘‘Ambient RF energy-harvesting technologies for selfsustainable standalone wireless sensor platforms,’’ Proc. IEEE, vol. 102, no. 11, pp. 1649–1666, Nov. 2014.

32. J. Zhou, P. Zhang, J. Han, L. Li, and Y. Huang, “Metamaterials and metasurfaces for wireless power transfer and energy harvesting,” Proc. IEEE Inst. Electr. Electron. Eng., vol. 110, no. 1, pp. 31–55, 2021.

33. O. M. Ramahi, T. S. Almoneef, M. Alshareef, and M. S. Boybay, “Metamaterial particles for electromagnetic energy harvesting,” Appl. Phys. Lett., vol. 101, no. 17, Oct. 2012.

34. L. Li, X. Zhang, C. Song, and Y. Huang, “Progress, challenges, and perspective on metasurfaces for ambient radio frequency energy harvesting,” Appl. Phys. Lett., vol. 116, no. 6, Feb. 2020.

35. H.-T. Zhong, X.-X. Yang, X.-T. Song, Z.-Y. Guo, and F. Yu, “Wideband metamaterial array with polarization-independent and wide incident angle for harvesting ambient electromagnetic energy and wireless power transfer,” Appl. Phys. Lett., vol. 111, no. 21, Nov. 2017.

36. X. Zhang, H. Liu, and L. Li, “Tri-band miniaturized wide-angle and polarization-insensitive metasurface for ambient energy harvesting,” Appl. Phys. Lett., vol. 111, no. 7, Aug. 2017.

37. H.-T. Zhong, X.-X. Yang, C. Tan, and K. Yu, “Triple-band polarization-insensitive and wide-angle metamaterial array for electromagnetic energy harvesting,” Appl. Phys. Lett., vol. 109, no. 25, Dec. 2016.

38. B. Alavikia, T. S. Almoneef, and O. M. Ramahi, “Wideband resonator arrays for electromagnetic energy harvesting and wireless power transfer,” Appl. Phys. Lett., vol. 107, no. 24, Dec. 2015.

39. S. D. Assimonis, T. Kollatou, D. Tsiamitros, D. Stimoniaris, T. Samaras, and J. N. Sahalos, ‘‘High efficiency and triple-band metamaterial electromagnetic energy hervester,’’ in Proc. 9th Int. Conf. Electr. Electron. Eng. (ELECO), pp. 320–323, Nov. 2015.

40. A. A. G. Amer, N. Othman, S. Z. Sapuan, A. Alphones, and A. A. Salem, ‘‘High-efficiency electromagnetic energy harvesting using double-elliptical metasurface resonators,’’ PLOS ONE, vol. 18, no. 12, p. e0291354, Dec. 2023.

41. X. Zhang, H. Liu, and L. Li, “Electromagnetic power harvester using wide-angle and polarization-insensitive metasurfaces,” Appl. Sci., vol. 8, no. 4, Mar. 2018.

42. F. Yu, X. Yang, H. Zhong, C. Chu, and S. Gao, ‘‘Polarization-insensitive wide-angle-reception metasurface with simplified structure for harvesting electromagnetic energy,’’ Appl. Phys. Lett., vol. 113, no. 12, Sep. 2018.

43. M. Dinh, N. Ha-Van, N. T. Tung, and M. Thuy Le, ‘‘Dual-polarized wideangle energy harvester for self-powered IoT devices,’’ IEEE Access, vol. 9, pp. 103376–103384, 2021.

44. B. Ghaderi, V. Nayyeri, M. Soleimani, and O. M. Ramahi, “Pixelated metasurface for dual-band and multi-polarization electromagnetic energy harvesting,” Sci. Rep., vol. 8, no. 1, 2018.

45. X. Duan, X. Chen, Y. Zhou, L. Zhou, and S. Hao, “Wideband metamaterial electromagnetic energy harvester with high capture efficiency and wide incident angle,” IEEE Antennas Wireless Propag. Lett., vol. 17, no. 9, pp. 1617–1621, Sep. 2018.

46. P. Gupta, S. Tripathi, S. Singh, and V. S. Gupta, “MPPT-EPO optimized solar energy harvesting for maximizing the WSN lifetime,” Peer-to-Peer Networking and Applications, vol. 16, no. 1, pp. 347–357, 2023.

47. A. Katepalli, Y. Wang, and D. Shi, “Solar harvesting through multiple semi-transparent cadmium telluride solar panels for collective energy generation,” Solar Energy, vol. 264, p. 112047, Nov. 2023.

48. D. Enescu, ‘‘Thermoelectric energy harvesting: Basic principles and applications,’’ Green Energy Advances, vol. 1, p. 38, Jan. 2019.

49. J. Davidson and C. Mo, “Recent advances in energy harvesting technologies for structural health monitoring applications,” Smart Materials Research, vol. 2014, no. 1, p. 410316, Apr. 2014.

50. S. Cao and J. Li, ‘‘A survey on ambient energy sources and harvesting methods for structural health monitoring applications,’’ Adv. Mech. Eng., vol. 9, no. 4, Apr. 2017.

51. J. A. Paradiso and T. Starner, “Energy scavenging for mobile and wireless electronics,” IEEE Trans. Pervasive Comput., vol. 4, no. 1, p. 1827, Jan. 2005.

52. Y.-H. Zhang, A. Lee, and C.-H. Lee, “Design and application of piezoelectric and electromagnetic energy harvesters for mechanical energy harvesting in the human body: A review,” Sensors and Actuators A: Physical, vol. 370, p. 115207, 2024.

53. F. Fatima, M. J. Akhtar, and O. M. Ramahi, “Frequency selective surface structures-based RF energy harvesting systems and applications: FSS-based RF energy harvesting systems,’’ IEEE Microwave Magazine, vol. 25, no. 3, pp. 47–69, Mar. 2024.

54. A. Ghaneizadeh, P. Gavriilidis, M. Joodaki, and G. C. Alexandropoulos, “Metasurface energy harvesters: State-of-the-art designs and their potential for energy sustainable reconfigurable intelligent surfaces,” IEEE Access, vol. 12, pp. 160464–160494, 2024.

55. A. Nayok, G. Prakash, and A. Rao, “Harnessing wind energy to power sensor networks for agriculture,” in Proc. IEEE Int. Conf. Adv. Energy Conservation Technol. (ICAECT), pp. 221–226, Jan. 2014.

56. F. Akhtar and M. H. Rehmani, “Energy harvesting for self-sustainable wireless body area networks,” IT Prof., vol. 19, no. 2, pp. 32–40, 2017.

57. S. Cao and J. Li, ‘‘A survey on ambient energy sources and harvesting methods for structural health monitoring applications,’’ Adv. Mech. Eng., vol. 9, no. 4, Apr. 2017.

58. F. Akhtar and M. H. Rehmani, “Energy replenishment using renewable and traditional energy resources for sustainable wireless sensor networks: A review,” Renew. Sustain. Energy Rev., vol. 45, pp. 769–784, May 2015.

59. M. A. Ullah, R. Keshavarz, M. Abolhasan, J. Lipman, K. P. Esselle, and N. Shariati, “A review on antenna technologies for ambient RF energy harvesting and wireless power transfer: Designs, challenges and applications,” IEEE Access, vol. 10, pp. 17231–17267, 2022.

60. A. Okba, A. Takacs, and H. Aubert, ‘‘Compact rectennas for ultra-lowpower wireless transmission applications,’’ IEEE Trans. Microw. Theory Techn., vol. 67, no. 5, pp. 1697–1707, May 2019.

61. F. Zhang, X. Liu, F.-Y. Meng, Q. Wu, J.-C. Lee, J.-F. Xu, C. Wang, and N.-Y. Kim, ‘‘Design of a compact planar rectenna for wireless power transfer in the ISM band,’’ Int. J. Antennas Propag., vol. 2014, pp. 1–9, Feb. 2014.

62. V. G. Veselago, “The electrodynamics of substances with simultaneously negative values of ε and μ,” Sov. Phys.—Usp., vol. 10, pp. 509–514, 1968.

63. A. Boardman, “Pioneers in metamaterials: John Pendry and Victor Veselago,” J. Opt., vol. 13, no. 2, pp. 1–6, 2011.

64. J. B. Pendry, A. J. Holden, D. J. Robbins, and W. J. Stewart, “Magnetism from conductors and enhanced nonlinear phenomena,” IEEE Trans. Microw. Theory Tech., vol. 47, no. 11, pp. 2075–2084, Nov. 1999.

65. C. M. Watts, X. Liu, and W. J. Padilla, “Metamaterial electromagnetic wave absorbers,” Adv. Mater., vol. 24, no. 23, pp. OP98–OP120, Jun. 2012.

66. H. Mosallaei and K. Sarabandi, “A one-layer ultra-thin meta-surface absorber,” in Proc. IEEE Antennas Propag. Society Int. Symp., vol. 1, pp. 615–618, 2005.

67. C. L. Holloway, A. Dienstfrey, E. F. Kuester, J. F. O’Hara, A. K. Azad, and A. J. Taylor, “A discussion on the interpretation and characterization of metafilms/metasurfaces: The two-dimensional equivalent of metamaterials,” Metamaterials, vol. 3, no. 2, pp. 100–112, Oct. 2009.

68. N. Engheta, ‘‘Thin absorbing screens using metamaterial surfaces,’’ in Proc. IEEE Antennas Propag. Soc. Int. Symp., vol. 2, pp. 392–395, Jun. 2002.

69. M. Park, J. Choi, and S. Kim, “Wide bandwidth pyramidal absorbers of granular ferrite and carbonyl iron powders,” IEEE Trans. Magn., vol. 36, no. 5, pp. 3272–3274, Sep. 2000.

70. H. Kwon, M. Jang, J. Yun, Y. Park, C. Shin, J. Yang, C. Kim, “Design and verification of simultaneously self-sensing and microwave-absorbing composite structures based on embedded SiC fiber network,” Composite Struct., vol. 261, p. 113286, 2021.

71. K. Li, X. Zhang, X. Hou, and P. Zhang, “Analysis and design of multilayer Jaumann absorbers,” in Proc. IEEE Int. Conf. Microw. Technol. Comput. Electromagn., pp. 81–84, May 2011.

72. N. I. Landy, S. Sajuyigbe, J. J. Mock, D. R. Smith, and W. J. Padilla, ‘‘Perfect metamaterial absorber,’’ Phys. Rev. Lett., vol. 100, no. 20, May 2008.

73. W. W. Salisbury, “Absorbent Body for Electromagnetic Waves,” U.S. patent 2599944, Jun. 1952.

74. A. Ghaneizadeh, K. Mafinezhad, and M. Joodaki, “A new compact dual-band perfect absorption ultrathin planar metasurface energy harvester in X-and V-bands with a wide incident angle,” AIP Adv., vol. 10, no. 8, Aug. 2020.

75. P. Shah and G. Shrikanth Reddy, “A dual-band, wide-angle, polarization insensitive metasurface-based RF energy harvester,” 2024 IEEE Int. Symp. Antennas Propag. INC/USNC-URSI Radio Sci. Meeting (AP-S/INC-USNC-URSI), pp. 1791–1792, 2024.

76. A. Ghaneizadeh, K. Mafinezhad, and M. Joodaki, “Design and fabrication of a 2D-isotropic flexible ultra-thin metasurface for ambient electromagnetic energy harvesting,” AIP Adv., vol. 9, no. 2, Feb. 2019.

77. H. Ojukwu, B. Seet, and S. U. Rehman, ‘‘Wideband and load-insensitive metasurface absorber for radio frequency energy harvesting,’’ in Proc. IEEE 33rd Annu. Int. Symp. Pers., Indoor Mobile Radio Commun. (PIMRC), pp. 963–967, Sep. 2022.

78. Y. Zhang, R. Huang, G. Wang, Z. H. Jiang, and W. Hong, ‘‘A lowcost polarization detection approach enabled by energy harvesting metasurface: Concept, design, and experiment,’’ IEEE Trans. Microw. Theory Techn., vol. 72, no. 10, pp. 6174–6186, Oct. 2024.

79. X. Duan, X. Chen, and L. Zhou, “A metamaterial electromagnetic energy rectifying surface with high harvesting efficiency,” AIP Adv., vol. 6, no. 12, Dec. 2016.

80. A. M. Hawkes, A. R. Katko, and S. A. Cummer, “A microwave metamaterial with integrated power harvesting functionality,” Appl. Phys. Lett., vol. 103, no. 16, Sep. 2013.

81. C. Song, Y. Wei, J. Kang, H. Jing, J. Wang, Z. Qu, B. Zhang, and J. Duan, “A dual-band, wide-angle absorbing metasurface for EM energy harvesting and wireless power transfer,” Opt. Commun., vol. 549, p. 129799, Dec. 2023.

82. L. KangHyeok and S. K. Hong, ‘‘Rectifying metasurface with high efficiency at low power for 2.45 GHz band,’’ IEEE Antennas Wireless Propag. Lett., vol. 19, no. 12, pp. 2216–2220, Dec. 2020.

83. M. El Badawe, T. S. Almoneef, and O. M. Ramahi, “A metasurface for conversion of electromagnetic radiation to DC,” AIP Adv., vol. 7, no. 3, Mar. 2017.

84. C. Song, Y. Wei, J. Wang, B. Zhang, Y. Qin, and J. Duan, ‘‘A wide-angle incidence, broadband rectified metasurface for radar frequency band EM energy harvesting and wireless power transfer,’’ Opt. Laser Technol., vol. 174, Jul. 2024.

85. H. Zhang, Y. Li, W. Hu, Q. Lu, B. Zhang, and L. Y. Yang, “Polarization-insensitive electromagnetic metamaterial design for multi-band energy harvesting,” IEEE Access, vol. 11, pp. 143956–143963, Dec. 2023.

86. P. Xu, S.-Y. Wang, and W. Geyi, “Design of an effective energy receiving adapter for microwave wireless power transmission application,” AIP Adv., vol. 6, no. 10, Oct. 2016.

87. T. S. Almoneef, F. Erkmen, and O. M. Ramahi, “Harvesting the energy of multi-polarized electromagnetic waves,” Sci. Rep., vol. 7, no. 1, p. 14, Nov. 2017.

88. C. Fowler, S. Silva, G. Thapa, and J. Zhou, “High efficiency ambient RF energy harvesting by a metamaterial perfect absorber,” Opt. Mater. Exp., vol. 12, no. 3, pp. 1242–1250, Mar. 2022.

89. L. Li, X. Zhang, C. Song, W. Zhang, T. Jia, and Y. Huang, “Compact dual-band, wide-angle, polarization-angle-independent rectifying metasurface for ambient energy harvesting and wireless power transfer,” IEEE Trans. Microw. Theory Techn., vol. 69, no. 3, pp. 1518–1528, Mar. 2021.

90. A. Z. Ashoor and O. M. Ramahi, “Polarization-independent cross-dipole energy harvesting surface,” IEEE Trans. Microw. Theory Techn., vol. 67, no. 3, pp. 1130–1137, Mar. 2019.

91. F. Erkmen, T. S. Almoneef, and O. M. Ramahi, “Scalable electromagnetic energy harvesting using frequency-selective surfaces,” IEEE Trans. Microw. Theory Techn., vol. 66, no. 5, pp. 2433–2441, May 2018.

92. A. Mouapi, “Radiofrequency energy harvesting systems for internet of things applications: A comprehensive overview of design issues,” Sensors, vol. 22, no. 21, p. 8088, 2022. 8088.

93. W. Li, T. Shen, B. Zhang, and Y. Wei, “A scalable, wide-angle metasurface array for electromagnetic energy harvesting,” Micromachines, vol. 15, no. 7, p. 904, 2024.

94. Y. Wei, J. Duan, H. Jing, H. Yang, H. Deng, C. Song, J. Wang, Z. Qu, and B. Zhang, ‘‘Scalable, dual-band metasurface array for electromagnetic energy harvesting and wireless power transfer,’’ Micromachines, vol. 13, no. 10, p. 1712, Oct. 2022.

95. Y. Wei et al., “A dual-band, polarization-insensitive, wide-angle metasurface array for electromagnetic energy harvesting and wireless power transfer,” Results Phys., vol. 46, Mar. 2023.

96. F. Erkmen and O. M. Ramahi, “A scalable, dual-band absorber surface for electromagnetic energy harvesting and wireless power transfer,” IEEE Trans. Antennas Propag., early access, May 27, 2021.

97. M. Amiri, M. Abolhasan, N. Shariati, and J. Lipman, ‘‘Highly efficient polarization-insensitive EM energy harvester,’’ in Proc. 18th Eur. Conf. Antennas Propag. (EuCAP), pp. 1–5, Mar. 2024.

98. Y. Wei et al., “A multiband, polarization-controlled metasurface absorber for electromagnetic energy harvesting and wireless power transfer,” IEEE Trans. Microw. Theory Techn., vol. 70, no. 5, pp. 2861–2871, May 2022.

99. N. Fernez et al., “Radiative quality factor in thin resonant metamaterial absorbers,” IEEE Trans. Microw. Theory Techn., vol. 66, no. 4, pp. 1764–1772, Apr. 2018.

100. Z. Geng, W. Su, X. Wang, Y. Jiang, and Y. Liu, ‘‘Numerical design of a metasurface-based ultra-narrow band terahertz perfect absorber with high Q-factors,’’ Optik, vol. 194, Oct. 2019.

101. D. B. Stojanovi´c, G. Gligori´c, P. P. Beli˘cev, M. R. Beli´c, and L. Hadžievski, “Circular polarization selective metamaterial absorber in terahertz frequency range,” IEEE J. Sel. Topics Quantum Electron., vol. 27, no. 1, Jan./Feb. 2021.

102. K. Chang and L.-H. Hsieh, Microwave Ring Circuits and Related Structures, 2nd ed. New York, NY, USA: Wiley, 2004.

103. M. El Badawe and O. M. Ramahi, ‘‘Efficient metasurface rectenna for electromagnetic wireless power transfer and energy harvesting,’’ Prog. Electromagn. Res., vol. 161, pp. 35–40, 2018.

104. A. A. G. Amer, N. Othman, M. M. Bait-Suwailamn, S. Z. Sapuan, A. A. A. Salem, and A. Salh, "Polarization-Insensitive, High-Efficiency Metasurface with Wide Reception Angle for Energy Harvesting Applications," Sensors, vol. 25, no. 2, p. 429, 2025.

105. R. Sharifi, A. C. Lepage, K. Niotaki, and X. Begaud, “A single-layer efficient metasurface absorber for RF energy harvesting applications,” 2025 IEEE Int. Workshop Antenna Technol. (iWAT), pp. 1–4, 2025.

106. C. R. Valenta and G. D. Durgin, ‘‘Harvesting wireless power: Survey of energy-harvester conversion efficiency in far-field, wireless power transfer systems,’’ IEEE Microw. Mag., vol. 15, no. 4, pp. 108–120, Jun. 2014.

107. L.-G. Tran, H.-K. Cha, and W.-T. Park, ‘‘RF power harvesting: A review on designing methodologies and applications,’’ Micro Nano Syst. Lett., vol. 5, no. 1, pp. 1–16, Dec. 2017.

108. A. Fereshtian, J. Berenguer, and M. Gasulla, "RF energy harvesting for IoT sensors: Effects of inductor quality factor on efficiency," IEEE International Instrumentation and Measurement Technology Conference (I2MTC), pp. 1-5, 2024.

109. H. Jabbar, Y. S. Song, and T. T. Jeong, “RF energy harvesting system and circuits for charging of mobile devices,” IEEE Trans. Consum. Electron., vol. 56, no. 1, pp. 247–253, 2010.

110. C. Zheng, B. Chen, L. Zhang, R. Chen, and J. S. Lai, “Design considerations of LLC resonant converter for contactless laptop charger,” in Proc. IEEE Appl. Power Electron. Conf. Expo., pp. 3341–3347, Mar. 2015.

111. L. Sa’adu, Y. Yusuf, and A. B. Isah, " Design and Implementation of a Backup Laptop Power Bank," BIMA Journal of Science and Technology, vol. 8, no. 4B, pp. 248-259, 2025.

112. V. Prabhakaran and S. Pavithra, "An eminent design for wireless power transfer using rectenna module using interleaved boost converter to increase the power efficacy delivered to the biomedical device," IOP Conference Series: Materials Science and Engineering. Vol. 993. No. 1. IOP Publishing, 2020.

113. R. Visintini, "Rectifiers," CAS - CERN Accelerator School: Specialised CAS Course on Power Converters, vol. 10, no. 133, pp. 133-184, 2006.

114. M. A. Halimi, T. Khan, Nasimuddin, A. A. Kishk, and Y. M. M. Antar, “Rectifier circuits for RF energy harvesting and wireless power transfer applications: A comprehensive review based on operating conditions,” IEEE Microw. Mag., vol. 24, no. 1, pp. 46–61, 2022.

115. D. Surender, M. A. Halimi, T. Khan, F. A. Talukdar, Nasimuddin, and S. R. Rengarajan, “5G/Millimeter-wave rectenna systems for radio-frequency energy harvesting/wireless power transmission applications: An overview,” IEEE Antennas Propag. Mag., vol. 65, no. 3, pp. 57–76, 2022.

116. N. U. Khan, F. U. Khan, M. Farina, and A. Merla, “RF energy harvesters for wireless sensors, state of the art, future prospects and challenges: A review,” Physical and Engineering Sciences in Medicine, pp. 1–17, Jun. 2024.

117. A. Boaventura, A. Collado, N. B. Carvalho, and A. Georgiadis, “Optimum behavior: Wireless power transmission system design through behavioral models and efficient synthesis techniques,” IEEE Microw. Mag., vol. 14, no. 2, pp. 26–35, Mar. 2013.

118. O. Assogba, A. K. Mbodji, and A. K. Diallo, ‘‘Efficiency in RF energy harvesting systems: A comprehensive review,’’ in Proc. IEEE Int. Conf Natural Eng. Sci. Sahel’s Sustain. Develop. Impact Big Data Appl. Soc. Environ. (IBASE-BF), pp. 1–10, Feb. 2020.

119. A. Reddaf, M. Boudjerda, I. Bouchachi, B. Babes, A. Elrashidi, K. M. AboRas, E. Ali, S. S. M. Ghoneim, and M. Elsisi, ‘‘Modeling of Schottky diode and optimal matching circuit design for low power RF energy harvesting,’’ Heliyon, vol. 10, no. 6, Mar. 2024.

120. H. P. da Paz, V. S. da Silva, E. V. Cambero, H. X. de Araújo, I. R. Casella, and C. E. Capovilla, "Analysis of rectifiers for RF energy harvesting aiming low power sensing applications," in 2019

IEEE 15th Brazilian Power Electronics Conference and 5th IEEE Southern Power Electronics Conference (COBEP/SPEC), pp. 1-5, Dec. 2019.

121. K. W. Lui, A. Vilches, and C. Toumazou, “Ultra-efficient microwave harvesting system for battery-less micropower microcontroller platform,” IET Microw. Antennas Propag., vol. 5, no. 7, pp. 811–817, 2011.

122. R. Agieb, A. Amer, I. Mansour, A. Solyman, K. Yahya, and A. Samir, “Improving energy harvesting system from ambient RF sources in social systems with overcrowding,” International Journal of Crowd Science, vol. 9, no. 1, pp. 13–28, 2025.

123. T. Hirakawa and N. Shinohara, “Theoretical analysis and novel simulation for single shunt rectifiers,” IEEE Access, vol. 9, pp. 16615–16622, 2021.

124. M. Zeng, A. S. Andrenko, X. Liu, B. Zhu, Z. Li, and H.-Z. Tan, “Differential topology rectifier design for ambient wireless energy harvesting,” in 2021 IEEE International Conference on Electronics, Computing and Communication Technologies (CONECCT), pp. 1-5, Jul. 2021.

125. G. Polaiah, K. Kandasamy, and M. Kulkarni, "Differential Frequency-Reconfigurable Rectifier for Efficient Microwave Energy Harvesting Applications," in 2021 IEEE International Conference on Electronics, Computing and Communication Technologies (CONECCT), pp. 1-5, 2021.

126. S. S. Sarma, S. Chandravanshi, and M. J. Akhtar, ‘‘Triple band differential rectifier for RF energy harvesting applications,’’ in Proc. IEEE Asia– Pacific Microw. Conf. (APMC), pp. 1–4, Dec. 2016.

127. Q. W. Lin and Y. Z. Xiu, “Differential rectifier using resistance compression network for improving efficiency over extended input power range,” IEEE Trans. Microw. Theory Tech., vol. 64, no. 9, pp. 2943–2954, 2016.

128. El Mattar, Sara, Abdennaceur Baghdad, and Abdelhakim Ballouk. "A 2.45/5.8 GHz high-efficiency dual-band rectifier for low radio frequency input power." International Journal of Electrical and Computer Engineering 12.3 (2022): 2169.

129. S. Chandravanshi, S. Sen Sarma, and M. J. Akhtar, “Design of triple band differential rectenna for RF energy harvesting,” IEEE Trans. Antenn. Propag., vol. 66, no. 6, pp. 2716–2726, 2018.

130. H. Sun, “An enhanced rectenna using differentially-fed rectifier for wireless power transmission,” IEEE Antennas Wireless Propag. Lett., vol. 15, pp. 32–35, Apr. 2016.

131. “BAL-0026 broadband isolation balun (300 KHz to 26.5 GHz),” Marki Microwave, Inc., Datasheet BAL-0026, Rev. E, 2020.

132. Y. Wei, J. Duan, H. Jing, Z. Lyu, J. Hao, Z. Qu, J. Wang, and B. Zhang, ‘‘A multiband, polarization-controlled metasurface absorber for electromagnetic energy harvesting and wireless power transfer,’’ IEEE Trans. Microw. Theory Techn., vol. 70, no. 5, pp. 2861–2871, May 2022.

133. A. A. G. Amer, N. Othman, S. Z. Sapuan, A. Alphones, M. F. Hassan, A. J. A. Al-Gburi, and Z. Zakaria, ‘‘Dual-band, wide-angle, and high-capture efficiency metasurface for electromagnetic energy harvesting,’’ Nanomaterials, vol. 13, no. 13, p. 2015, Jul. 2023.

134. W. Hu, Z. Yang, F. Zhao, G. Wen, J. Li, Y. Huang, D. Inserra, and Z. Chen, ‘‘Low-cost air gap metasurface structure for high absorption efficiency energy harvesting,’’ Int. J. Antennas Propag., vol. 2019, pp. 1–8, Sep. 2019.

135. M. El Badawe, A. Albishi, and O. M. Ramahi, "Polarization independent dual-band RF energy harvester," 12th Eur. Conf. Antennas Propag. (EuCAP), pp. 7–9, 2018.

136. R. Sharifi, A. C. Lepage, K. Niotaki, and X. Begaud, “An efficient compact dual-band metasurface RF energy harvester,” 2025 IEEE 19th Eur. Conf. Antennas Propag. (EuCAP), 2025.

Résumé Étendu

Les dispositifs IoT (Internet des objets) de faible puissance, tels que les capteurs de température, de lumière ou de mouvement, sont généralement déployés en grand nombre dans les environnements domestiques, industriels ou urbains. Leur alimentation reste un défi technique majeur, en particulier lorsque l'accès aux sources d'énergie traditionnelles (batterie, câble d'alimentation) est restreint ou indésirable pour des raisons de maintenance, de coût ou de compacité. Dans ce contexte, la récupération de l'énergie ambiante, et plus particulièrement l'exploitation des radiofréquences (RF) présentes dans l'environnement, constitue une solution prometteuse. Parmi les diverses sources d'énergie ambiante exploitables (thermique, solaire, vibratoire, …), les signaux radiofréquences (RF) représentent une source omniprésente et largement sous-exploitée, en particulier dans les environnements urbains ou domestiques riches en communications sans fil. Cependant, la densité de puissance RF disponible dans l'environnement est relativement faible.

Les bandes de fréquences utilisées par les technologies Wi-Fi (notamment 2,45 GHz et 5,2 GHz) sont particulièrement intéressantes pour cette application, en raison de leur déploiement à grande échelle et de leur densité de puissance relativement plus élevée dans les environnements intérieurs. Cependant, les niveaux d'énergie disponibles restent faibles, ce qui nécessite une conception fine et optimisée des systèmes de récupération d'énergie RF.

Cette thèse est consacrée à la conception, l'optimisation et la validation expérimentale de dispositifs compacts de récupération d'énergie RF ambiante basés sur des métasurfaces, spécifiquement adaptés aux bandes Wi-Fi, et intégrables dans des solutions IoT autonomes.

L'objectif principal est de concevoir, simuler, fabriquer et évaluer des métasurfaces RF capables de récupérer et de convertir efficacement l'énergie électromagnétique disponible dans ces bandes. Le travail a été structuré autour des objectifs suivants :

1. Concevoir une métasurface RF efficace opérant à 2,45 GHz, avec un minimum de composants discrets, maximisant l'efficacité de récupération tout en conservant une structure compacte et facile à fabriquer.

2. Optimiser cette métasurface pour améliorer son efficacité de récupération, en particulier par une étude détaillée des paramètres géométriques de la cellule unitaire et par une méthodologie nouvelle.

3. Développer un circuit de redressement différentiel, compatible avec la métasurface conçue, en minimisant également le nombre de composants et en maximisant l'efficacité du redressement, en utilisant des composants adaptés aux faibles niveaux de puissance, tels que les diodes Schottky.

4. Valider les performances de chaque sous-système indépendamment : la métasurface seule, le redresseur seul, puis le système entier, par des simulations électromagnétiques et des mesures expérimentales, dans des conditions réalistes.

5. Étendre la conception à une version bi-bande, capable de récupérer de l'énergie simultanément à 2,45 GHz et 5,2 GHz, tout en maintenant une faible complexité structurelle et un nombre réduit de composants.

1. Conception de la métasurface

L'architecture retenue repose sur des cellules interconnectées, une approche permettant de combiner la puissance récupérée par plusieurs cellules tout en maintenant une structure plane. Dans un premier temps, afin de faciliter l'optimisation de la métasurface, le circuit redresseur est remplacé par une résistance, qui modélise alors l'impédance d'entrée de ce dernier.

Étapes de conception :

- Cellule unitaire : une cellule compacte a été conçue pour résonner à 2,45 GHz sur un substrat Arlon Diclad 880. La valeur optimale de la résistance de charge a été déterminée à 700 Ω, ce qui permet une efficacité de récupération simulée de 94 %.

- Supercellule : quatre cellules interconnectées ont été simulées. Après ré-optimisation de la résistance de charge à 115 Ω, l'efficacité a augmenté de 62 % à 92 % à 2,49 GHz.

- Réseau fini 5×4 : l'efficacité a été évaluée en considérant uniquement les lignes centrales et en éliminant les lignes aux bords (concept de "lignes centrales moyennes"). Une efficacité de 90 % a été obtenue.

Simulations:

La cellule unitaire et la supercellule ont été simulées dans CST Studio Suite avec des conditions aux limites périodiques (Floquet), tandis que le réseau fini de 5×4 cellules a été modélisé à l'aide du solveur en domaine temporel.

Mesures:

Le réseau a été fabriqué avec des modifications pour la connectique RF. Ces modifications ont entraîné une légère dégradation des performances. L'efficacité mesurée sur la ligne centrale est de 61 % à 2,49 GHz, contre 73 % simulée à 2,54 GHz.

Version bi-bande :

Une seconde résonance a été introduite dans la cellule. La cellule bi-bande fonctionne simultanément à 2,45 GHz et 5,2 GHz. La charge optimale a été fixée à 300 Ω, permettant une efficacité simulée de 94 % à 2,45 GHz et 96 % à 5,2 GHz. Après l'optimisation de la supercellule, la simulation et la réalisation du réseau fini (5x4 cellules), les performances obtenues sont les suivantes :

- 25 % à 2,47 GHz et 38,5 % à 5,05 GHz en mesures,
- 49,8 % à 2,5 GHz et 40 % à 5,1 GHz en simulation.

2. Conception du circuit redresseur

Un redresseur différentiel a été conçu pour convertir l'énergie RF captée en tension continue. Le circuit est basé sur une diode Schottky SMS7630, choisie pour sa faible tension seuil, idéale pour les faibles niveaux d'entrée.

Simulation:

Le redresseur proposé a été simulé à l'aide du logiciel Advanced Design System (ADS), en combinant une co-simulation avec Momentum. Une efficacité de redressement de 58 % a été obtenue à −2,7 dBm à 2,49 GHz.

Dans un deuxième temps, certaines modifications ont été effectuées afin de permettre la mesure. Celles-ci ont entraîné une baisse de l'efficacité de 4.3%.

Mesure:

La mesure a montré une efficacité de redressement de 46,4 % à −2,7 dBm à 2,45 GHz, en bon accord avec les résultats de simulation.

3. Performances du dispositif récupérateur d'énergie

Une fois les sous-systèmes validés individuellement, le redresseur a ensuite été associé à la métasurface via deux câbles courts pour former un système complet, dont l'efficacité globale RF-DC a été évaluée.

La même antenne cornet que celle utilisée lors des mesures de la métasurface seule a été employée, combinée à un amplificateur.

Les mesures ont montré que l'efficacité totale atteint environ 20 % à 2,51 GHz. Ce résultat valide l'efficacité de la conception dans un contexte de récupération d'énergie ambiante à faible densité de puissance.

4. Conclusion

L'ensemble de ce travail apporte une contribution originale à la récupération de l'énergie RF ambiante, en combinant :

- Simplicité structurelle, grâce à des conceptions compactes et faciles à fabriquer ;

- Haute efficacité de récupération, grâce à des optimisations ciblées des géométries et des charges ;

- Extensibilité, avec une méthode généralisable aux conceptions multi-bandes.

Les résultats obtenus démontrent que des systèmes simples mais bien optimisés peuvent offrir des performances intéressantes dans un contexte d'énergie ambiante à faible densité. Ce travail peut servir de base à de futurs développements, notamment pour l'intégration directe avec des capteurs IoT, la miniaturisation avancée ou la récupération dans des environnements RF complexes.

ECOLE DOCTORALE

Titre : Récupération d'énergie efficace à Métasurface pour application IoT

Mots clés : Récupération d'énergie, Internet des objets, Métasurfaces, Radiofréquence, Transfert d'énergie sans fil

Résumé : Les communications sans fil et l'Internet des objets (IoT) deviennent des éléments incontournables de la vie moderne. En évitant l'utilisation de batteries et en réduisant ainsi les coûts, la taille et le poids des appareils, la récupération d'énergie ambiante représente une alternative prometteuse pour l'alimentation électrique. L'énergie ambiante peut être captée à partir de diverses sources telles que l'énergie solaire, éolienne ou les signaux radiofréquences (RF). Alors que les énergies solaire et éolienne offrent une densité de puissance élevée, elles ne sont pas toujours disponibles. À l'inverse, les signaux RF sont omniprésents, mais leur densité de puissance est relativement faible. Plusieurs solutions permettent de collecter l'énergie électromagnétique, notamment les rectennas et les métasurfaces pour la récupération d'énergie. Pour utiliser des absorbants dans les dispositifs de récupération d'énergie, le défi principal est de maximiser l'énergie collectée et ainsi de minimiser les pertes dans les diélectriques. À cet égard, les absorbants à base de métasurface, grâce à leur faible épaisseur et leurs caractéristiques d'absorption constituent des solutions prometteuses si on utilise un substrat à faibles pertes. En général, les dispositifs de récupération d'énergie basés sur des métasurfaces se présentent sous forme de structures multicouches ou planaires. L'inconvénient majeur des structures multicouches réside dans leur complexité de fabrication. Les conceptions planaires permettent de surmonter ce problème. De plus, étant donné que l'énergie RF ambiante est généralement faible, il est essentiel d'en capter un maximum en optimisant les performances du dispositif récupérateur d'énergie. Dans cette thèse, des récupérateurs d'énergie à base de métasurface compacts et efficaces sont proposés : une structure monobande fonctionnant à 2,45 GHz et une bi-bande fonctionnant à 2,45 GHz et 5,2 GHz. Dans un premier temps, les métasurfaces ont été conçues. Étant donné les faibles niveaux d'énergie RF ambiante, maximiser la puissance collectée est une priorité. Pour relever ce défi, une étape intermédiaire dans le processus de conception a été introduite afin d'améliorer l'efficacité de capture. Cette étape supplémentaire a été appliquée aux deux structures, monobande et bi-bande. Un réseau fini de 5×4 cellules est développé pour chaque structure. L'efficacité de capture des rangées centrales du réseau fini simulé atteint 90 % à 2,54 GHz pour la version monobande. Pour la conception bi-bande, l'efficacité de capture des rangées centrales est de 74 % à 2,5 GHz et de 30 % à 5,09 GHz en simulation. Dans un second temps, un circuit redresseur mono-bande à base de diodes Schottky est proposé pour être intégré à la métasurface mono-bande, afin de convertir l'énergie RF captée en courant continu. L'efficacité de redressement à 2,49 GHz pour une puissance d'entrée de -2,7 dBm atteint 58 %. Les métasurfaces mono-bande et bi-bande ainsi que le redresseur ont été analysés indépendamment. Ensuite, tous les dispositifs ont été fabriqués et mesurés afin de vérifier leurs performances.

Title : Efficient Metasurface Energy Harvesters for IoT Applications

Keywords : Energy harvesting, Internet of Things (IoT), Metasurfaces, Radio Frequency, Wireless power transfer

Abstract : Wireless communications and the Internet of Things are becoming integral parts of modern life. By avoiding the need for batteries—thereby reducing the cost as well as the size and weight of appliances—energy harvesting by collecting ambient energy represents a promising alternative power supply. Ambient energy in the environment can be captured from various sources like solar, wind, or radio frequency signals, etc. While solar and wind energy are characterized by a high power density, these sources are not always available. Radio frequency signals, on the other hand, have the advantage of being ubiquitously present but have a comparatively low power density. There are several solutions for collecting electromagnetic energy; two common solutions are rectenna and metasurface for energy harvesting. To use absorbers in energy harvesting devices, the challenge is to maximize the collected energy and thus to minimize losses which occur in dielectrics. To do so, metasurfaces, with their low profile and absorption characteristics can be good candidates using a low-loss substrate.
In general, in energy harvesting devices based on metasurface, either multi-layer or planar structures can be used. The main drawback of multi-layer structures is the complexity of fabrication. Planar designs help to overcome this problem. Moreover, as the ambient radio frequency energy is usually low, it is necessary to collect most of it by improving the performance of the metasurface. To do so, in this thesis, compact efficient metasurface harvesters are proposed: a single-band design operating at 2.45 GHz and a dual-band design operating at 2.45 GHz, and 5.2 GHz. Firstly, the metasurface structures have been designed. Given the low levels of ambient radio frequency energy, it is crucial to maximize the collected power. To address this challenge, an intermediate step in the design process is introduced to enhance the capturing efficiency of metasurface. This additional step is applied for both proposed single and dual-band designs. A finite array of 5×4 cells is presented for both designs. The simulated capturing efficiency of the central rows of the finite array for the single-band design is 90% at 2.54 GHz. The simulated capturing efficiency of the central rows of the finite array for the dual-band design is 74% at 2.5 GHz, and 30% at 5.09 GHz. Secondly, a single-band rectifier circuit based on Schottky diodes is proposed to be integrated with the single-band metasurface structure, in order to convert the collected radio frequency energy to DC. The rectification efficiency at 2.49 GHz at the differential input of the rectifier at -2.7 dBm, is 58%. Each proposed design of the metasurfaces and the rectifier has been analyzed independently. Then all have been fabricated and measured to verify their performance.

Institut Polytechnique de Paris
91120 Palaiseau, France